Title
Studies of Gamma-Ray Burst Prompt Emission with RHESSI and NCT

Author
Bellm, Eric Christopher

Publication Date
2011

Studies of Gamma-Ray Burst Prompt Emission with RHESSI and NCT

by

Eric Christopher Bellm

A dissertation submitted in partial satisfaction of the
requirements for the degree of
Doctor of Philosophy

in

Physics

in the

Graduate Division
of the
University of California, Berkeley

Committee in charge:
Professor Steven E. Boggs, Chair
Professor Robert P. Lin
Professor Joshua S. Bloom

Spring 2011

Studies of Gamma-Ray Burst Prompt Emission with RHESSI and NCT

Abstract

Studies of Gamma-Ray Burst Prompt Emission with RHESSI and NCT

by

Eric Christopher Bellm
Doctor of Philosophy in Physics

University of California, Berkeley

Professor Steven E. Boggs, Chair

Gamma-Ray Bursts (GRBs) are the most luminous objects in the universe. They herald a catastrophic energy release which manifests itself in tenths to hundreds of seconds of irregular gamma-ray emission. This initial "prompt" emission is followed by "afterglow" emission at other wavelengths that fades smoothly over hours to years.

GRB prompt emission has been observed with ever-increasing sophistication for more than four decades, but many details of its origin remain unknown. While GRBs are understood to result from relativistic jets produced by violent reconfigurations of compact objects, the composition of the outflow, the means of energy dissipation, and the radiative processes underlying the observed emission are all uncertain. I review the present understanding of all facets of GRB science in Chapter 1.

Gamma-ray spectroscopy and polarimetry provide two channels for testing models of GRB prompt emission with observed data. In Chapters 2–4, I employ the Reuven Ramaty High-Energy Solar Spectroscopic Imager (RHESSI) to conduct broad-band time-resolved spectroscopy of bright GRBs. RHESSI is a solar observatory that uses nine coaxial germanium detectors for imaging and spectroscopy of solar flares. Because the detectors are unshielded, RHESSI also records counts from off-axis sources like GRBs. In Chapter 2, I detail the methods I use for analyzing RHESSI GRB data.

In Chapter 3, I conduct joint spectral analysis of bursts co-observed by RHESSI and *Swift*-BAT, enabling spectral modeling over a wide 15 keV–17 MeV band. These results reveal the difficulty of predicting the peak spectral energy of a burst from BAT observations alone.

While GRB spectra commonly have been assumed to be non-thermal and have been fit by purely phenomenological models, some authors have proposed that thermal emission from the GRB photosphere may be the source of the GRB spectral peak. In Chapter 4, I perform time-resolved spectroscopy of bright GRBs observed by RHESSI and compare the fit results of several phenomenological and quasi-thermal models. The fit results for the quasi-thermal models are poorer than those reported for fits in more narrow energy bands, and the fit parameters show significant dependence on the fit band. More sophisticated models and additional data are needed to determine the relevance of the photospheric emission.

Polarimetric studies of GRBs are in their infancy, but they have the potential to distinguish GRB emission models and probe the structure of the relativistic jet. Observations to date have exploited the polarimetric signatures produced by Compton scattering in gamma-ray observatories. Since these instruments have poor spatial resolution and are not calibrated for polarimetric observations, only a few bright GRBs have been observed, each with significant systematic effects. In Chapters 5–8, I present development work for a balloon-borne Compton telescope, the Nuclear Compton Telescope (NCT), which is capable of measuring GRB polarization. NCT uses planar cross-strip germanium detectors for Compton imaging (200 keV–10 MeV) and polarimetry (200 keV–2 MeV). Chapter 5 describes NCT and its flight history.

In Chapter 6, I discuss calibrations of the effective area of NCT during the 2009 New Mexico and 2010 Australia balloon campaigns. By placing radioactive sources of known activity throughout the NCT field of view, it is possible to determine the efficiency of the telescope. I compare these values to those derived from detailed Monte Carlo simulations. The values derived from the real data show a roughly constant deficit relative to those derived from the Monte Carlo simulations which may be related to known deficiencies in the lower-level event calibrations.

Chapter 7 assesses NCT's polarimetric performance. I generated partially polarized beams throughout NCT's field of view by scattering photons off of a scintillator slab triggered in coincidence with the NCT detectors. The measured polarimetric modulation showed good agreement with Monte Carlo simulations for some calibrations, although systematic geometric effects are present. NCT's polarimetric performance compares well to that of other Compton telescopes.

Finally, in Chapter 8 I calculate NCT's sensitivity to GRBs and expected detection rate. Using single-site and incompletely-absorbed events, NCT has about one-fourth the sensitivity of BATSE LAD. NCT could detect about half of the bursts in the BATSE catalog if they occurred in its field of view. Bursts bright enough for polarimetric analysis are too rare to detect effectively from a balloon platform, however, so a satellite instrument with NCT-like detectors would be needed to perform a useful census of GRB polarization.

Better understanding of the GRB prompt emission will clarify the place of GRBs in stellar life cycles, provide new insights into the physics of collisionless shocks and relativistic jets, and facilitate the use of GRBs as probes of the early universe and electromagnetic counterparts to gravitational wave and neutrino signals. The complex phenomenology of GRBs creates both a challenge and a rich opportunity to explain and utilize these enigmatic events.

To my parents, with gratitude.

“I own I can never look upon the stars without wondering why the whole world does not become astronomers; and that men endowed with sense and reason should neglect a science they are naturally so much interested in, and so capable of inlarging their understanding, as next to a demonstration must convince them of their immortality, and reconcile them to all those little difficulties incident to human nature, without the least anxiety.”

—Thomas Wright, *An Original Theory or New Hypothesis of the Universe*, 1750.

Contents

List of Figures

List of Tables

Acknowledgments

During the completion of this work, it has been my privilege to work with and learn from a great many uniquely talented individuals. I am grateful for their support and encouragement.

Sincere thanks to Prof. Steven Boggs, my adviser, for his guidance and support of my efforts throughout the Ph.D. program. His good humor and optimism were invaluable in the most challenging periods, and his generosity with opportunities encouraged my growth as a scientist.

Thanks also to the members of my dissertation committee, Prof. Robert Lin and Prof. Joshua Bloom, for their comments that improved the clarity of this work.

Members of the RHESSI GRB team were helpful guides as I learned about prompt GRB science. Kevin Hurley coordinated our efforts and provided access to data and collaborators that expanded the impact of this work. David Smith provided key insights into the performance of the RHESSI detectors. Claudia Wigger was my tutor in the intricacies of RHESSI data analysis and suggested key improvements in my methods. She and her family were warm and gracious hosts during my visit to the Paul Scherrer Institut in Switzerland. Independently, Nat Butler was a mentor to me in my early years; he was generous in sharing his code with me and awakened me to the potential of rigorously analyzed GRB data.

The emotional roller coaster of a balloon campaign forges deep bonds among all those involved. I am particularly grateful to our engineers for their hard work and expertise. Steve McBride was indispensable during the NCT campaigns; his engineering touched all aspects of NCT, and his tales of balloon launches past enlivened many meals at Fred's and Sadie's and on the Todd Mall. Jane Hoberman was tireless in ensuring that the electronics performed at the highest level; without her attention to detail, NCT could not have been so successful.

My fellow grad students were a band of brothers in the field. Foremost among them was Mark Bandstra, whose careful, clear solutions to technical problems I have relied on countless times throughout graduate school. I have tried to emulate his leadership on campaign and in life, and I am grateful for his friendship. Alan Chiu worked harder than anyone else over two campaigns while maintaining a steady cheerfulness that was crucial to our morale. His late nights coding produced highly capable GSE software, and his careful watchfulness made sure NCT was working correctly. Daniel Perez-Becker, Zhong-Kai Liu, Jau-Shian Liang, Wei-Che Hung, and Zach Pu also contributed their unique talents and a great deal of energy to NCT. Finally, Belinda Bandstra was a valuable part of the team in New Mexico, keeping

us well-supplied, well-fed, and moderately civilized.

The other members of the NCT team—Prof. Hsiang-Kuang Chang, Prof. Yuan-Hann Chang, Dr. C. H. Lin, and Prof. Alfred Huang—added valuable scientific and engineering experience to our collaboration. I appreciated their hospitality during my visit to Taiwan.

NCT's successes are grounded in the considerable expertise of members of the SSL and LBNL engineering and technical staff. Mark Amman, Bill Donakowski, Paul Turin, Yvette Irwin, and Terry McDonald made significant contributions of skill, effort, and ingenuity. Their professionalism continues to impress me.

I have great respect and admiration for the entire staff of the Columbia Scientific Ballooning Facility, and I am particularly grateful to Bill Stepp and Frank Candelaria for their efforts during the 2009 and 2010 NCT campaigns.

Harry Asher of the Sydney office of Concordia International Forwarding provided friendly and highly effective service directing the international shipment of the NCT equipment during the Australia campaign. His capable handling of our difficult cargo logistics removed a huge burden from me, and I will remember fondly my four-day ride across Australia with the NCT cryostat. I am also grateful to Ravi Sood for his management of the Alice Springs Balloon Launching Station.

Other members of the SSL gamma-ray astrophysics group have offered their ideas, companionship, and support on this scientific journey. Trixi Wunderer gave me many great suggestions for improving my analysis, and her commitment to rigorous science remains an inspiration. Andreas Zoglauer's masterful MEGAlib package undergirds all of the Compton analysis here; he deserves thanks for his patience as I learned to harness its power. Wayne Coburn wrote the first versions of the NCT flight code; my effort to understand it was an education in itself. Thanks also to John Tomsick, Emerah Kalemci, Arash Bodaghee, Nicolas Barrière, Philip von Doetinchem, Jason Bowen, Michelle Galloway, and Alex Lowell for many pleasant lunch conversations on topics scientific and otherwise.

I am particularly grateful to Anne Takizawa for her cheerful assistance with all the administrative details of the Physics graduate program. Her skillful guidance enabled me to navigate several bureaucratic rapids with ease.

My life in Berkeley has been blessed by good friends too numerous to name. I am especially thankful for the support of Fr. Charlie Donahue and all my Newman friends, as well as for good conversations with Andrew Ng, Brad Malone, Vasudha Shivamoggi, and Meredith Hughes.

My parents, Jim and Annette, as well as my brother Andrew have been a constant source of support and encouragement during my grad school years. Their phone calls, emails, cards, packages, and visits helped me maintain perspective. I will especially treasure my memories of working together with Dad on NCT in Australia—a bigger project than the model rockets we built together when I was younger!

Finally, my fiancée Cameron has brought incredible joy into my life. Her support of my work at the "space lab," her help during the NCT shipments, and her patience during my long months afield enabled me to persevere. I am filled with hope and excitement for our future together!

Chapter 1

Gamma-Ray Bursts

Abstract

Gamma-Ray Bursts (GRBs) produce tenths to hundreds of seconds of temporally irregular gamma-ray emission with smooth spectra peaking in the hundreds of keV. This initial "prompt" emission is followed by a long-wavelength afterglow that fades over several weeks. Redshift measurements of afterglows have confirmed that GRBs are located at cosmological distances, making them the most luminous objects in the universe. Decades of study have narrowed potential theories of GRB progenitors and emission mechanisms, but many questions remain open.

1.1 GRB Phenomenology

1.1.1 Prompt Emission

The eponymous "prompt" gamma-ray emission of GRBs was discovered serendipitously in 1967 by the Vela satellites monitoring Soviet compliance with the Nuclear Test Ban Treaty (Klebesadel et al. 1973). The characteristic multi-peaked, irregular temporal structure and variation in burst duration were readily observed (Figure 1.1). Through the 1970s and 1980s, observers obtained a larger sample of GRB lightcurves and spectra, and theories of GRB origins proliferated. However, the challenges of localizing such short-lived transients prevented significant progress.

The Burst and Transient Experiment (BATSE; Fishman et al. 1989) on the Compton Gamma-Ray Observatory (CGRO) provided improved energy spectra and degree-scale localization of a large burst sample. The sample's angular isotropy and spatial inhomogeneity gave credence to cosmological models of the burst origin (Meegan et al. 1992). Bimodality in the distribution of burst duration—defined by the time T_{90} spanning the interval in which

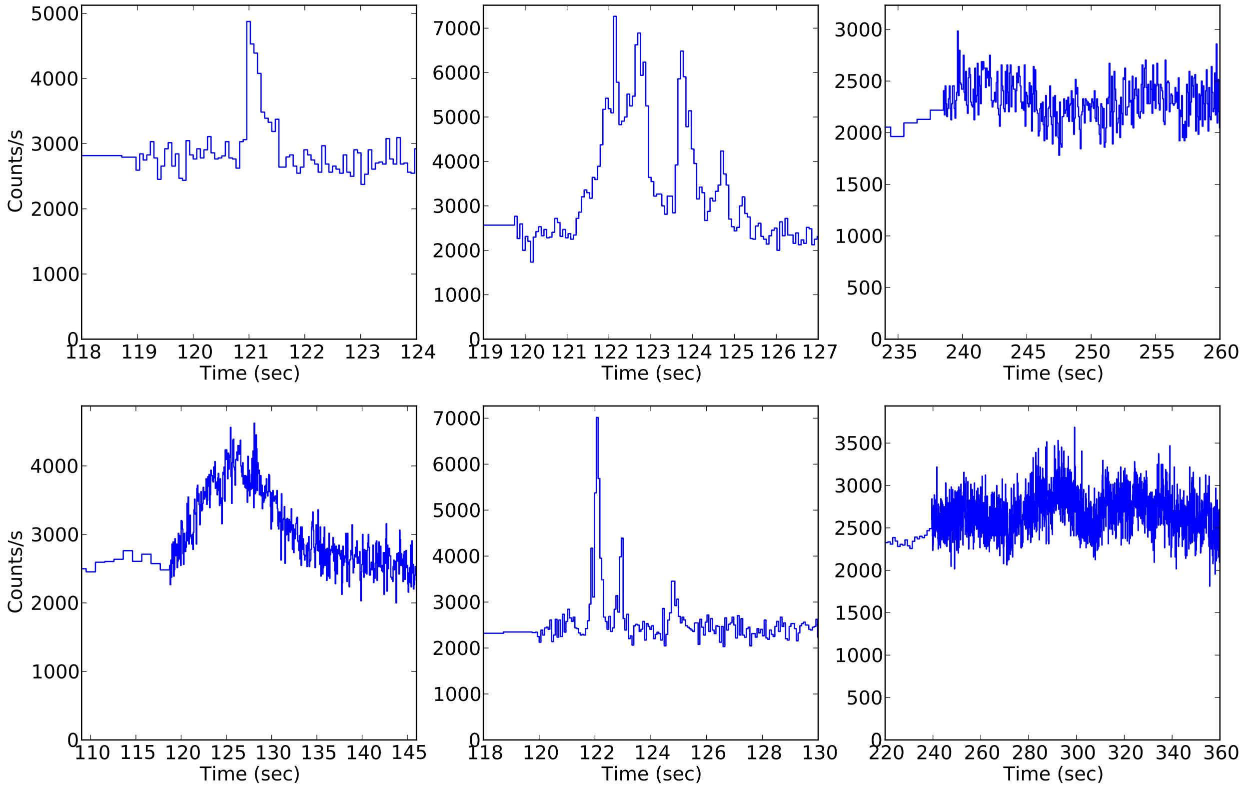

Figure 1.1: Example GRB prompt lightcurves (20–300 keV) selected from the December 1991 BATSE data.

5%–95% of the total observed counts were collected—suggested two classes of burst progenitors (Kouveliotou et al. 1993). The observed correlation between duration and spectral hardness led to the nomenclature "short–hard" and "long–soft" bursts, with a division at about 2 seconds[1] (Figure 1.2).

BATSE spectral analysis of GRBs showed smooth, apparently non-thermal spectra with νF_ν peak energies $E_{\rm peak}$ of several hundred keV (Band et al. 1993). The peak energy is correlated with intensity and typically shows a hard-to-soft temporal evolution (Ford et al. 1995; Figure 1.3).

In 1997, the discovery of the first afterglows (van Paradijs et al. 1997; Costa et al. 1997; Frail et al. 1997) and the measurement of GRB redshifts (Metzger et al. 1997) confirmed the cosmological origin of GRBs. Arcminute-precision localization by BeppoSAX (Boella et al. 1997), HETE-2, and the Interplanetary Network enabled detection of long-wavelength counterparts for increasing number of GRBs. The *Swift* satellite (Gehrels et al. 2004),

---

[1] The discovery of short bursts with tens to hundreds of seconds of soft extended emission following the initial hard spike has complicated this temporal division (Norris & Bonnell 2006; Bloom et al. 2008), and the proportion of bursts observed in each class varies with detector bandpass and triggering algorithm.

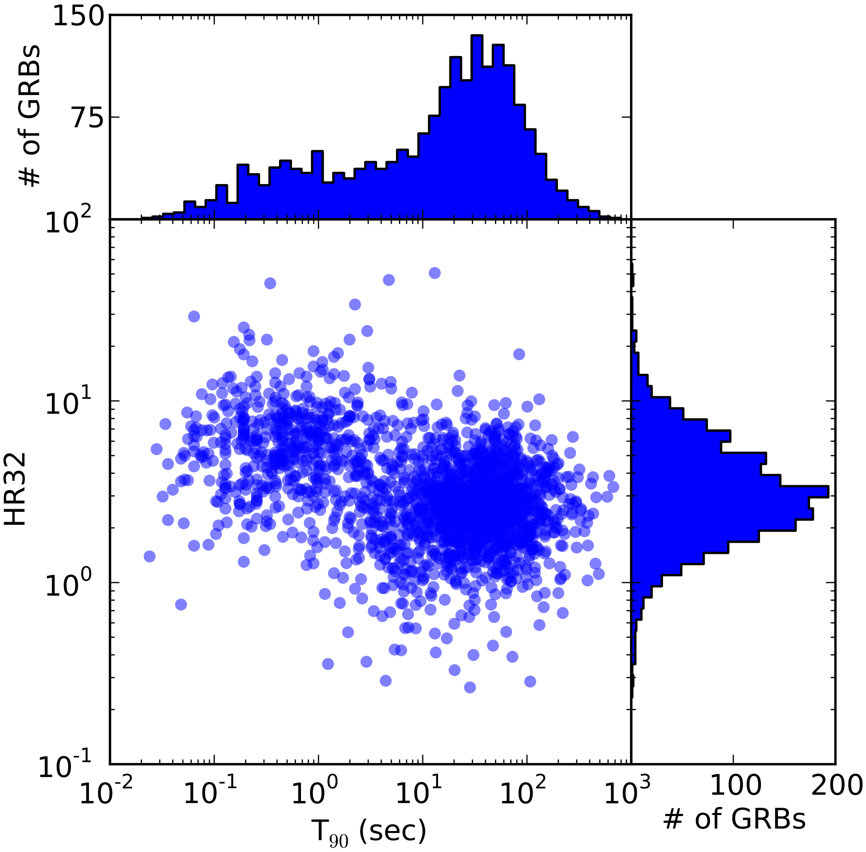

Figure 1.2: The hardness-duration plot for all BATSE bursts reveals two classes of GRBs. Duration is specified by T_{90}, while the hardness ratio is the ratio of the fluence in discriminator channels 3 (100–300 keV) and 2 (50–100 keV). Bimodality can be observed more readily in duration alone (top histogram) than in spectral hardness (right histogram).

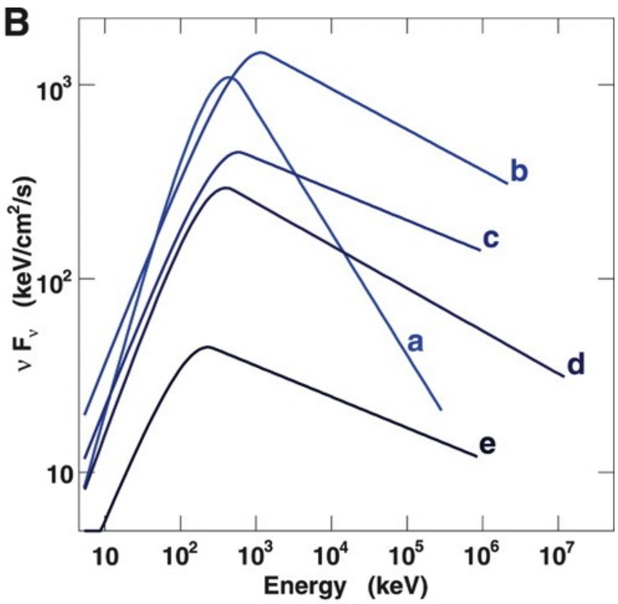

Figure 1.3: Example GRB spectral evolution for GRB 080916C (Figure 2b of Abdo et al. 2009b). The best-fit Band function spectra fit to the *Fermi* data are plotted in νF_ν space. After the initial interval (a), a hard-to-soft spectral evolution correlated with intensity occurs.

launched in 2004, has localized about 100 bursts per year with its rapid slewing capability. (Table 1.1 gives an overview of major GRB-detecting missions.)

The availability of GRB positions has enabled searches for prompt emission components in bands other than the gamma-ray. Simultaneous detections have been rare, however, and, determining whether such simultaneous multi-wavelength data is due to prompt or afterglow emission presents a significant interpretive challenge.

Akerlof et al. (1999) reported the first detection of optical emission during the prompt phase of GRB 990123 with the ROTSE-I robotic imager. GRB 041219a was detected in the optical (Vestrand et al. 2005) and infrared (Blake et al. 2005). The small precursor of GRB 061121 triggered *Swift*-BAT and enabled UVOT observations during the primary burst phase (Page et al. 2007). Fortuitous positioning of the "naked-eye" GRB 080319B near the previous GRB detected by *Swift* enabled high-cadence optical observations contemporaneous with the prompt gamma-rays (Bloom et al. 2009; Racusin et al. 2008). The optical emission from this burst peaked at magnitude 5.3. For all these bursts, the optical/IR lightcurves showed general correspondence with the prompt gamma-rays, but the detailed variability in the two bands showed less correlation. In other cases, such as GRBs 060124 (Romano et al. 2006) and 091024 (Gruber et al. 2011), the behavior of the optical emission is generally independent of the prompt gamma-rays.

With the EGRET pair telescope on CGRO, Hurley et al. (1994) observed GeV photons contemporaneous with and up to 5700 seconds after the long GRB 940217. Additionally, for some bright bursts, EGRET observed hard high-energy (10–200 MeV) spectral features

Mission	Years of operation	Instrument	Energy Band (keV)	Major Results
Vela	1965–1984	(multiple satellites)	200–1500	GRB discovery and prompt morphology
CGRO	1991–2000	BATSE	20–8000	Largest GRB sample; isotropy;
		EGRET	20 MeV–80 GeV	long and short bursts; Band function spectra
BeppoSAX	1996–2002	GRBM	40–700	Localization of first afterglows
		WFC	2–28	
		NFI	0.1–300	
HETE-2	2001–2006	FREGATE	6–400	X-Ray Flashes and X-Ray Rich GRBs
		WXM	2–25	
		SXC	0.5–10	
Swift	2004–	BAT	15–150	Best-localized sample; early X-ray afterglows
		XRT	0.2–10	
		UVOT	170–650 nm	
Fermi	2008–	LAT	20 MeV–>300 GeV	Properties of GeV emission
		GBM	3 keV–30 MeV	

Table 1.1: Major GRB-detecting satellites.

(González et al. 2003; Kaneko et al. 2008). These reports have been confirmed by *Fermi*-LAT (Atwood et al. 2009), which has observed high energy components in the spectra of the brightest long (Abdo et al. 2009a; Ackermann et al. 2011) and short (Ackermann et al. 2010) GRBs. For the bright GRB 080916c, however, the data were consistent with a Band-only spectrum (Abdo et al. 2009b). Notably, the high energy component of GRB 090926A showed evidence of a cutoff at 1.4 GeV (Ackermann et al. 2011).

The Milagrito telescope reported a statistically significant excess of TeV gamma-rays during the prompt phase of GRB 970417A (Atkins et al. 2000). However, no other GRBs to date have been detected at very high gamma-ray energies (VHE) in the prompt or afterglow phases despite increasingly sensitive searches (Atkins et al. 2005; Abdo et al. 2007; Aharonian et al. 2009; Jarvis et al. 2010).

Polarimetric measurements of the prompt emission are in their infancy, but such data may constrain emission models and probe the structure of the emitting region (Toma et al. 2009). Polarization data may be obtained by instruments utilizing the Compton scattering of gamma-rays (Lei et al. 1997) or potentially in the X-ray band by gaseous Time Projection Chambers which track the ejected photoelectron (Black et al. 2007). Measurements of GRB polarization to date by general-purpose instruments have been limited to the brightest bursts and troubled by systematic effects. Coburn & Boggs (2003) reported a high linear polarization ($\Pi = 80 \pm 20\%$) for RHESSI data from GRB 021206. Subsequent analysis using different event cuts suggested that the RHESSI data could not constrain the polarization (Wigger et al. 2004), highlighting the challenges of the analysis. Additional reports of GRB polarization have been reported using INTEGRAL-SPI (Kalemci et al. 2007; McGlynn et al. 2007) and INTEGRAL-IBIS (Götz et al. 2009) as well as using BATSE observations of scattered albedo photons (Willis et al. 2005). These studies reported prompt polarization fractions greater than 50%, but the large detectors and lack of calibration required reliance on extensive Monte Carlo simulations, which may be less reliable for correcting false modulation (Bloser et al. 2009). Progress will require a larger sample of bursts obtained by a well-calibrated satellite polarimeter. Several potential approaches have been developed as balloon instruments (Boggs et al. 2004; Bloser et al. 2009; Krawczynski et al. 2009).

1.1.2 Afterglow

The first long-wavelength afterglows of long GRBs were observed in 1997 (van Paradijs et al. 1997; Costa et al. 1997; Frail et al. 1997). Regular observations of afterglows in all bands followed. Short GRB afterglows were first observed in 2005 (Gehrels et al. 2005; Fox et al. 2005; Hjorth et al. 2005b; Berger et al. 2005), as they are generally dimmer by an order of magnitude (Nakar 2007). GRB afterglows have less temporal and spectral variability than the prompt emission, fading smoothly over weeks to months. Afterglow observations continue to enable new insights into the complex physics of GRBs, including studies of their host galaxies and redshift distribution, their connection to supernovae (SNe), and their interaction with the circumburst environment.

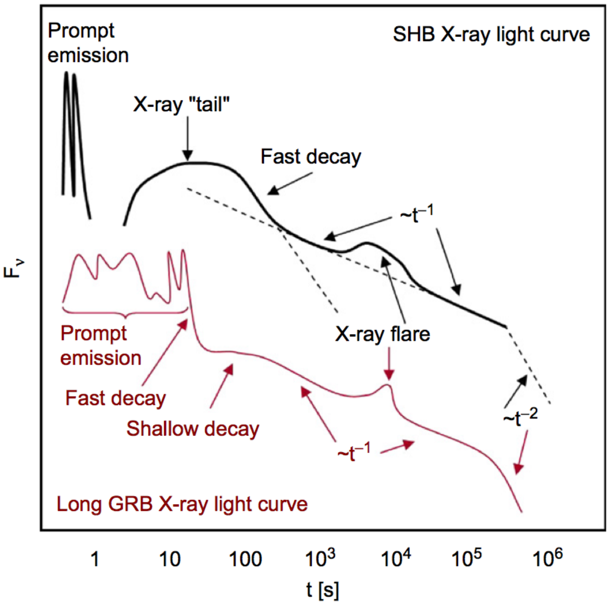

Figure 1.4: Characteristic X-ray afterglow light curves for short (black) and long (red) bursts (Figure 4 of Nakar 2007).

X-ray

Long GRB X-ray afterglows were first observed by BeppoSAX (Costa et al. 1997), but the large sample of early-time afterglows enabled by *Swift*'s rapid slewing capability revealed a complex but characteristic behavior (Nousek et al. 2006; Figure 1.4). A steep ($\propto t^{-3}$ or steeper) initial flux decline lasting hundreds of seconds follows the end of the prompt phase before slowing into a plateau phase ($\propto t^{-0.5}$ to t^{-1}) typically lasting 10^3–10^4 s. The steep-to-plateau transition is typically marked by a change in the spectral index. After the plateau, the light curve enters a shallow decay phase ($\propto t^{-1}$ to $t^{-1.5}$) lasting until late times. The final decay phase sometimes breaks and steepens.

In some cases, large X-ray flares interrupt the smooth decay. Generally the flares appear to be late, soft spikes similar to the prompt emission (Butler & Kocevski 2007; Krimm et al. 2007). The low-energy sensitivity of HETE-2 enabled earlier observations of X-Ray Flashes (XRFs) and X-Ray Rich GRBs (XRRs) (Sakamoto et al. 2005) in similar numbers as normal GRBs, suggesting that even in the classical prompt phase the observed dominance of gamma-ray emission over X-ray emission may be influenced by detector thresholds.

For short bursts, the X-ray afterglow typically begins with an X-ray tail lasting ~100 s; sometimes the tail produces extended emission in the gamma-ray band (Norris & Bonnell 2006). A fast decay phase then transitions into a gradual ($\sim t^{-1}$) decay similar to that observed for long bursts, with X-ray flares and late temporal breaks occasionally observed (Figure 1.4).

Optical

Long GRB afterglows in the optical bands are characterized several hundred seconds of flat or rising emission followed by gradual power-law decays $t^{-\alpha}$, with decay indices of $-0.5 < \alpha \lesssim -1.2$ (Oates et al. 2009). Power-law spectra are also the norm. Typical visual magnitudes of long bursts one day after the burst are 19–20.

Some, but not all, optical lightcurves show temporal breaks to steeper slopes $\alpha \approx 2.0$ in the days after the burst. Previous theoretical expectations (Section 1.2.1) and early observations (e.g., Harrison et al. 1999) suggested that the decaying afterglow lightcurves should show breaks in all bands at the same time–"achromatic breaks." Instead, chromatic breaks are commonly observed, with breaks occurring at different times or not at all in the various bands (e.g., Liang et al. 2008). Accounting for chromatic breaks poses a significant challenge for existing GRB jet models.

A significant fraction of GRBs, referred to as "optically dark," have no detected optical counterparts. Forty percent of the *Swift* GRB sample have no reported optical detection by *Swift*-UVOT or ground-based telescopes despite the early-time observations and precise localizations enabled by *Swift* (Roming et al. 2009). Deep observations of the host galaxies of dark GRBs suggest that dust extinction is the primary cause of the dark bursts rather than high redshift or observational biases (Perley et al. 2009).

Radio

Radio afterglow measurements are obtained less frequently than observations in other bands due to constraints on available telescope time. However, radio measurements have enabled significant advances in understanding the physics of the afterglow emission, including identifying signatures of relativistic motion and allowing calorimetry of the total burst energetics (Section 1.2.1). Radio observations have also played a key role in detailed broadband afterglow models of bright GRBs (e.g., Chandra et al. 2008).

GeV–TeV Gamma Rays

High-energy gamma-rays (tens of MeV–GeV) occur contemporaneously with the MeV prompt emission (Section 1.1.1) with temporal correlations suggesting some of the emission has a common origin (e.g., Ackermann et al. 2011). However, high energy components have been observed to persist after the prompt emission, complicating the division of prompt and afterglow emission. Hurley et al. (1994) observed an 18 GeV photon 5700 seconds after GRB 940217. Time-resolved spectral analysis of GRB 941017 by González et al. (2003) found the high-energy spectral component increased in strength as the MeV prompt component weakened. Finally, *Fermi*-LAT has observed that emission in the LAT band starts later and lasts longer than that at lower energies (Ackermann et al. 2011, and references therein).

No afterglow detections at TeV energies have been made yet (Atkins et al. 2005; Abdo et al. 2007; Aharonian et al. 2009; Jarvis et al. 2010).

1.1.3 Multi-messenger

To date, no gravitational wave (GW) or neutrino counterpart to the electromagnetic (EM) emission of GRBs has been detected. In the most extensive survey, Abbott et al. (2010) searched GW data from the LIGO and VIRGO observatories, finding no significant signals coincident with 137 GRBs. However, even GW upper limits have proven valuable: non-detection of GW signals from GRB 070201, which had a localization consistent with an origin in M31, ruled out a coalescing compact binary progenitor, assuming the GRB was indeed located in M31 (Abbott et al. 2008b). GW detections of GRBs are expected in this decade. The most favored candidate for the progenitors of short GRBs, compact binary mergers, are potentially observable by the next-generation gravitational wave observatories Advanced LIGO and Advanced VIRGO (Abbott et al. 2008a).

Cubic kilometer neutrino observatories such as IceCube are beginning operations with sensitivity sufficient to detect neutrinos generated in the GRB fireball. A recent report (IceCube Collaboration et al. 2011) of non-detection of neutrinos from 117 GRBs excludes basic fireball models (Waxman & Bahcall 1997) at 90% C.L.

1.2 Theories of GRBs

The complexity of GRB phenomenology has made it difficult to build unified, predictive theories of GRBs. Some features of an eventual unified GRB theory are established by strong evidence, such as the presence of relativistic jets and the connection between long GRBs and Type Ibc supernovae. However, in other areas there remains little productive confrontation between theory and observation.

1.2.1 Jets and Energetics

Several independent pieces of evidence indicate that GRB emission is the product of relativistic jets.

The presence of a significant flux of (apparently) non-thermal radiation at MeV energies and above creates a so-called "compactness problem." If a nonrelativistic source emits photons with temporal features of size δt, causality requires the physical size of the emitting region to be $\sim c\delta t$. The corresponding optical depth of MeV photons to $\gamma\gamma \rightarrow e^{\pm}$ is huge: $\tau_{\gamma\gamma} \sim 10^{15}$ (Piran 2004, and references therein). If the prompt emitting region is moving relativistically with bulk Lorentz factor Γ, however, two effects mitigate the compactness problem. In the source frame, the energies of the photons are lower than those observed by a factor of Γ. Also, the size of the emitting region increases to $\Gamma^2 c\delta t$. Observations of prompt GRB emission can thus be used to set constraints on the minimum Lorentz factor, with $\Gamma \gtrsim 100$ (e.g., Lithwick & Sari 2001).

Observations of radio scintillation in GRB afterglows have allowed direct measurement of relativistic expansion rates. The radio afterglow measurements of Frail et al. (1997) oscillated in a manner consistent with interstellar scattering; the size of the source at two weeks was 10^{17} cm and the expansion mildly relativistic. Taylor et al. (2004) used the VLBI to resolve images of the radio afterglow of GRB 030329 between 20 and 100 days after the burst, finding its size and proper motion consistent with a relativistic outflow.

With the realization that GRBs are located at cosmological distances, it became apparent that the implied energetics were pushing the limits of stellar-mass progenitors. The energy in prompt gamma-rays assuming isotropic emission (E_{iso}) for some bursts was 10^{53}–10^{54} erg (e.g., Kulkarni et al. 1998a, 1999). If the GRB emission were collimated in relativistic jets, however, this problem would be avoided: the isotropic energy release would be reduced by the fraction of the solid angle subtended by the jet (Rhoads 1997). The jet model predicted achromatic temporal breaks in the afterglow light curve: initially, relativistic beaming would restrict afterglow observations to a subset of the jet. As the jet slowed, however, eventually the edge of the jet would become visible and the decay index would increase. This transition occurs when $\Gamma \sim 1/\theta_j$, where θ_j is the jet opening angle. By measuring the time of the afterglow breaks, the jet opening angles could be inferred (Sari et al. 1999). Early results found that the beaming-corrected energies E_γ of long GRBs clustered tightly at 10^{51} erg (Frail et al. 2001; Bloom et al. 2003), suggesting a single class of stellar-mass progenitors.

Since the launch of *Swift*, the initial clarity of this picture of GRB jets and energetics has been muddied. First, the overwhelming majority of GRBs show afterglow breaks that are chromatic between the X-ray and optical bands, with the X-ray breaks occurring earlier (e.g., Liang et al. 2008). These results are difficult to accommodate within standard jet models. Multiple-component jets have been proposed in order to accommodate some observations (Racusin et al. 2008). Another possibility is that the observed breaks in the X-ray light curves due to effects other than jet physics (perhaps contribution from "late prompt" emission: Ghisellini et al. 2007) and the true jet breaks are occurring at late times and are undetected (Kocevski & Butler 2008).

Second, some bursts with measured jet breaks appear sub- or super-energetic compared to initial estimates. Detailed broadband modeling of bright *Swift* GRBs has found several bursts with collimation-corrected energy release greater than 10^{52} erg (Chandra et al. 2008; Bellm et al. 2008b; Cenko et al. 2010). The nearest GRBs, however, have energetics orders of magnitude lower than typical GRBs (Kulkarni et al. 1998b; Bloom et al. 2001; Soderberg et al. 2004, 2006a).

The classical analytic jet models which assume an on-axis observer may impose distortions, however. Recent simulations suggest that the true energy of a burst measured by an off-axis observer will be as much as a factor of four smaller than that implied by on-axis models (van Eerten et al. 2010). Moreover, jet breaks in the radio regime should be delayed relative to the X-ray/optical breaks due to self-absorption effects, creating chromatic breaks (van Eerten et al. 2011).

Another approach may yield energy estimates which are less sensitive to jet models. Late-time radio measurements can allow for accurate calorimetry of GRB energetics by observing the outflow once it transitions to the non-relativistic, spherically symmetric Sedov-Taylor regime. Previous efforts found values of E_K, the total kinetic energy of the explosion, of 0.5–3 × 10^{51} erg for GRBs 970508 (Frail et al. 2000), 980703 (Berger et al. 2004), and

030329 (Frail et al. 2005; van der Horst et al. 2008). Shivvers & Berger (2011) generated similar constraints using sparsely-sampled radio data, finding a 90% C.L. range of E_K of 1.1×10^{50}–3.3×10^{53}, somewhat higher than determined by late-time calorimetry or broadband modeling. Future observations with the EVLA will allow regular determination of the burst energetics with moderate use of telescope time (Shivvers & Berger 2011).

1.2.2 Progenitors

Long GRBs

Observational evidence linking long GRBs with core-collapse SNe appeared soon after the first afterglow detections (for a review, see Woosley & Bloom 2006). The first evidence was provided by the temporal and spatial coincidence of GRB 980425 and SN 1998bw (Galama et al. 1998). Late-time bumps observed in some afterglows beginning with GRB 980326 (Bloom et al. 1999) suggested emerging SN light curves, although re-brightening due to dust effects was also plausible (Esin & Blandford 2000; Waxman & Draine 2000). Spectroscopic observations of the afterglow of the bright, nearby GRB 030329 confirmed the link (Stanek et al. 2003): the spectral evolution of the associated SN 2003dh showed clear correspondence to SN 1998bw (Hjorth et al. 2003). Since then, associated SNe have been regularly detected for nearby GRBs (e.g., Malesani et al. 2004; Campana et al. 2006; Starling et al. 2011). Two nearby bursts, GRBs 060505 and 060614, showed no underlying SNe to deep limits (Gehrels et al. 2006; Della Valle et al. 2006; Fynbo et al. 2006), but their prompt emission may be construed as that of a short burst (060505) or a short burst with extended emission (060614) (Nakar 2007, and references therein).

Short GRBs

Evidence clearly indicates that short and long bursts have different progenitors. For nearby short bursts, associated SNe have been ruled out to deep limits (Hjorth et al. 2005a; Fox et al. 2005; Soderberg et al. 2006b). Moreover, studies of GRB host galaxies have shown that short GRBs are associated with older stellar populations (Berger 2011, and references therein). As expected for a massive star origin, long GRBs occur predominately in regions of high star formation in late-type galaxies. Short GRBs occur in both early and late galaxies.

Compact binary mergers have long been a popular candidate for short GRB progenitors (e.g., Paczynski 1986; Eichler et al. 1989; Narayan et al. 1992). While current evidence from host galaxy types and burst environments is consistent with this theory (Berger 2011), confirmation of the merger origin of short GRBs will likely result from gravitational wave detection, potentially by Advanced LIGO and Advanced VIRGO (Abbott et al. 2008a).

In addition to the binary merger channel, accretion-induced collapse (AIC; Nomoto & Kondo 1991) of a white dwarf to a protomagnetar was proposed by Metzger et al. (2008) as a progenitor of short bursts with extended emission. MacFadyen et al. (2005) suggested the AIC of a neutron star to a black hole could produce short bursts as well.

Some fraction of observed short GRBs may be due to extragalactic giant flares from Soft Gamma Repeaters. In particular, had the Dec. 27, 2004 giant flare of SGR 1806–20 occurred within a distance of $\sim$40 Mpc, its hard initial spike would have resembled a conventional short GRB (Hurley et al. 2005; Palmer et al. 2005). The soft, oscillating tail of SGR giant flares is also suggestive of the short GRB extended emission observed by BATSE, HETE-2, and *Swift* (Norris & Bonnell 2006). GRBs 051103 and 070201 were suggested as possible candidates for an SGR origin, as their large localization error boxes included nearby galaxies (Hurley et al. 2010; Mazets et al. 2008; Ofek et al. 2008). For GRB 070201, the non-detection of gravitational waves ruled out a binary merger if the GRB was actually located in M31 (Abbott et al. 2008b).

Due to the unknown luminosity distribution of SGR giant flares, the contribution of giant flares to the observed short GRB rate is uncertain. Ofek (2007) used the number of observed associations of IPN error boxes with nearby galaxies to place an upper limit of 16% on the fraction of SGRs in the overall short GRB sample, while the Galactic SGR rate requires a lower limit of 1%. Observations of the pulsating X-ray tail, of the localized source in quiescence, or of repeated bursts from the same source would be needed to confirm an SGR origin for a specific burst.

1.2.3 Central Engines

The central engines which power GRBs must generate prodigious energy releases within timescales of a few to tens of seconds. They must produce collimated, relativistic outflows with minimal baryon loads in order to reach the high Lorentz factors required by observations. Two major models for the energy source and release have been explored: gravitational, produced by rapid accretion onto a newly-formed black hole (BH), and magneto-rotational, by means of the outflows of a highly magnetized, rapidly rotating proto-neutron star (PNS): a "millisecond magnetar."

The "collapsar" scenario was first proposed by for failed SNe (Woosley 1993), then developed further in the context of highly-energetic "hypernovae" like SN 1998bw (MacFadyen & Woosley 1999; MacFadyen et al. 2001). The collapse of the iron core during the SN explosion of a fast-rotating massive star (Woosley & Heger 2006) either produces a BH directly or after a period of fallback accretion onto a NS. (Accretion onto a newly formed BH may also occur after binary mergers, potentially producing short GRBs (Lee & Ramirez-Ruiz 2007).) Due to the fast rotation, an optically thick, neutrino-cooled accretion disk forms around the BH and produces jets carrying some fraction of the energy released by rapid accretion. Many of the details of the accretion disk formation and cooling remain uncertain, and the viability of the process is sensitive to the assumed initial conditions (e.g., Lee & Ramirez-Ruiz 2007; Taylor et al. 2011, and references therein).

Simulations initiated subsequent to BH formation show that collapsar jets can break out of the stellar envelope, potentially generating the observed GRB emission (MacFadyen & Woosley 1999; MacFadyen et al. 2001). Recent simulations have suggested, however, that accretion onto the neutron star formed after core collapse may not produce a black hole (Dessart et al. 2008). Instead, the neutron star loses mass through a magnetically driven baryonic jet. This result, if proven durable for a range of relevant initial conditions, challenges the key assumption of black hole formation in the collapsar model.

Usov (1992) recognized that a newly born rapidly rotating magnetar could generate a relativistic electron-positron fireball leading to the observed emission. The original model proposed that the NS formed due to AIC of a white dwarf (WD). With the well-established connection between core-collapse SNe and long GRBs, present theoretical efforts (Metzger et al. 2010, and references therein) focus on magnetars produced during the core collapse of massive stars. (Other formation channels remain plausible, including WD AIC and WD-WD or NS-NS binary mergers (Metzger et al. 2008); these scenarios may be relevant for short bursts.)

In this scenario, core collapse generates a SN shock and a newly-born magnetar with a large magnetic field ($\sim 10^{15}$ G) and short period (∼ms). As the NS cools over the Kelvin-Helmholtz timescale (10–100 s), neutrino-driven mass loss clears baryons from the NS. As the NS cools, the wind becomes increasingly magnetized and the magnetar produces a relativistic wind through magneto-centrifugal slinging (Thompson et al. 2004). This wind is collimated by magnetic hoop stresses in the stellar envelope, breaking out of the stellar surface in bipolar jets (Bucciantini et al. 2007, 2008, 2009). The observed GRB emission is then produced by internal shocks or magnetic dissipation (Section 1.2.4).

MHD simulations of these processes have shown the viability of this model, producing relativistic jets from an initial protomagnetar within a preexisting SN shock without additional tuning (Bucciantini et al. 2009). The light curve generated by the model, while far smoother than that of observed bursts, is comparable in duration (Metzger et al. 2008). The remnant magnetar may also be capable of producing the observed X-ray flares and other late-time activity.

One challenge for the magnetar model is the upper limit it implies on the GRB energy release. While the gravitational binding energy of the NS is $\sim 5 \times 10^{53}$ ergs, losses due to gravitational waves may put the available rotational energy for fast-rotating NS an order of magnitude lower (Thompson et al. 2010). While jet modeling remains uncertain (Section 1.2.1), some energetic bursts have collimation-corrected energy releases in excess of these values (e.g., Cenko et al. 2010). Improved three-dimensional MHD simulations should help clarify whether the protomagnetar model can generate the range of phenomenology observed by GRBs.

1.2.4 Prompt Emission Mechanisms

Without a well-established central engine model, it is necessary to make assumptions and parametrize ignorance when modeling the origin of the prompt emission. Key questions include: What is the composition and magnetization of the ejecta? How is the energy of the relativistic bulk motion (or Poynting flux) of the GRB jet dissipated? What radiative processes produce the observed broadband emission?

Outflow Composition and Dissipation

Three classes of models have been discussed in the literature, varying in their relative magnetization. In the fireball model, magnetic fields are dynamically unimportant and energy is carried by the bulk motion of a pair plasma (e.g., Piran 2004). At the other extreme, in electromagnetic models the magnetic energy density dominates the relativistic flow (Lyutikov & Blandford 2003; Lyutikov 2006). In the intermediate regime magnetic fields are dynamically important and MHD approximations apply (Spruit et al. 2001; Drenkhahn & Spruit 2002; Zhang & Yan 2011).

"Internal shocks" (Rees & Meszaros 1994) are the most popular dissipation mechanism in models containing non-magnetized "fireball" outflows. In the internal shocks scenario, variable activity from the central engine produces shells of ejecta with varying Lorentz factors. Faster shells overtake slower ones and collide. Fermi acceleration due to repeated shock crossings during the resulting collisionless shocks produces populations of accelerated electrons which may then radiate. Simulations support theoretical proposals (Blandford & Eichler 1987) that the Weibel instability can mediate relativistic collisionless shocks in non-magnetized plasmas and accelerate a nonthermal power-law distribution of electrons (Spitkovsky 2008a,b).

The internal shocks model is capable of producing the observed variability of GRB light curves (Sari & Piran 1997), and the central engine activity which produces the shells could produce late X-ray flares. However, the low efficiency of the internal shocks model (∼1%; Kumar 1999) requires a larger energy budget from the central engine.

If the outflow is Poynting flux-dominated, magnetic dissipation may accelerate a population of electrons with higher efficiency than shock acceleration. The mechanisms for such dissipation are highly uncertain, particularly in relativistic outflows. The data used to study reconnection are generally from solar flares, the terrestrial magnetosphere, and laboratory plasmas (Zweibel & Yamada 2009; Yamada et al. 2010); the conditions in these plasmas are quite different from those in GRB outflows, limiting the applicability of the results (Uzdensky 2011). Still, preliminary theoretical efforts have explored acceleration scenarios including the relevant relativistic and radiative effects (Lyutikov & Uzdensky 2003; Lyubarsky 2005; Uzdensky & McKinney 2010) and their application in the context of GRBs (e.g., Drenkhahn & Spruit 2002; Giannios 2006, 2008; McKinney & Uzdensky 2010). So far, magnetic dissipation scenarios remain a viable means of particle acceleration for GRBs and an active area of research.

Emission Mechanism

Synchrotron emission is the obvious candidate for the prompt emission mechanism (Meszaros et al. 1994; Lloyd & Petrosian 2000), given the apparently non-thermal spectra and the likelihood that the source region contains magnetic fields and a population of relativistic electrons. A challenge for pure synchrotron models is that some observed low-energy spectral slopes ($\alpha > -2/3$; Preece et al. 1998a; Ghirlanda et al. 2002) are impossible to achieve with optically thin synchrotron emission (Katz 1994; Ghisellini et al. 2000). Violations of this "line of death" may be accounted for, however, if typical assumptions about self-absorption, electron pitch angle, and electron population do not hold (Lloyd & Petrosian 2000; Lloyd-Ronning & Petrosian 2002).

Compton scattering may modify a source synchrotron spectrum. Even moderate Inverse Compton cooling of the source electrons may produce low-energy spectral indices in line with observations (Daigne et al. 2011). Models including Synchrotron Self-Compton (SSC) effects (Panaitescu & Mészáros 2000; Kumar & McMahon 2008) have a larger phase space than synchrotron-only models. These models predict bright emission in the optical band, however, which is only occasionally observed (Kumar & Panaitescu 2008; Roming et al. 2009).

If the magnetic fields in the shocked region are not constant nor dynamically large, the emitted radiation may be altered. Medvedev (2000) proposed "jitter radiation" may occur if the magnetic fields are chaotic on lengths less than the Larmor radius. However, recent simulations (Sironi & Spitkovsky 2009) suggest that this field configuration is unlikely for GRB-relevant shocks. The low-energy synchrotron spectrum is also altered if the ordered magnetic fields decay on scales much smaller than that of the outflow (Pe'er & Zhang 2006).

Despite the smooth spectra of GRBs, some authors have proposed that there may be thermal contributions from the GRB photosphere. Time-resolved spectral fits of BATSE bursts with hard low-energy emission were consistent with black-body emission (Preece 2000). Ryde (2005) found that a model consisting of a black body plus a power-law approximating the nonthermal emission could fit spectra of most BATSE bursts. This simple model is less successful in a wider energy band, however (Chapter 4). Realistic treatment of the interaction of the thermal and nonthermal radiation requires numerical modeling; such models can reproduce *Fermi* spectra with fiducial parameters (Pe'er et al. 2010).

1.2.5 Afterglow Emission Mechanisms

Since the emission processes producing the prompt emission do not dissipate all of the energy of the burst, the final stage of the GRB occurs when the outflow collides with the surrounding medium, eventually slowing. This "external shock" interaction produces a "forward shock" of the ejecta on the medium as well as a "reverse shock" on the ejecta itself.

The forward shock is expected to generate the late-time afterglow emission (Meszaros & Rees 1997). After an initial radiative phase (Cohen et al. 1998), the shock becomes adiabatic and its propagation is described by the relativistic self-similar solution of Blandford & McKee (1976). The expansion transitions into the nonrelativistic Sedov-Taylor phase on a timescale of years.

Synchrotron emission is the likely afterglow emission mechanism. The observed power-law spectra and light curves may be interpreted naturally in terms of the hydrodynamic evolution of the shock and the spectral break frequencies of the synchrotron emission (Sari et al. 1998; for a detailed review, see Piran 2004). Under the simplest assumptions, the accelerated electrons are assumed to have Lorentz factors distributed as a power law with index p above a minimum value γ_m. The uncertain energy density in electrons and magnetic fields is parametrized (ϵ_e and ϵ_B) and assumed to be constant.

The resulting spectrum consists of power-law segments $F_\nu \propto \nu^{-\beta}$, with breaks at key frequencies: ν_{sa}, the self-absorption frequency; ν_m, the frequency of emission from electrons with the minimum Lorentz factor γ_m; and ν_c, the cooling frequency. In the initial fast-cooling regime lasting ∼hours, the break frequencies are ordered $\nu_c < \nu_m$. Afterward, the slow cooling regime begins, with $\nu_m < \nu_c$. (During fast cooling, an additional spectral break, ν_{ac}, results from the population of uncooled electrons (Granot et al. 2000).) The time evolution of the flux using the hydrodynamics of the Blandford-McKee self-similar solution similarly produces power law segments: $F_\nu \propto t^{-\alpha}\nu^{-\beta}$, with the indices α varying depending on the density profile of the surrounding medium and whether the shock evolution is adiabatic or radiative. Figure 1.5 shows the spectral and temporal slopes for a variety of configurations. At late times, jet effects influence the observed light curve (Sari et al. 1999; Section 1.2.1).

Various effects may complicate this picture, including late-time energy injection ("refreshed shocks") (Rees & Meszaros 1998), an inhomogeneous external medium (e.g., Wang & Loeb 2000; Lazzati et al. 2002), or structure or inhomogeneity within the jet itself (e.g., Meszaros et al. 1998; Zhang & Mészáros 2002; Nakar et al. 2003; Racusin et al. 2008).

In the fireball model, the existence of the reverse shock predicts a bright optical flash (Sari & Piran 1999). Initial observations of early optical emission lent credence to this model (Akerlof et al. 1999), but bright optical flashes have been rare in the *Swift* era despite the regular coverage by *Swift*-UVOT (Roming et al. 2009). In contrast, Poynting-flux dominated models of the outflow predict negligible reverse shocks and optical flashes (Lyutikov 2006). Compton scattering of the optical photons could explain the lack of observed optical flashes, but the up-scattered photons should be observed by *Fermi* (Beloborodov 2005; Kobayashi et al. 2007).

Understanding of the complex features of the early-time afterglow, including multiple breaks, flares, and plateaus (Section 1.1.2), remains elusive. A variety of explanations have been advanced for these features (for a review, see Zhang 2007). Due to their similarity with spikes in the prompt emission (Butler & Kocevski 2007; Krimm et al. 2007), X-ray flares are generally attributed to late-time activity of the central engine (Burrows et al. 2005; Zhang et al. 2006). The steep decline seen in the X-ray afterglows may be interpreted as the "curvature effect" caused by propagation delays for off-axis emission (Fenimore et al. 1996; Panaitescu et al. 2006; Zhang et al. 2006). The origin of the plateau or shallow decay phase is harder to discern; current explanations include additional energy injection into the shock (Panaitescu et al. 2006; Nousek et al. 2006), jet effects (Eichler & Granot 2006; Granot et al. 2006; Toma et al. 2006), and time-varying microphysical parameters (Granot et al. 2006; Fan & Piran 2006; Ioka et al. 2006).

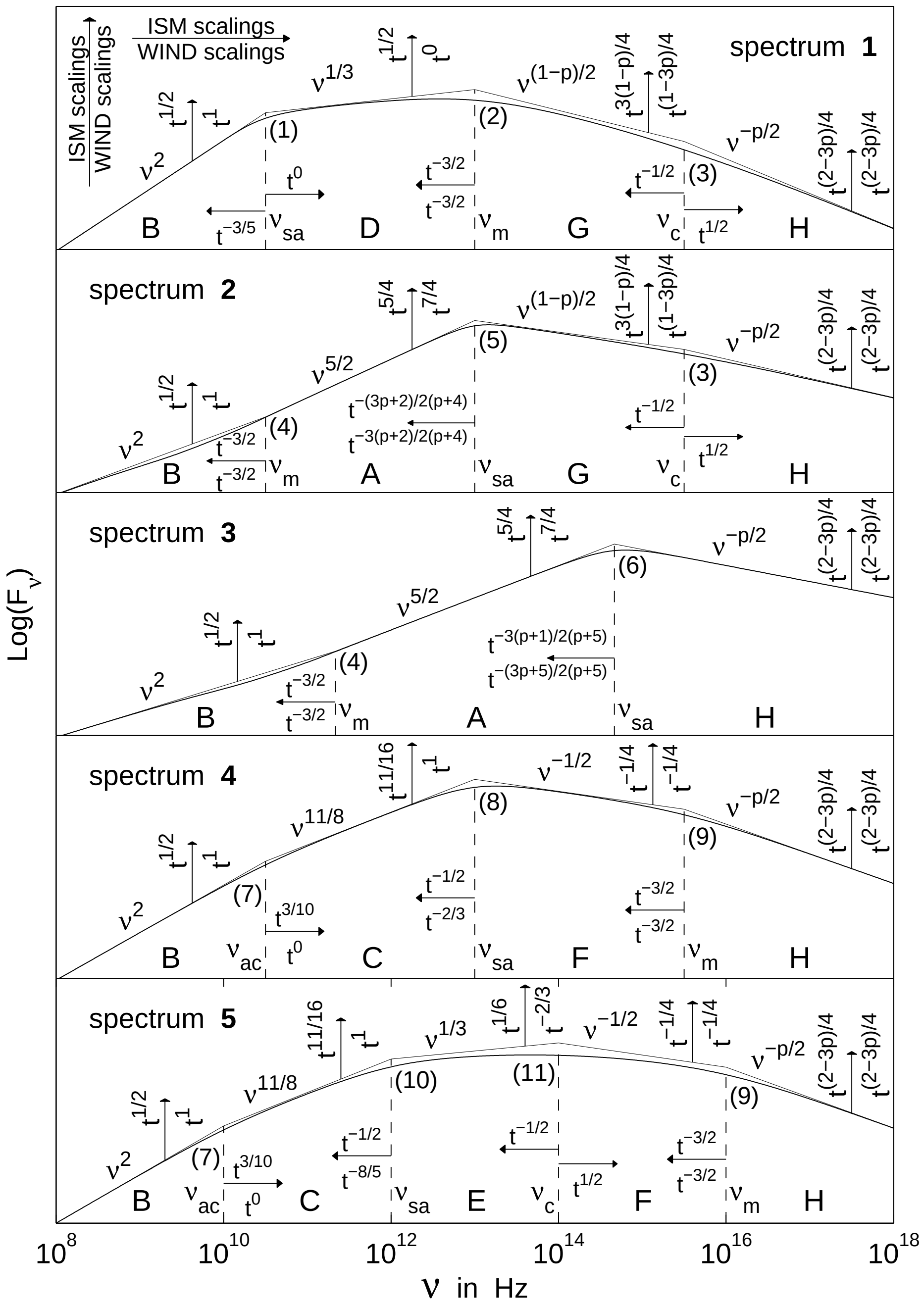

Figure 1.5: Temporal and spectral scalings of synchrotron afterglow emission (Figure 1 of Granot & Sari 2002). Spectra 1 and 2 are for slow cooling, and 4 and 5 are for fast cooling. Spectrum 3 results when ν_{sa} is greater than both ν_m and ν_c. Temporal scalings of the break frequencies and flux are specified for both ISM (constant external density) and wind ($\rho \propto r^{-2}$) external environments.

1.3 Summary

Gamma-ray bursts show a rich and varied phenomenology across a wide electromagnetic energy band, and they are expected to be sources of neutrinos and gravitational waves. Accurate localization of burst afterglows has enabled rapid improvements in our understanding of GRBs in the last decade and half. Many questions remain open, however, including the nature of the progenitors; the formation, composition, and dynamics of the outflow; and the burst emission mechanisms. Further progress will be fueled by advances in observation (multi-messenger observations, prompt polarimetry, and host galaxy statistics), simulation (3D MHD simulations of burst outflows), and theory (improved understanding of relativistic collisionless shocks).

Chapter 2

RHESSI Gamma-Ray Burst Analysis Methods

Abstract

RHESSI is a solar gamma-ray telescope. Its nine germanium detectors are unshielded and receive emission from off-axis sources like GRBs. To determine the response of RHESSI to GRBs, I performed extensive Monte Carlo simulations. I discuss these simulations, the analysis pipeline, and validation of the analysis techniques used in Chapters 3 and 4.

2.1 The RHESSI Instrument

The Reuven Ramaty High-Energy Solar Spectroscopic Imager (RHESSI; Figure 2.1) is a NASA Small Explorer satellite designed to study particle acceleration in solar flares (Lin et al. 2002). Flare spectra include thermal X-ray emission, a hard X-ray bremsstrahlung continuum, and MeV gamma-ray lines produced by ion acceleration. In order to observe these spectral components in detail, RHESSI's nine high-purity germanium detectors (Figure 2.2) provide imaging and spectroscopy of solar flares over a broad bandpass (3 keV–17 MeV) with excellent energy resolution (1–10 keV) (Smith et al. 2002).

The RHESSI signal processing chain electronically segments each cylindrical detector into thin front and thick rear segments (Figure 2.3). The front segment, which caps the coaxial rear segment, primarily detects photoabsorbed X-rays ($\lesssim$ 250 keV) from the Sun. The rear segments preferentially record higher-energy gamma-rays.

RHESSI employs a rotating modulation collimator to produce images with spatial resolution of several arcseconds (Hurford et al. 2002). Two planes of X-ray opaque grids modulate the incoming flux of on-axis sources as RHESSI rotates with a period of ~ 4 seconds. Fourier analysis of this modulation enables image reconstruction of the flares.

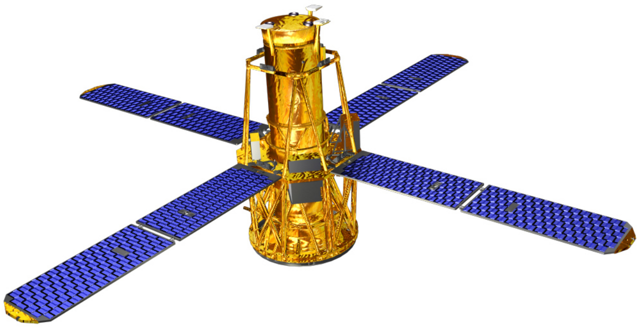

Figure 2.1: Conceptual rendition of the RHESSI spacecraft. (Image courtesy NASA/Spectrum Astro Inc.)

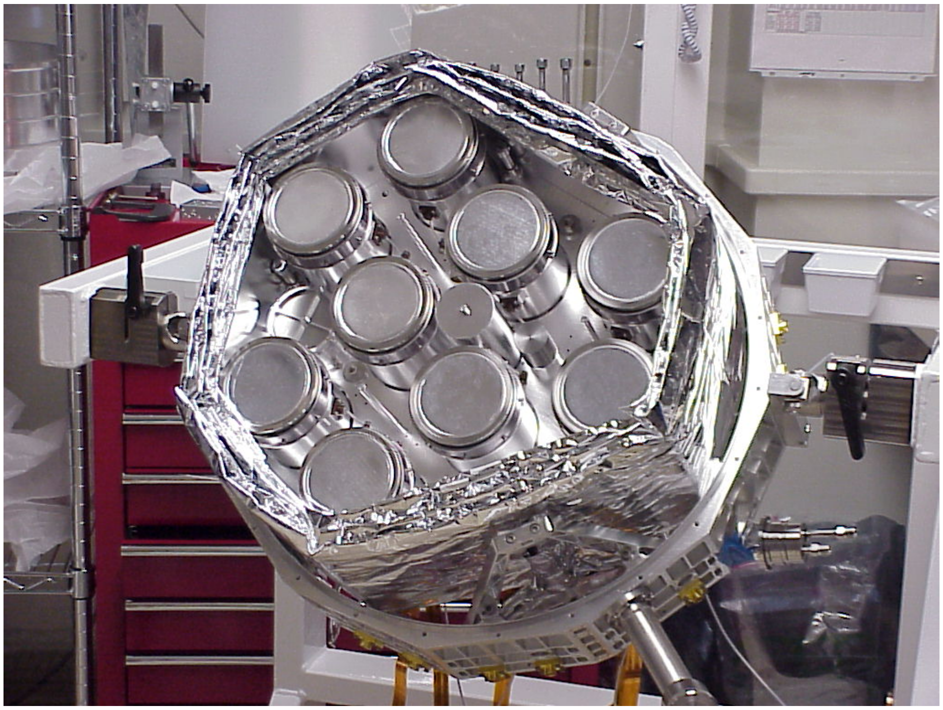

Figure 2.2: Image of the RHESSI cryostat. (Image courtesy NASA.)

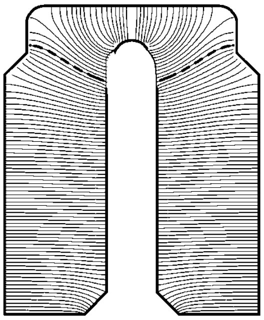

Figure 2.3: Schematic cross-section of one of RHESSI's closed-end coaxial germanium detectors (from Smith et al. 2002). Thin solid lines and bold dashed lines depict the field lines and the front-rear segmentation boundary, respectively.

The RHESSI detectors are unshielded. As a result, in addition to photons from the Sun, RHESSI may detect (but not image) off-axis astrophysical and terrestrial sources. These sources include GRBs, giant flares from Soft Gamma Repeaters (Boggs et al. 2007), Galactic nuclear gamma-ray lines (Smith 2003) and Terrestrial Gamma-Ray Flashes (Smith et al. 2005).

The onboard flight software tags each event with 1 binary μs (2^{-20} s) time resolution. The data are stored onboard before being telemetered to the Berkeley Ground Station during one of $\sim$6 daily passes.

RHESSI was launched on a Pegasus-XL launch vehicle on February 5, 2002. The instrument has performed nominally since launch. However, its 600 km circular orbit (38° inclination) includes frequent passes through the South Atlantic Anomaly (SAA). Interactions with charged particles in the SAA have caused radiation damage in the detectors: defects in the crystal lattice create hole traps, leading to a gradual degradation in active volume and spectral performance (Figure 2.4). The operations team undertook annealing procedures, in which the detectors were heated to $\sim 100°$ C for several weeks, in November 2008 and after an unexpected power loss in March 2010. Both procedures were successful in restoring some of the lost sensitivity; however, spectral analysis of GRB data from the damaged detectors will require more sophisticated modeling. The GRB analysis presented in this work employs only data from undamaged detectors (Figure 2.5).

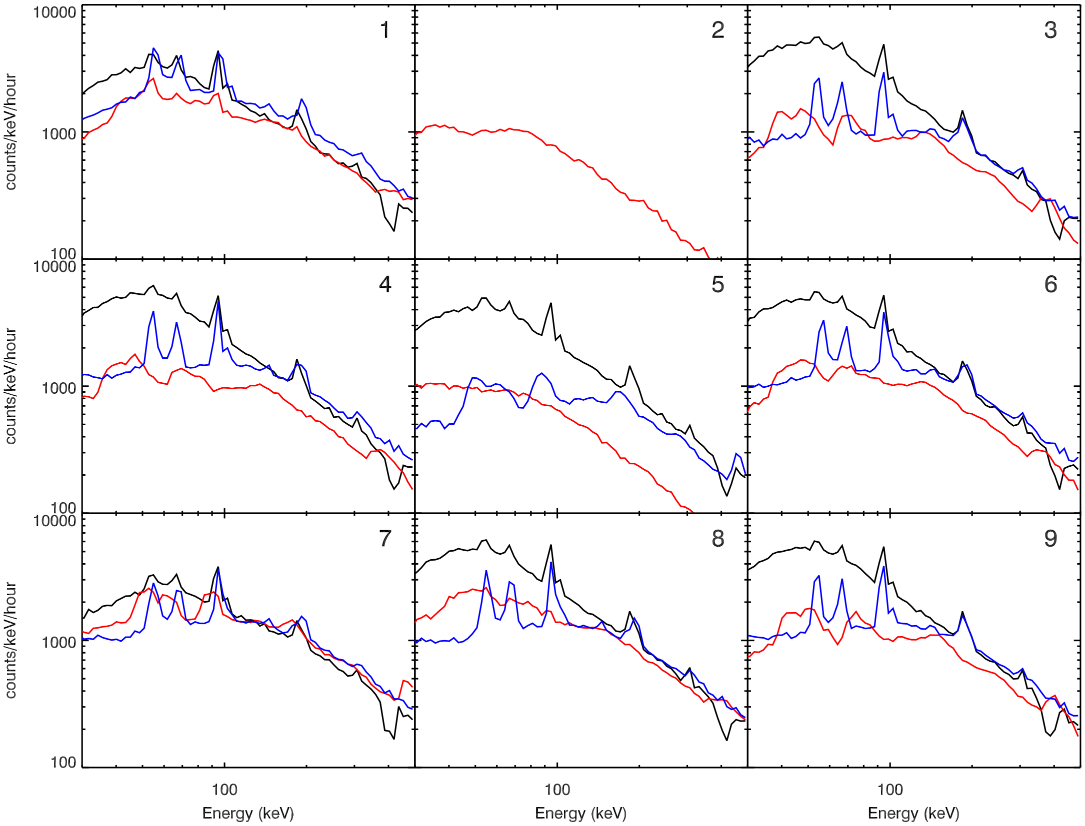

Figure 2.4: RHESSI rear segment background rates by detector at mission start (2002, black), with major radiation damage (2007, red), and after the first anneal (2008, blue). The loss of active volume and spectral resolution are readily apparent. While the annealing procedure restored some lost sensitivity, the spectral behavior still shows deviation from the initial state. (Detector 2 was only segmented during the 2007 plot interval.)

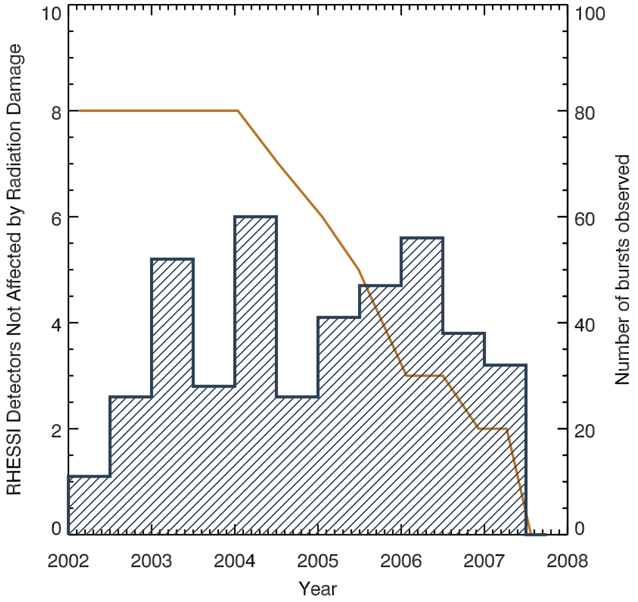

Figure 2.5: Timeline of radiation damage to the RHESSI detectors. The line shows the number of RHESSI detectors unaffected by radiation damage as a function of time. (Detector 2 is omitted in this plot because it was not segmented early in the mission.) The overplot histogram shows the number of GRBs observed by RHESSI per six-month interval.

2.2 Spectral Response

2.2.1 Photon-Detector Interactions

The source photon spectrum is extremely valuable for scientific studies of astrophysical objects. In the X-ray–gamma-ray regime, however, inference of the original spectrum is complicated by the range of interactions the source photons may have with the detector volume.

At low energies (~ 150 keV in germanium, Figure 2.6), photoelectric absorption is the dominant interaction, and the full energy of the photon is deposited. However, if fluorescence photons are excited in the detector material, these photons may escape, decreasing the observed energy. At higher energies, Compton scattering dominates. A portion of the energy of the incoming photon will be deposited through the Compton recoil electron. The scattered photon may then scatter again, be photoabsorbed, or leave the detector volume completely. In the MeV regime, electron-positron pair production becomes important. The electron or the positron may annihilate within the detector volume; the resulting annihilation photons may be photoabsorbed or escape.

Interactions with surrounding passive material may also lead to energy deposition in the detectors. A photon may Compton scatter into the detector. Similarly, one or both compo-

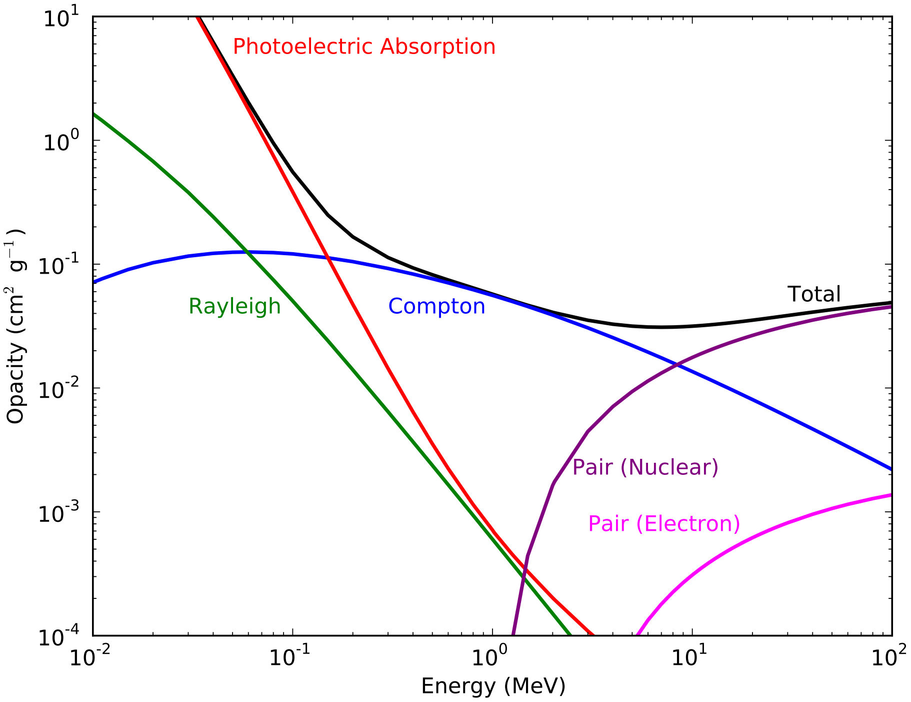

Figure 2.6: Cross section of photon interactions in germanium as a function of energy. Photoelectric absorption and Compton scattering are the most important processes for GRB spectroscopy.

nents of a pair produced outside the detector may annihilate within it. Finally, fluorescence photons excited in passive material may be absorbed in the detectors.

Accordingly, the energy of an incoming photon generally cannot be derived from the energy of the count observed by the detector. Instead, knowledge of the spectral response of the detector can be used with an observed count spectrum to make probabilistic inferences about the source photon spectrum.

2.2.2 Monte Carlo Response Generation

In order to determine RHESSI's response to incoming photons, I utilized Monte Carlo simulations with a detailed model of the RHESSI spacecraft. The RHESSI science team developed this mass model (Figure 2.7) with reference to the engineering drawings (Smith 2005). The model simplifies non-critical sections of the satellite body while preserving detail in the detectors and cryostat (Figure 2.8).

I used the GEANT3-based Monte Carlo suite MGEANT (Sturner et al. 2000) to simulate the RHESSI response. Because the spacecraft rotates along its axis, I simulated photons along 60° arcs in rotation angle (Figure 2.9). Trial simulations showed that the response does not vary appreciably on smaller scales. I simulated six sector responses for each off-axis

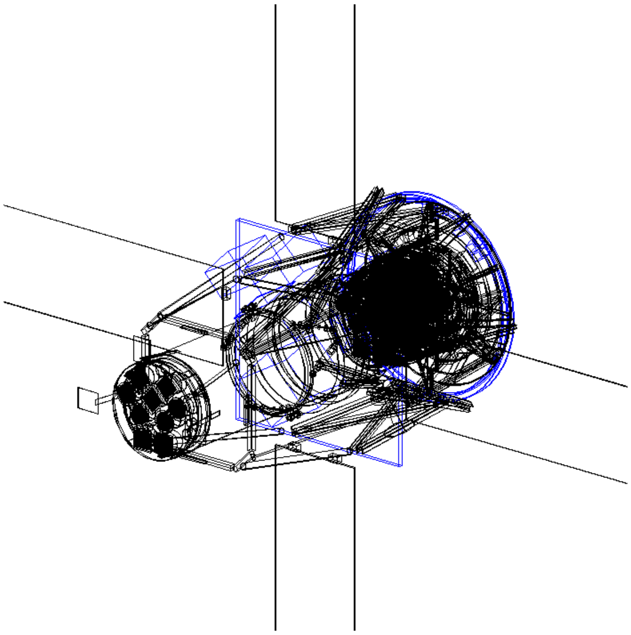

Figure 2.7: Image of the RHESSI mass model used for the Monte Carlo simulations presented in this work.

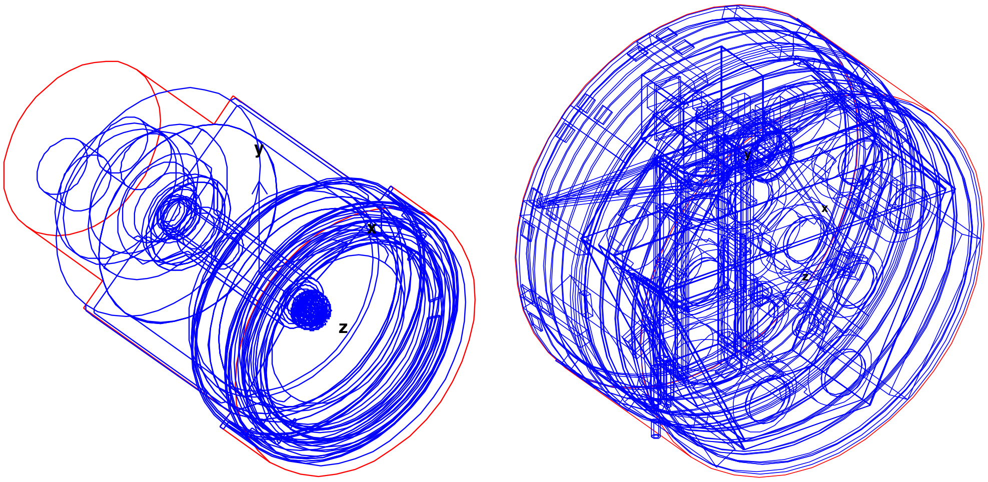

Figure 2.8: Detail view of a detector module and the cryostat assembly in the RHESSI mass model.

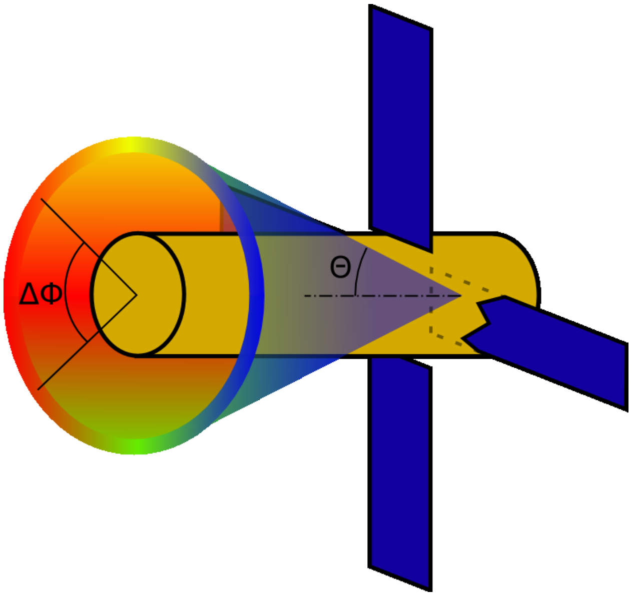

Figure 2.9: Simulation geometry for RHESSI response. For each off-axis angle θ, I simulated photons impinging from azimuthal sectors $\Delta\phi$.

angle. Off-axis angles were spaced every 15° from 0° (on axis) to 180° (incidence on the spacecraft rear). The detector response changes smoothly and slowly (Figure 2.11) between the tabulated responses, and the analysis chain interpolates between adjacent responses to determine the value at the true GRB angle.

For each off-axis angle and sector, I simulated monoenergetic photons from 30 keV to 30 MeV. I chose an energy binning scheme to maximize flexibility and ease of rebinning. The bin scheme must balance the need for many spectral bins to best constraint the fit parameters with the requirement that each bin must have enough counts to be in the Gaussian regime ($N \gtrsim 10$) (Section 2.2.3). Because GRBs vary significantly in spectrum and intensity, energy bands effective for one burst may be poor for another. By examining the RHESSI-observed count spectra for a range of GRBs, I found a scheme which allowed detailed coverage of the brightest GRBs while degrading gracefully for dimmer ones. Table 2.1 describes the binning. Since the number of bins in each segment is a power of two, it is straightforward to halve or quarter the number of bins in order to deal with low-count spectra.

Figure 2.10 shows the simulated response matrix for the rear segments for photons incident at 120° from the rotation axis. A major portion of the response is off-diagonal, indicating that for many interactions the full energy of the incoming photon is not recorded in any single segment.

Effective area (A_{eff}) is the conventional means for specifying the efficiency of high-energy astrophysical telescopes. If a number of counts $C(E)$ of energy E is detected from a known

E_{min} (keV)	E_{max} (keV)	N_{bins}
30	60	16
60	515	64
515	3000	32
3000	17000	8
17000	30000	4

Table 2.1: Number of logarithmic bins per energy band used in the RHESSI response simulations.

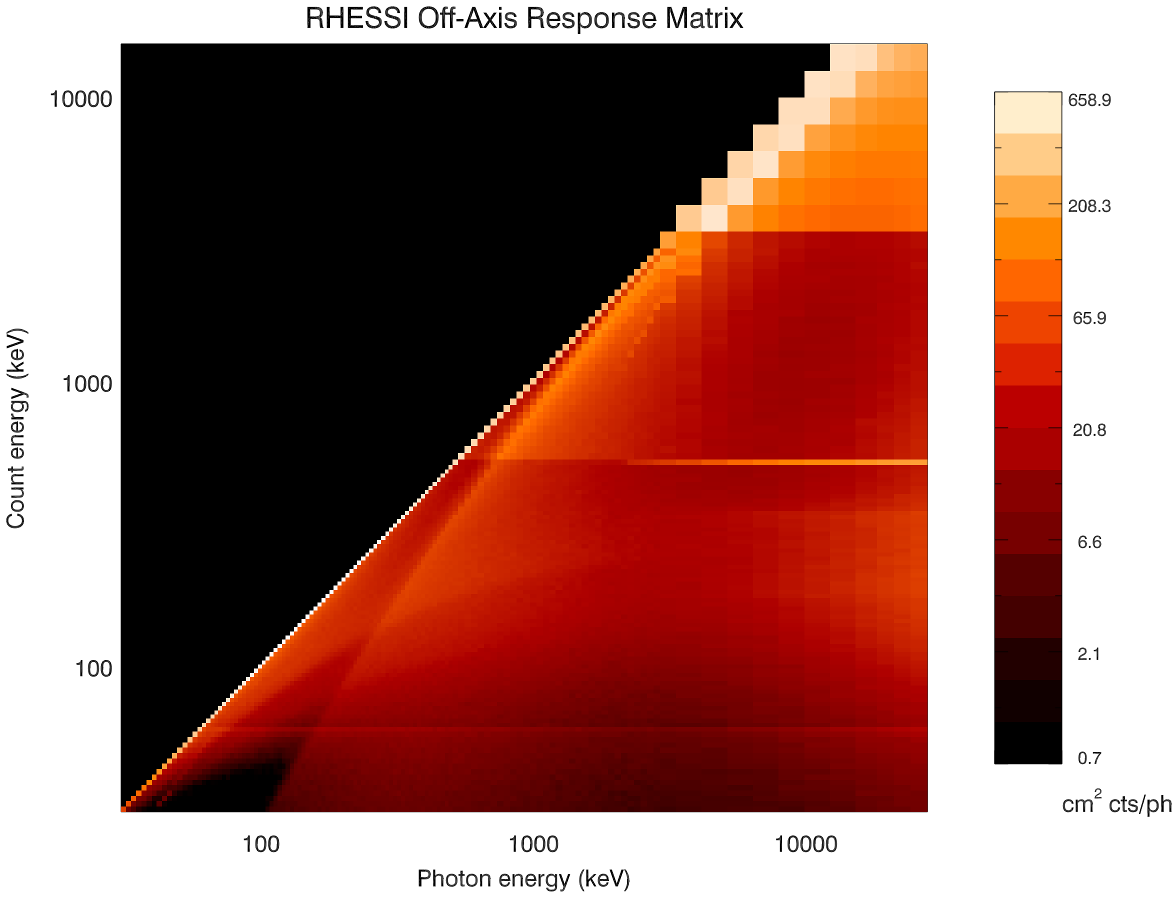

Figure 2.10: Simulated RHESSI rear-segment response matrix for 120° incidence. The photopeak, Compton edge, and positron annihilation features can be seen.

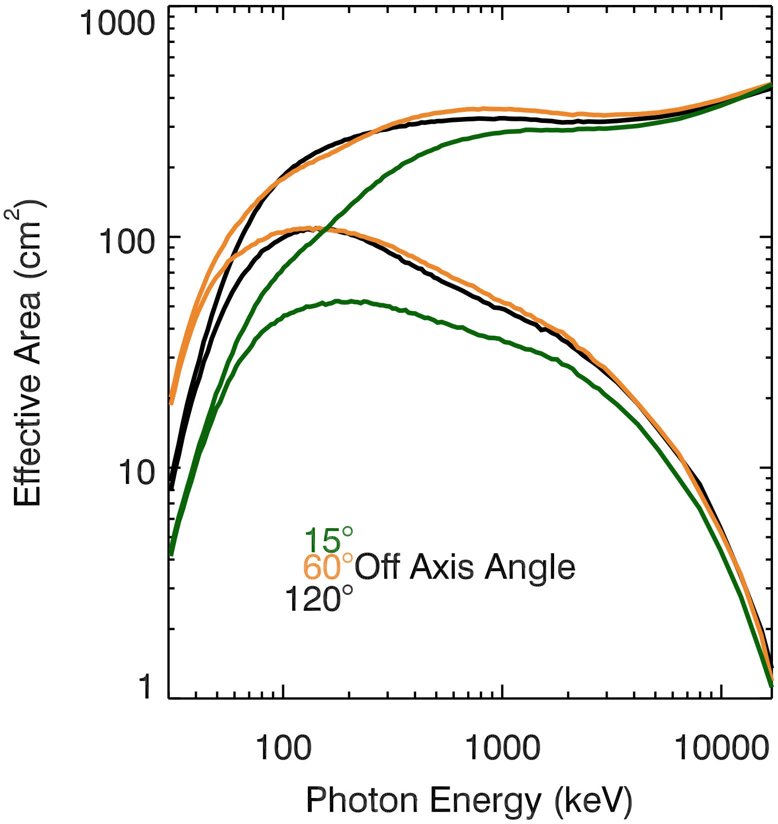

Figure 2.11: Simulated RHESSI effective area for 15°, 60°, and 120° incidence. The plot includes the effective area for photopeak-only events (lower curves) and for any event having one or more interactions in any detector (upper curves).

flux $F(E_\gamma)$ of monoenergetic photons of energy E_γ in time T_{obs}, the effective area is given by

$$A_{\text{eff}}(E, E_\gamma) = \frac{C(E)}{F(E_\gamma)T_{obs}}. \tag{2.1}$$

The units of A_{eff} are cm^2 counts/photon.

Figure 2.11 shows RHESSI's effective area for several off-axis angles. For analysis of spectral lines, the number of photopeak events ($E = E_\gamma$) observed is vital. For continuum sources like GRBs, however, photons which deposit only some of their energy ($E < E_\gamma$) are still useful.

2.2.3 Spectral Fitting

Because the RHESSI response is strongly off-diagonal, it is not possible to infer the source photon spectrum directly from the observed count spectrum. The instrument response function relates these quantities:

$$C(E) = T_{obs} \int N_E(E_\gamma) A_{\text{eff}}(E, E_\gamma) dE_\gamma \tag{2.2}$$

where $N_E(E_\gamma)$ is the differential photon flux (photons cm^{-2} s^{-1} keV^{-1}).

The inversion of this integral equation for $N_E(E_\gamma)$ from the measured $C(E)$ is unreliable in practice. Instead, a "forward fitting" approach has typically been employed in high-energy astrophysics. Given a model spectrum $N_{E,mod}(E_\gamma, p)$ which depends on parameters p, one may produce the expected count spectrum in the instrument given the spectral model by

$$M(E_i, p) = T_{obs} \sum_j N_{E,mod}(E_j, p) A_{\text{eff}}(E_i, E_j) \Delta E_j. \tag{2.3}$$

A nonlinear least-squares fitting algorithm varies the parameters p and uses the modeled and observed count spectra to construct a test statistic. The "best fit" parameters p minimize the chosen fit statistic. Typically, the fit statistic used is the χ^2 statistic, which has the advantage of also providing a goodness-of-fit estimate. Appropriate use of the χ^2 statistic requires that the variance of the observed counts $C(E_i)$ be $\sigma_i \simeq \sqrt{C(E_i)}$. Since the variance of Poisson-distributed data approaches the Gaussian variance for large numbers, this determines the requirement that each $C(E_i) \gtrsim 10$.[1]

Since it is necessary to assume a spectral shape in order to fit the data, the utility of forward fitting is limited by the reasonableness of the spectral models considered. Model choices may become conventional without being physical. However, in cases where there is good theoretical justification for specific spectral models, forward fitting provides a computationally efficient means of analyzing X-ray and gamma-ray spectra.

2.3 Data Analysis Pipeline

The RHESSI data analysis software[2] is written in the SSW-IDL analysis environment[3], a collection of solar physics libraries built on the IDL software package. To facilitate calls to the data extraction and spacecraft aspect routines, I wrote the data pipeline software used for analyzing RHESSI GRB data in IDL as well.

---

[1] Alternative approaches for low-count fitting have included weighting by model variances rather than data variances (Ford et al. 1995) and using small-count error bars derived from the Poisson distribution (Gehrels 1986). Recent work suggests that replacing χ^2 fitting with alternate statistics (Cash 1979) may be necessary for bias-free fitting even in the high-count regime (Humphrey et al. 2009).

[2] `http://hesperia.gsfc.nasa.gov/rhessidatacenter/software.html`

[3] `http://www.lmsal.com/solarsoft/`

The first step in analyzing RHESSI GRB spectra is to obtain localization information from other satellites. Because RHESSI cannot image off-axis sources like GRBs, it is necessary to obtain the coordinates of the burst from *Swift*, the Interplanetary Network[4], or other observatories in order to determine the angle of the burst relative to RHESSI's rotation axis. Since RHESSI's response varies considerably with off-axis angle (Figure 2.11), spectral analysis is not reliable without a localization accuracy of several degrees or better.

The burst angle and the time of the burst determine the detector segments employed in subsequent analysis. For bursts with off-axis angles of 75° or less, the front segments record appreciable counts. I use the rear segments alone for bursts with larger off-axis angles, as at these angles the front segment data is mainly background. Despite efforts to model the degradation of the RHESSI detectors due to radiation damage, the effect of the damage on observed continuum spectra remains uncertain. Accordingly, I omit from analysis all detectors damaged at the time of the burst (Figure 2.5).

Semi-automated software tools aid in the identification of background and source time intervals, but the final determination is user-driven. In some cases, matching data from other instruments requires exact time intervals. Because RHESSI has relatively high background, the period in which it detects GRB emission is often shorter than that of other observatories. For cases in which the times for spectral extraction need to be specified, the software provides cues as to the significance of the burst detection.

In its default configuration, the analysis pipeline extracts a six-minute light curve over the full 30 keV–17 MeV energy band with one-second time resolution. The software initially suggests background intervals before and after the burst where the median-subtracted bin significance is less than 3σ throughout. The user tunes these suggestions to specify final background intervals.

The software fits a third-order polynomial to the observed background in three energy bands, 30–150 keV, 150–400 keV, and 400 keV–17 MeV. These fits specify a background model as a function of time and are used to produce background spectra scaled to the burst interval.

Individual detectors may show periodic modulation with the spin period, particularly below 150 keV (Figure 2.12). Accordingly, the background fitting routine uses the RHESSI aspect system to extract a lightcurve with time bins matching the edges of the six azimuthal RHESSI response sectors (Section 2.2.2). By summing the light curve for each sector, the fitting software produces an azimuthal amplitude $A(\mathrm{seg}_i, \Delta E_j, \mathrm{az}_k)$ for each segment seg_i, energy band ΔE_j, and azimuthal sector az_k. Subtracting the mean

$$\langle A(\mathrm{seg}_i, \Delta E_j)\rangle = \frac{1}{N_{\mathrm{az}}} \sum_{k=1}^{N_{\mathrm{az}}} A(\mathrm{seg}_i, \Delta E_j, \mathrm{az}_k) \tag{2.4}$$

produces a modulation

$$\Delta A(\mathrm{seg}_i, \Delta E_j, \mathrm{az}_k) = A(\mathrm{seg}_i, \Delta E_j, \mathrm{az}_k) - \langle A(\mathrm{seg}_i, \Delta E_j)\rangle. \tag{2.5}$$

---

[4] `http://www.ssl.berkeley.edu/ipn3/`

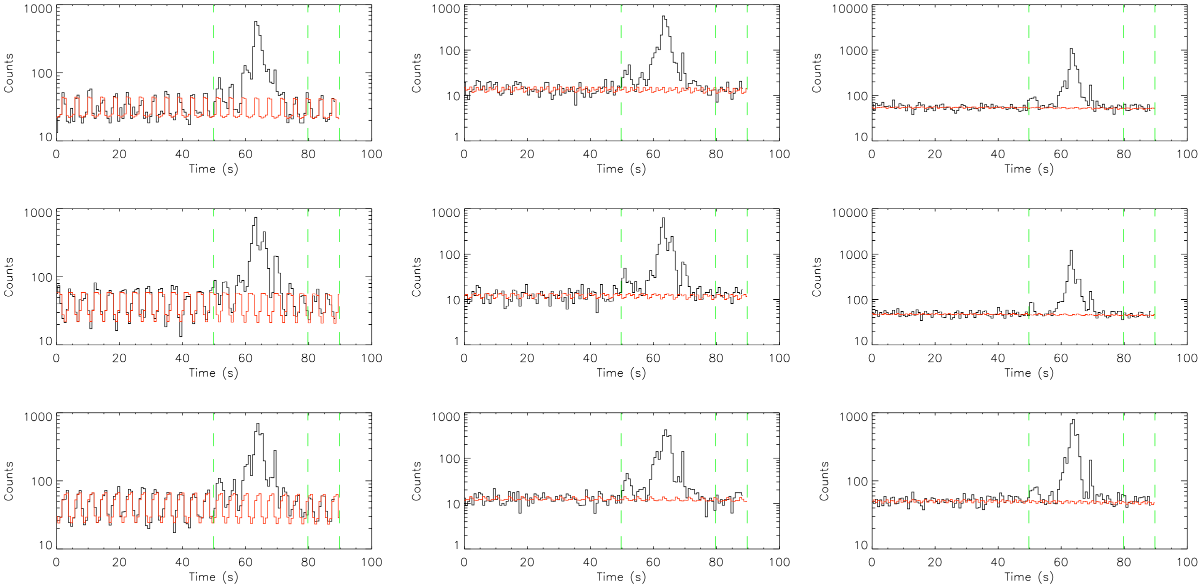

Figure 2.12: Azimuthally-modulated background fit to data for GRB021008 showing an extreme case of modulation. Each row shows data from one rear segment. Plot energies are 30–150 keV, 150–400 keV, and 400 keV–17 MeV.

The modulation, which is allowed to grow or decay linearly in time, modifies the polynomial fit. The background fit function is accordingly

$$BG(\mathrm{seg}_i, \Delta E_j, t_k) = (\langle A(\mathrm{seg}_i, \Delta E_j)\rangle - \Delta A(\mathrm{seg}_i, \Delta E_j, \mathrm{az}_k)(1+Yt_k))(A+Bt_k+Ct_k^2+Dt_k^3+\ldots) \tag{2.6}$$

with fit parameters $Y, A, B, C, D, \ldots$. Not all burst background intervals display this modulation, so the user chooses between the modulated background and a simple polynomial fit. Finally, the software extracts the burst spectrum and subtracts the modeled background.

To generate the detector response function, the software interpolates between the Monte Carlo response matrices for the two off-axis angles nearest the true GRB angle on the 15° grid. As RHESSI rotates, those detectors which are nearest to the burst will preferentially record the most counts. Because GRBs have irregular temporal structure, RHESSI's rotation introduces a bias: detectors facing the GRB during bright portions of the burst will produce more data than those oriented toward the burst's dim periods (Figure 2.14). To account for this effect, the software gives the user the option to "lightcurve-weight" the response matrix. In this procedure, the azimuthal sector responses are averaged with weights given by the proportion of total burst counts occurring in that sector of rotation angle. This method also provides a convenient means of producing responses for intervals less than a complete rotation period.

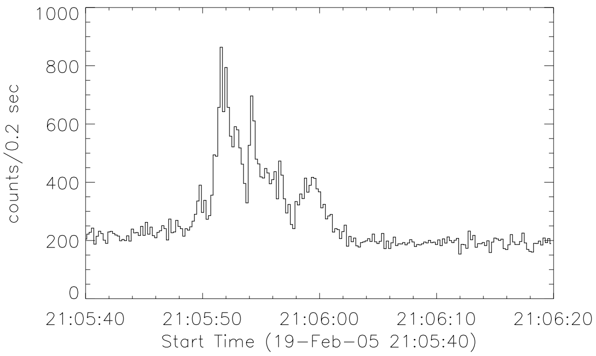

Figure 2.13: RHESSI lightcurve of GRB 050219B (50 keV–200 keV) using data from all rear segments. Because of the irregular temporal structure of the burst, detectors oriented toward the burst during bright intervals will record more counts than those rotated away (Figure 2.14).

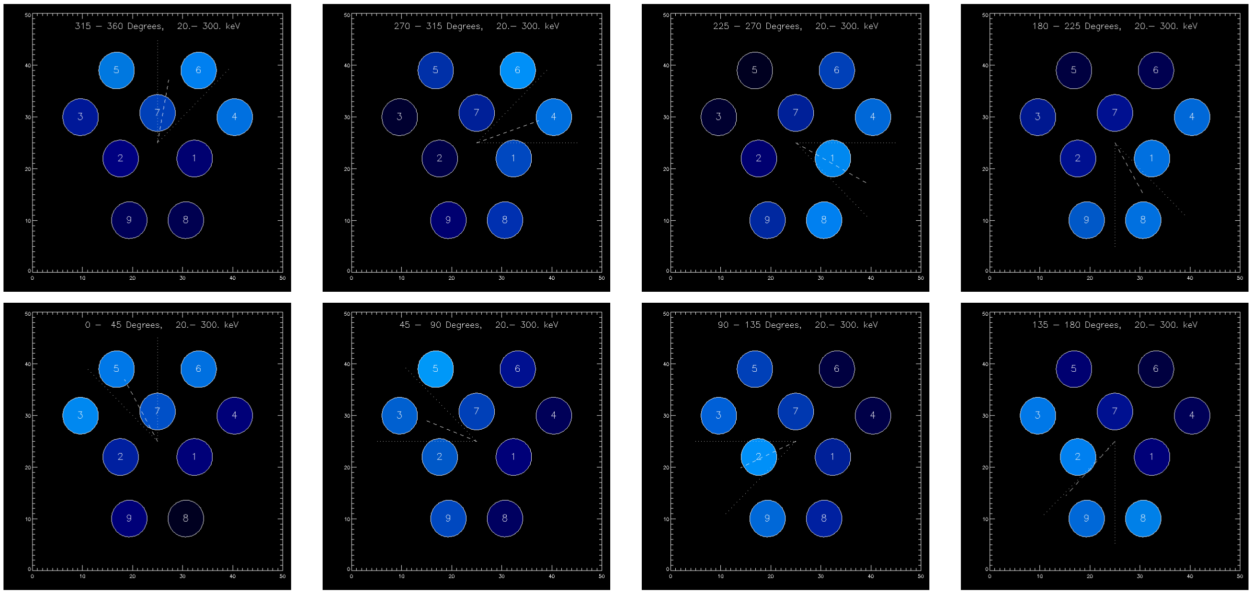

Figure 2.14: Detector distribution of observed counts (50 keV–200 keV) with rotation. The images show (in counter-clockwise order) the counts observed per detector for GRB 050219B (Figure 2.13) in consecutive eighths of a rotation period. As RHESSI rotates, the detectors oriented towards the burst record more counts. This effect is most pronounced for bursts such as this one which are perpendicular to the RHESSI rotation axis. Images from Bandstra (2006).

The final RHESSI spectrum and response are written to disk as OGIP PHA[5] and RMF[6] files. These standard formats allow RHESSI data to be analyzed jointly with that of other instruments in a straightforward manner. The analysis parameters—time intervals, energy bands, detector segments, etc.—are stored in a MySQL database for later use.

Spectral fitting of the RHESSI data may occur in the forward-fitting packages XSPEC[7] or ISIS (Houck & Denicola 2000). ISIS is preferentially used in this work as it is easier to script and allows for rigorous error estimates on the burst fluence via exploration of the parameter space.

2.4 Verification

In order to verify the accuracy of the response matrices and the analysis methods, I conducted test fits of simulated spectra, compared my results for real RHESSI GRBs to those obtained using different simulations and fit methods, and looked for correspondence with GRBs observed by other instruments.

During the development of these analysis methods, I fit simulated spectra produced using the same mass model. In Figure 2.15, I present an example fit which uses the spectral parameters of a bright BATSE burst (Kaneko et al. 2006) at a random incidence angle.

A different approach to analyzing RHESSI GRB spectra is described in Wigger et al. (2008). These authors employ the same mass model described in Section 2.2.2. They simulate a source photon spectrum of $N_E \propto E^{-2}$, then use a spectral model to weight the resulting count spectrum until it matches the observed count spectrum. The different fit methods produce good correspondence in the fit parameters (e.g., Table 4.2). I collaborated closely with these authors while developing the methods presented here. Our reports[8] of RHESSI spectral fits to the Gamma-Ray Burst Coordinates Network (GCN)[9] allowed detailed comparison of the results of the different fit approaches for individual bursts.

Simultaneous observation of individual RHESSI GRBs by other instruments has enabled comparison of fit results and joint fits. (Differences in energy band, integration period, and fit model complicate these comparisons, however.) Figure 2.16 compares the RHESSI preliminary $E_{\rm peak}$ value reported via the GCN to those reported by other instruments.

For GRB 070125, I conducted joint fits between RHESSI and *Konus*-WIND data to test luminosity relations for one of the most energetic GRBs ever observed (Bellm et al. 2008b). Due to radiation damage to the RHESSI detectors, the *Konus* data had about six times more usable counts, allowing for better statistical constraint of the burst spectrum. The RHESSI data tended to fit higher $E_{\rm peak}$ values for this burst, although the fit values were consistent

---

[5] `http://heasarc.gsfc.nasa.gov/docs/heasarc/ofwg/docs/spectra/ogip_92_007/ogip_92_007.html`

[6] `http://heasarc.gsfc.nasa.gov/docs/heasarc/caldb/docs/memos/cal_gen_92_002/cal_gen_92_002.html`

[7] `http://heasarc.gsfc.nasa.gov/docs/xanadu/xspec/`

[8] GCN Circulars 8857, 8251, 6399, 6135, 6025, 5867, 5838, 5725, 5685, 5684, and 5418

[9] `http://gcn.gsfc.nasa.gov/`

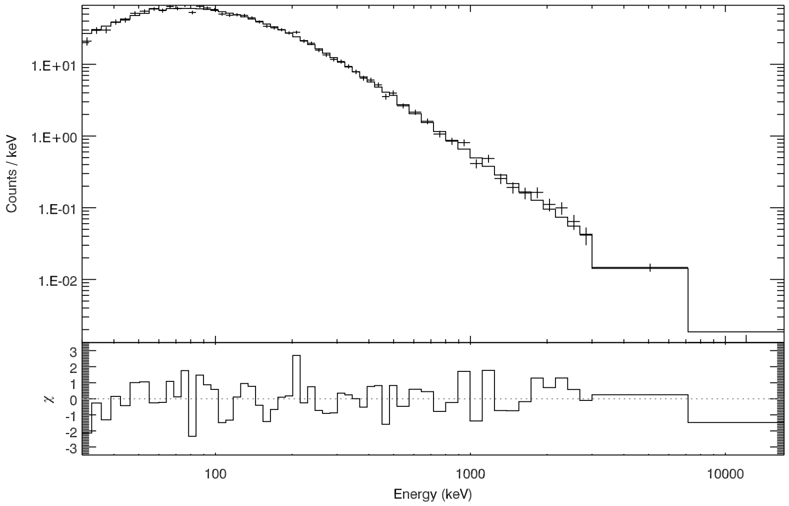

Figure 2.15: Spectral fit of a simulated GRB using the analysis methods presented here. The Band function fit values of $\alpha = -0.72^{+0.12}_{-0.11}$, $E_{\rm peak} = 433^{+42}_{-39}$, $\beta = -2.45^{+0.066}_{-0.077}$ are identical within error to the input parameters $\alpha = -0.73$, $E_{\rm peak} = 421$, $\beta = -2.38$. The fit was acceptable, with $\chi^2/{\rm dof} = 61.8/58 = 1.14$. The simulated off-axis angle was 52.6 degrees.

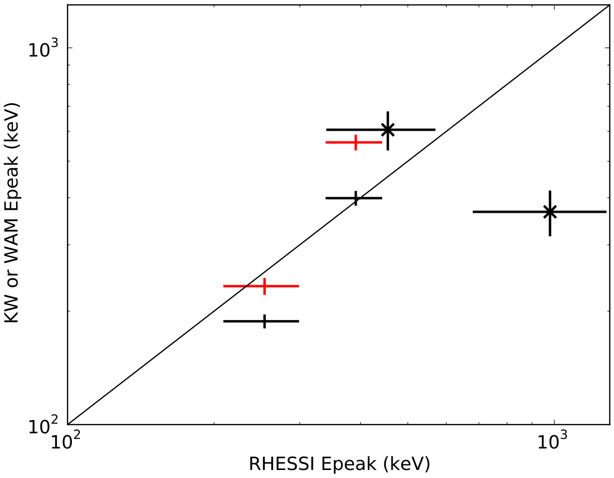

Figure 2.16: Comparison of RHESSI $E_{\rm peak}$ values reported in the GCN to those of *Konus*-WIND (black) and *Suzaku*-WAM (red). Data are for bursts (L-R) 070508, 061007, 061121, and 070125. For points marked with a cross, the $E_{\rm peak}$ values are derived from different models, introducing a bias in the directions observed: the $E_{\rm peak}$ value obtained by Band function fits are systematically lower than those given by cutoff power-law fits (Band et al. 1993).

with those of *Konus* due to large error bars. Joint fitting required a normalization offset between RHESSI and *Konus* of 0.85–0.95. (A systematic study of GRB data from *Konus*, BAT, and WAM found a characteristic *Konus* offset of a similar magnitude (Sakamoto et al. 2010).) My joint spectral analysis of RHESSI, *Konus*-WIND, and *Suzaku*-WAM data for the short burst GRB 051103 helped explore whether some observed short GRBs could be giant flares from extragalactic Soft Gamma-Ray Repeaters (Hurley et al. 2010). The spectral agreement between the RHESSI and *Konus* data for this burst was better and the required normalization offset smaller.

The joint RHESSI+BAT fits presented in Chapter 3 did not require a normalization offset between the two instruments, and the fit results showed excellent agreement with independent *Konus* and *Suzaku*+BAT fits (Table 3.2, Figure 3.1).

2.5 Summary

The unshielded germanium detectors of RHESSI make it a capable GRB detector with a wide field of view, broad energy band, excellent time and energy resolution, and moderate effective area. Using localizations obtained by other instruments, it is possible to determine RHESSI's spectral response with detailed Monte Carlo simulations. The analysis methods account for background modulation and response shifts due to RHESSI's four second rotation period. Spectral fitting results of RHESSI GRBs show good correspondence with results obtained by other instruments.

Chapter 3

RHESSI Spectral Fits of *Swift* GRBs

Abstract

One of the challenges of the *Swift* era has been accurately determining the spectral peak E_{peak} of the prompt GRB emission. RHESSI, which is sensitive from 30 keV to 17 MeV, can extend spectral coverage above the *Swift*-BAT bandpass. Using the public *Swift* data, I present results of joint spectral fits for 26 bursts co-observed by RHESSI and *Swift*-BAT through May 2007. I compare these fits to estimates of E_{peak} which rely on BAT data alone. A Bayesian E_{peak} estimator gives better correspondence with the measured results than estimators relying on correlations with the *Swift* power law indices.

Portions of this work are taken from Bellm et al. (2008a) and are used here with permission.

3.1 The GRB Spectral Peak $\mathrm{E}_{\mathrm{peak}}$

Gamma-ray burst prompt spectra show a characteristic νF_ν spectral peak E_{peak} with energies ranging from tens of keV to several MeV. The peak energy is correlated with the intensity of the emission (the hardness-intensity correlation) and tends to evolve to lower energies in time (Ford et al. 1995). For spectral fits using the empirical Band function (Band et al. 1993), $E_{\mathrm{peak}} = (2 + \alpha)E_0$ so long as the high-energy power-law index $\beta < -2$. For a few bursts EGRET (González et al. 2003; Kaneko et al. 2008) and *Fermi* (Abdo et al. 2009a) observed rising high-energy power-law components suggesting a second, yet-unmeasured GeV spectral peak. However, a smooth spectral rise to and fall from the MeV E_{peak} is observed in available data for most bursts. Accordingly, accurate measurement of E_{peak} is needed to understand the energy released in the GRB prompt phase.

The launch of the *Swift* satellite opened a new era in the studies of GRBs, with its rapid slewing and localization capability enabling systematic observations of GRB afterglows (Gehrels et al. 2009). However, the narrow bandpass of *Swift's* Burst Alert Telescope (BAT;

15–150 keV) prevented the detection of the spectral peak of many bursts and hence their overall energetics. This shortcoming was particularly troubling due to interest in proposed luminosity relations connecting E_{peak} to the total energy release (Amati et al. 2002; Ghirlanda et al. 2004). Accordingly, supplemental observations from other observatories like RHESSI, *Konus*-WIND, and *Suzaku*-WAM were needed to complete the *Swift* GRB observations.

3.2 RHESSI-BAT Joint Fits

I attempted simultaneous spectral fitting for all RHESSI-observed GRBs appearing in the first BAT Catalog (Sakamoto et al. 2008). In this work, I restricted the analysis to those detectors which do not exhibit signs of radiation damage. At the time of *Swift*'s launch, six RHESSI segments were usable for spectroscopy; by May 2007 only two segments remained undamaged. Of 46 candidate bursts, 26 had sufficient RHESSI counts for spectral analysis and produced acceptable joint fits. I selected analysis time intervals manually from the RHESSI lightcurve using a S/N criterion. The resulting intervals were usually shorter than those used in the BAT Catalog. I extracted the RHESSI data using the methods described in Chapter 2. I generated BAT spectra and responses for these intervals with the standard analysis procedures.[1]

Typically, the joint fits did not require a normalization offset between the RHESSI and BAT data. (Of the four bursts that needed an offset for acceptable fitting, one was in a period of highly modulated RHESSI background, and three were after December 2006 when radiation damage was becoming severe.) For the RHESSI data, I generally fit over the full 30 keV-17 MeV energy band. For bursts coming from the rear of RHESSI, I raised the lower energy bound to ~60 keV, as the additional passive material of the RHESSI cryostat can influence the low energy data. For GRB 061007, I omitted the RHESSI data above 3 MeV; there were no significant counts above that level, but the residuals showed systematic deviation which biased the fit.

For 16 of the 26 bursts, the joint RHESSI-BAT best fit found additional model parameters (E_{peak} and/or β) compared to the BAT-only fit. I report the results of the joint fits in Table 3.1.

These results correspond well with comparable fits reported by *Konus*-WIND and *Suzaku*-WAM, which also are sensitive in the MeV range. The fit parameters reported for co-observed bursts in Table 3.2 are consistent within errors in general. Figure 3.1 compares the E_{peak} values obtained with the RHESSI+BAT joint fits presented here to the WAM+BAT fits of Krimm et al. (2009). There is excellent agreement between the fit E_{peak} values over a large energy band.

---

[1] http://swift.gsfc.nasa.gov/docs/swift/analysis/threads/bat_threads.html

GRB	Analysis Interval (sec)	Best Fit Model	α	$E_{\rm peak}$ (keV)	β	Fluence (10^{-6} ergs/cm^2)	χ^2_ν
041223	0.0 – 124.0	CPL	$-0.97^{+0.05}_{-0.04}$	$617.^{+86.}_{-70.}$		$87.8^{+8.1}_{-7.1}$	1.21
041224	-3.7 – 36.3	Band	$-0.77^{+0.60}_{-0.32}$	$77.^{+20.}_{-19.}$	$-2.10^{+0.16}_{-0.24}$	$12.9^{+3.8}_{-3.2}$	0.93
050124	-2.2 – 3.8	Band	$-0.65^{+0.72}_{-0.45}$	$86.^{+40.}_{-24.}$	$-2.12^{+0.20}_{-0.50}$	$3.3^{+1.3}_{-1.2}$	0.81
050219B	-29.3 – 10.7	Band	$-1.10^{+0.12}_{-0.10}$	$188.^{+27.}_{-26.}$	$-2.62^{+0.29}_{-0.84}$	$37.1^{+5.1}_{-4.7}$	0.99
050326	-1.1 – 24.9	Band	$-1.01^{+0.13}_{-0.11}$	$277.^{+181.}_{-77.}$	$-1.73^{+0.12}_{-0.19}$	$61.7^{+19.1}_{-16.0}$	0.72
050525A	0.1 – 12.9	Band	$-1.02^{+0.11}_{-0.10}$	$81.^{+3.}_{-3.}$	$-3.12^{+0.25}_{-0.50}$	$21.3^{+1.2}_{-1.1}$	0.90
050713B	-1.6 – 27.4	PL	$-1.40^{+0.04}_{-0.04}$			$43.0^{+4.8}_{-4.7}$	1.03
050717	-0.2 – 35.8	CPL	$-1.13^{+0.04}_{-0.04}$	$2237.^{+483.}_{-386.}$		$65.7^{+7.2}_{-6.9}$	0.92
050802	-3.3 – 22.7	PL	$-1.65^{+0.06}_{-0.07}$			$15.8^{+3.6}_{-3.2}$	1.02
050820B	6.8 – 12.8	CPL	$-0.57^{+0.17}_{-0.16}$	$147.^{+25.}_{-18.}$		$2.6^{+0.3}_{-0.3}$	0.96
051111	-14.5 – 11.5	Band	$-1.04^{+0.19}_{-0.14}$	$255.^{+156.}_{-84.}$	$-1.98^{+0.17}_{-0.46}$	$20.0^{+4.3}_{-4.6}$	0.89
051221A	0.2 – 2.3	Band	$-1.26^{+0.17}_{-0.13}$	$238.^{+175.}_{-81.}$	$-1.98^{+0.11}_{-0.21}$	$4.8^{+0.8}_{-0.8}$	1.35
060110	-0.8 – 11.2	PL	$-1.60^{+0.05}_{-0.05}$			$9.7^{+1.8}_{-1.6}$	0.90
060117	-0.6 – 17.4	CPL	$-1.58^{+0.10}_{-0.09}$	$77.^{+6.}_{-6.}$		$26.8^{+1.4}_{-1.2}$	1.06
060418	-5.2 – 30.8	CPL	$-1.52^{+0.07}_{-0.07}$	$624.^{+671.}_{-240.}$		$22.4^{+7.7}_{-4.4}$	0.92
060421A	-0.3 – 3.7	Band	$-0.88^{+0.33}_{-0.26}$	$141.^{+106.}_{-42.}$	$-1.87^{+0.20}_{-0.63}$	$3.6^{+2.1}_{-1.9}$	0.82
060501	-2.9 – 10.1	PL	$-1.37^{+0.05}_{-0.06}$			$21.9^{+4.5}_{-4.2}$	1.04
060502A	-15.1 – 9.9	Band	$-0.87^{+0.35}_{-0.24}$	$172.^{+144.}_{-60.}$	$-1.98^{+0.26}_{-1.67}$	$11.8^{+7.0}_{-5.9}$	1.04
060614	-1.5 – 3.5	CPL	$-1.56^{+0.12}_{-0.11}$	$280.^{+279.}_{-97.}$		$6.7^{+6.7}_{-1.2}$	0.95
060908	-3.3 – 1.7	CPL	$-0.68^{+0.23}_{-0.20}$	$161.^{+49.}_{-32.}$		$2.0^{+0.4}_{-0.3}$	0.87
061007	-0.8 – 63.2	Band	$-0.85^{+0.04}_{-0.04}$	$478.^{+52.}_{-51.}$	$-2.47^{+0.24}_{-0.42}$	$244.6^{+23.2}_{-22.5}$	0.84
061121	56.0 – 85.0	Band	$-1.31^{+0.04}_{-0.04}$	$741.^{+214.}_{-169.}$	$-2.37^{+0.32}_{-1.21}$	$64.7^{+8.1}_{-8.4}$	1.02
061126	-4.4 – 22.6	CPL	$-1.06^{+0.06}_{-0.05}$	$796.^{+199.}_{-146.}$		$34.0^{+5.3}_{-4.4}$	0.92
061222A	81.9 – 87.9	CPL	$-0.80^{+0.17}_{-0.17}$	$269.^{+316.}_{-77.}$		$7.5^{+6.6}_{-1.8}$	0.91
070220	0.1 – 32.1	CPL	$-1.24^{+0.08}_{-0.07}$	$419.^{+189.}_{-116.}$		$20.3^{+4.9}_{-3.6}$	0.95
070508	2.2 – 18.2	CPL	$-1.07^{+0.07}_{-0.06}$	$283.^{+66.}_{-47.}$		$42.3^{+6.4}_{-4.9}$	0.66

Table 3.1: Best joint fit parameters. Spectral models considered are a Band function (Band et al. 1993), cutoff power law (CPL), and simple power law (PL). Errors are quoted at the 90% confidence level. Fluence is in the 15 keV–10 MeV band, and analysis times are relative to the BAT trigger time.

GRB	Instrument	α	$E_{\rm peak}$ (keV)	β	Fluence (erg/cm^2)	Fluence Energy Band	Reference
050717	RHESSI+BAT	-1.13±0.04	2240^{+480}_{-390}		$6.19^{+0.51}_{-0.53} \times10^{-6}$	20 keV–6 MeV	(a)
	Konus+BAT	$-1.11^{+0.11}_{-0.09}$	2401^{+781}_{-568}		$6.5^{+0.9}_{-2.2} \times10^{-6}$		(b)
061007	RHESSI+BAT	-0.85±0.04	478^{+52}_{-51}	$-2.47^{+0.23}_{-0.42}$	$2.43^{+0.23}_{-0.22} \times10^{-4}$	20 keV–10 MeV	(a)
	Konus	-0.70±0.04	399^{+19}_{-18}	$-2.61^{+0.15}_{-0.21}$	$2.49^{+0.17}_{-0.12} \times10^{-4}$		(c)
	WAM+BAT	-0.93±0.03	471±36	$-2.59^{+0.21}_{-0.36}$			(d)
061121	RHESSI+BAT	-1.31±0.04	740^{+210}_{-170}	$-2.37^{+0.31}_{-1.21}$	$5.85^{+0.51}_{-0.53} \times10^{-5}$	20 keV–5 MeV	(a)
	Konus	$-1.32^{+0.05}_{-0.04}$	606^{+90}_{-72}	< -2.7	$5.67^{+0.3}_{-0.5} \times10^{-5}$		(e)

Table 3.2: Comparison of the best-fit Band parameters by different instruments for GRBs 050717, 061007, and 061121. Parameter uncertainties are 90% C.L.
References: (a) This work (b) Krimm et al. (2006) (c) Golenetskii et al. (2006b) (d) Krimm et al. (2009) (e) Golenetskii et al. (2006a); Page et al. (2007)

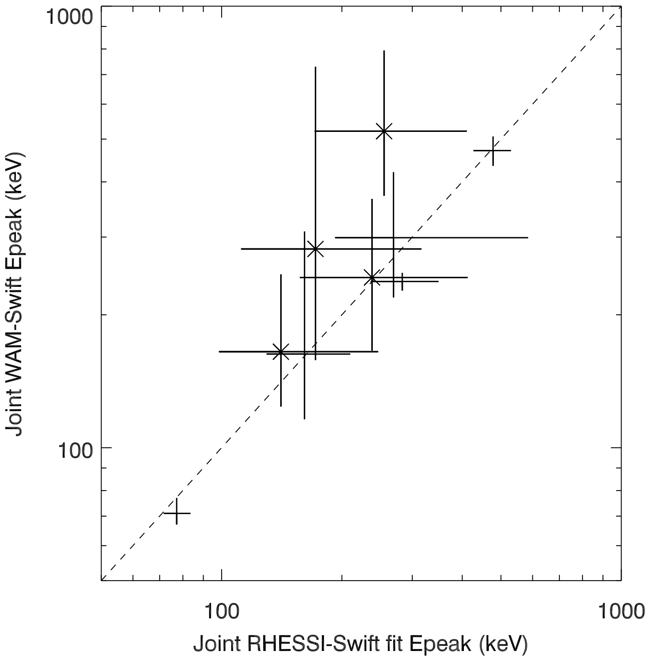

Figure 3.1: Comparison of the measured RHESSI+BAT E_{peak} values with the WAM+BAT values of Krimm et al. (2009). Points marked with a cross have RHESSI best fit values of $\beta > -2$, and hence E_{peak} is only a formal value, as the fit spectrum continues to rise. The error bars correspond to the 90% confidence level. The overplot line indicates equality of the measurements. The full BAT+WAM time intervals were an acceptable match to the RHESSI+BAT intervals except for the case of GRB061222A, for which the most appropriate time-resolved interval is plotted.

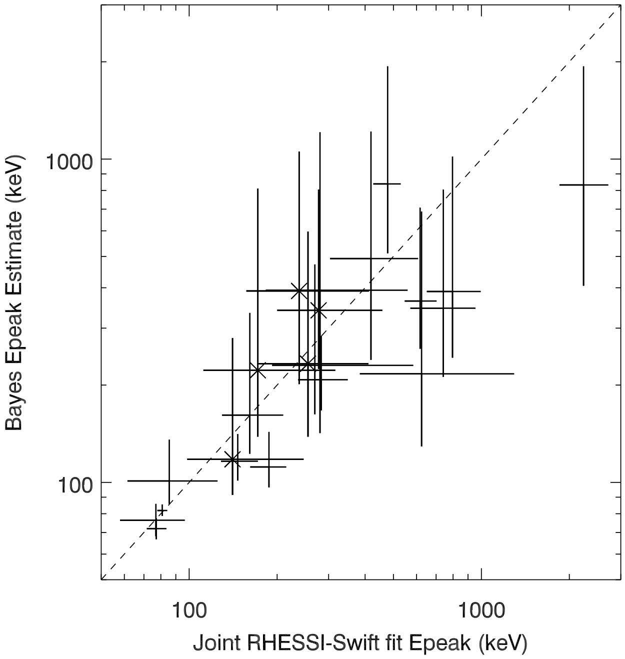

Figure 3.2: Comparison of the measured RHESSI+BAT $E_{\rm peak}$ values with those predicted by Butler et al. (2007). Symbols as in Figure 3.1.

3.3 Testing $E_{\rm peak}$ Estimators

The peak energy $E_{\rm peak}$ of the prompt GRB spectrum is crucial to determining overall burst energetics, and it plays a key role in several proposed luminosity indicators. The narrow passband of *Swift*-BAT prevents determination of $E_{\rm peak}$ for many bursts. Accordingly, a number of attempts have been made to infer $E_{\rm peak}$ from the BAT data alone. Butler et al. (2007) used a Bayesian fit method with priors determined from the BATSE catalog to estimate $E_{\rm peak}$. Zhang et al. (2007a) derived an $E_{\rm peak}$ – BAT power law index correlation using hardness ratios (see also (Zhang et al. 2007b)). Finally, Sakamoto et al. (2009) conducted Monte Carlo simulations to estimate $E_{\rm peak}$ in cases when a simple power-law model was the best fit to the BAT data. In Figures 3.2, 3.3, and 3.4, I compare the predictions of these models to the joint fit results.

The Bayesian model of Butler et al. (2007) shows good correspondence with the measured values (Figure 3.2). Above ∼600 keV, the predicted values of $E_{\rm peak}$ tend to be low, although their error bars reach near the measured values. This deviation is exaggerated somewhat, as the RHESSI data are for shorter, more intense (and typically harder) burst intervals than used in Butler et al. (2007).

Comparison of the Zhang et al. correlation-predicted $E_{\rm peak}$ to the measured RHESSI-

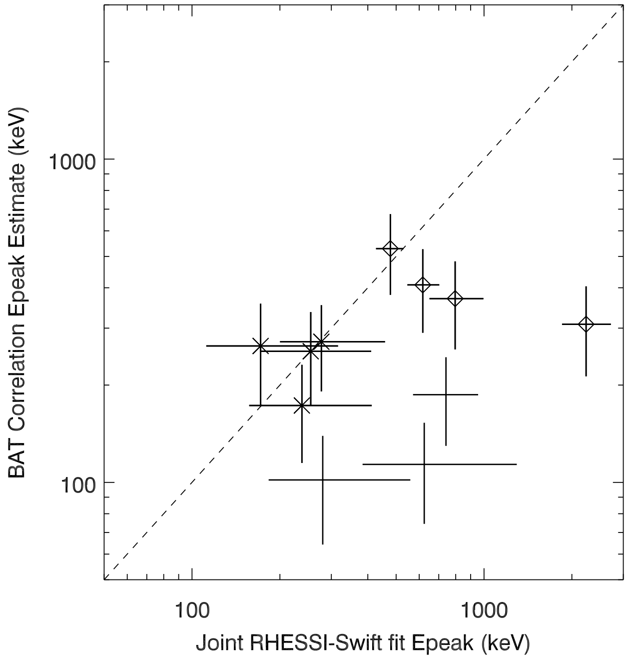

Figure 3.3: Comparison of the measured RHESSI+BAT $E_{\rm peak}$ values with those found with the correlation of Zhang et al. (2007a). Points marked with a diamond have BAT-only power law indices outside the range ($-2.3 < \alpha < -1.2$) likely to yield accurate predictions of $E_{\rm peak}$ (Zhang et al. 2007b). Other symbols as in Figure 3.1.

Swift values shows that this correlation appears to systematically under-predict the measured value of $E_{\rm peak}$, especially at high energy (Figure 3.3).

The results of the $E_{\rm peak}$ estimator of Sakamoto et al. (2009) are unsatisfactory (Figure 3.4). The predicted values of $E_{\rm peak}$ are systematically lower than the measured values. While the uncertainties on the predictions contain the measured value, they are so large as to automatically include most $E_{\rm peak}$ values observed (e.g., Figure 11 of Kaneko et al. 2006). The correlation is therefore unpredictive. Sakamoto et al. (2009) caution that their relation is intended to estimate $E_{\rm peak}$ within the BAT band (below 150 keV) and will not give correct results when the true value of $E_{\rm peak}$ is larger. However, such $E_{\rm peak}$ estimators are potentially useful primarily in cases when only BAT data is available. Since all estimates of this correlation will lie in the BAT band, there is no way to determine if the true $E_{\rm peak}$ is larger.

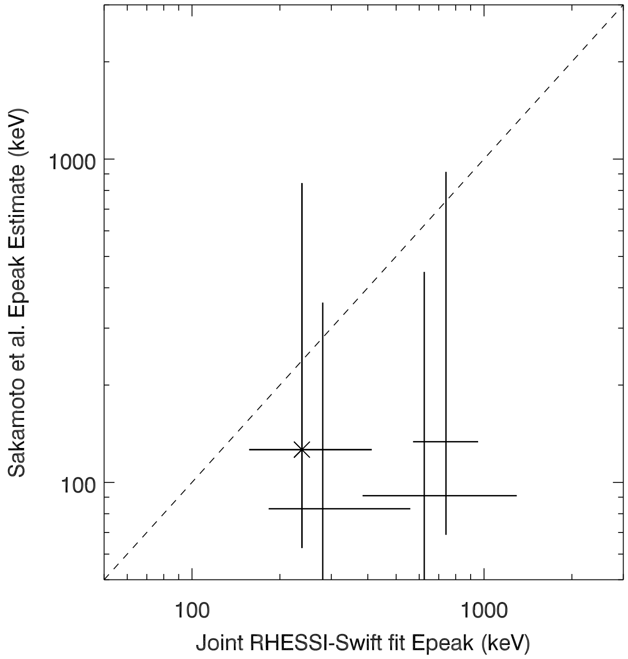

Figure 3.4: Comparison of the measured RHESSI+BAT E_{peak} values with those found with the simulation-derived correlation of Sakamoto et al. (2009). Other symbols as in Figure 3.1.

3.4 Summary

Joint fits of RHESSI and BAT GRB data for co-observed bursts have identified additional spectral parameters and helped to determine the overall burst energetics. These results show good correspondence with fits obtained with other instruments sensitive at energies higher than the BAT bandpass. I used the RHESSI+BAT sample to test three estimators intended to predict the value of E_{peak} from BAT data alone. A Bayesian estimator was most successful, while two estimators using correlations with BAT fit parameters gave unacceptable results. This analysis emphasizes the importance of cross-validating results with different instruments, as such efforts can help ensure the reliability of large-scale studies using data from BAT alone.

Chapter 4

RHESSI Tests of Quasi-Thermal Gamma-Ray Burst Spectral Models

Abstract

Prompt gamma-ray burst spectra evolve on short time scales, suggesting that time-resolved spectral fits may help diagnose the still unknown prompt emission mechanism. I use broad-band gamma-ray data from the RHESSI spacecraft to test quasi-thermal models with high signal-to-noise time-resolved spectra of nine bright gamma-ray bursts. In contrast to results reported in more narrow energy bands, the quality of the fits of quasi-thermal models is poor in relation to fits of the phenomenological Band function. Moreover, the best-fit parameters for the simplest quasi-thermal model, a black body plus a nonthermal power law, show significant dependence on the fit band. Models that replace the power law with more complicated nonthermal functions are not robust for the data considered here and decrease the physical relevance of the fit black body.

Portions of this work are taken from Bellm (2010) and are used here with permission.

4.1 Introduction

One of the most distinct features of the initial gamma-ray emission of gamma-ray bursts (GRBs) is its temporal variability. Significant evolution of the lightcurve and the spectrum occurs on timescales shorter than the total burst duration. Accordingly, spectral fits of subintervals of a burst may provide improved insight into the burst emission mechanism, at the cost of increased complexity.

When the Band et al. (1993) phenomenological spectral model (the “Band function,” a smoothly connected broken power law) was found to successfully fit the GRB prompt emission observed by BATSE, systematic time-resolved analyses of large burst samples focused on identifying patterns in the fit parameter evolution in an attempt to gain insight into the emission mechanism of long GRBs. Ford et al. (1995), Crider et al. (1997), and Preece et al. (1998b) considered the evolution of the peak energy $E_{\rm peak}$, low-energy power-law index α, and high-energy power-law index β, respectively. Broadly, these authors found a typical hard-to-soft decay of the emission and a general correlation of spectral hardness with intensity.

The observation of hard low-energy spectral slopes ($\alpha \sim +1$) in the initial portions of GRB pulses raised concerns about the viability of the synchrotron shock model, as $\alpha > -2/3$ violated the "line of death" for optically thin synchrotron (OTS) emission (Crider et al. 1997; Preece et al. 1998a; Ghirlanda et al. 2002; Preece et al. 2002). These violations, in concert with theoretical expectations from the fireball model (e.g., Mészáros & Rees 2000), led authors to suggest such emission could have a thermal origin (Crider et al. 1997; Preece 2000). Ghirlanda et al. (2003) found that time-resolved BATSE LAD spectra with hard low-energy indices could be acceptably fit with a black-body spectrum. This result was confirmed by Ryde (2004) for hard, single pulses. In some cases the addition of a simple power-law improved the correspondence with the high-energy LAD data. These successes led Ryde (2005) to propose that all GRB emission might be decomposed into thermal and nonthermal components of similar magnitude, with the black-body emission providing the spectral peak of the prompt emission. Within the LAD band, a simple power law proved a sufficient approximation to the more complicated true nonthermal emission, with the resulting black-body plus power-law model (BBPL) fits having similar χ^2 values as the Band function for identical degrees of freedom. In Ryde et al. (2006), the authors noted that the power-law slope of the BBPL model avoided the OTS line of death and sought to interpret the black body fit results in the context of a photospheric model. Most recently, Ryde & Pe'er (2009) (hereafter, RP09) identified regularity in the time evolution of the temperature and flux of the black-body component for single-pulse bursts and linked the normalization of the black-body component to the size of the thermal emitting region (see also Pe'er et al. 2007).

While the simple power-law approximating the nonthermal emission in the BBPL model is effective over the moderate energy band (28 keV–1.8 MeV) of the BATSE LAD detectors, tests of the BBPL model using data covering a broader bandpass have had mixed results. McBreen et al. (2006) successfully fit the BBPL model to GRB 041219A data from *INTEGRAL*-SPI spanning the range 20 keV–8 MeV, although the black body contributed only a small portion of the flux of the main burst. Foley et al. (2008) obtained acceptable time-integrated fits of the BBPL model to GRBs observed by *INTEGRAL*-IBIS and SPI, although the IBIS detection requirement created a burst sample with relatively low peak spectral energies ($E_{\rm peak} \lesssim 150$ keV). Ghirlanda et al. (2007) considered BATSE bursts co-observed in the X-ray by the Beppo-SAX WFC. Time-resolved spectra were not available for the WFC data, but a summation of the time-resolved BBPL fits to the BATSE data led to a significant over-prediction of the WFC flux, while a similar extrapolation of the summed time-resolved Band function fits was much more successful.

In this work, I have employed data from the Ramaty High Energy Solar Spectroscopic Imager (RHESSI) (Lin et al. 2002) to investigate the behavior of quasi-thermal spectral models over a broad energy band. RHESSI's nine coaxial germanium detectors image the

Sun at X-ray to gamma-ray energies (3 keV–17 MeV) with excellent resolution in energy (1–5 keV) and time (1 binary μs) (Smith et al. 2002). RHESSI's detectors are effectively unshielded above ∼30 keV and receive emission from astrophysical sources like GRBs with a total effective area of ∼150 cm^2. Each coaxial detector is electronically segmented into thin front and thick rear segments; most off-axis emission is recorded in the rear segments. The satellite rotates with a period of about 4 seconds.

4.2 Data Analysis

4.2.1 Sample Selection

The identification of optimal fit intervals for time-resolved spectral fitting requires balancing the need for high signal-to-noise (in order to constrain the fit parameters of the spectral models) with the goal of the finest possible time resolution. In my previous systematic analysis of RHESSI GRBs (Bellm et al. 2008a), I found that a S/N ratio of at least 45 was required for adequate fitting of the most complicated models. This value is also consistent with those adopted by previous studies of time-resolved BATSE spectra (Crider et al. 1997; Kaneko et al. 2006).

Because bursts may have periods of high signal which are degraded to low S/N when integrated over the whole burst, I chose candidate bursts from the RHESSI sample[1] with localizations and total S/N > 30. Radiation damage to RHESSI's germanium detectors has slowly degraded spectral performance; I restricted the analysis to detectors which do not show signs of radiation damage. I therefore considered bursts from the RHESSI launch in February 2002 through June 2006, after which all nine RHESSI detectors were damaged. Forty-five GRBs met these criteria.

To identify subintervals within each candidate burst, I used the Bayesian Blocks algorithm (Scargle 1998), which identifies the most probable segmentation of a burst lightcurve into intervals of constant Poisson rate. I modified the stopping criterion to generate subintervals of appropriate S/N. Since the RHESSI data are stored event by event, this "top-down" identification of the burst subintervals is more natural than building up data accumulated on fixed timescales until a minimum S/N is reached. While previous work on quasi-thermal models has focused on spectral evolution within pulses, my segmentation method does not require pulse modeling. This approach was necessary, as the bright bursts in this sample generally have irregular temporal structure, but it also avoids imposing additional implicit selection effects on the burst sample.

I applied the Bayesian Blocks algorithm to the raw RHESSI eventlist to identify the most probable segmentation points. The time variation of the background, while present, does not dominate the GRB variability. In my modified stopping criterion, I computed the background-subtracted S/N (in the 60 keV–3 MeV band) for each proposed subinterval. If the S/N ratios of both subintervals were greater than 15, the segmentation was allowed.

---

[1] `http://grb.web.psi.ch/`

GRB	Off-Axis Angle	T_0 (UT)	Interval Edges (sec)
		High S/N Sample	
020715	72°	19:21:08.666	0.000, 0.356, 0.646, 3.336
021008A	50°	07:01:01.399	0.000, 1.265, 1.985, 2.541, 2.727, 2.934, 3.142, 3.278, 3.542, 3.889, 4.054, 4.314, 4.438, 4.995, 8.153, 8.617
021206	18°	22:49:12.951	0.000, 1.983, 2.163, 2.267, 2.405, 2.626, 3.012, 3.176, 3.377, 3.487, 3.559, 3.629, 3.714, 3.809, 3.871, 3.959, 4.024, 4.099, 4.361, 4.618, 4.699, 4.792, 4.945, 5.068, 5.168, 5.346, 5.552, 5.718, 6.112, 6.217, 6.603, 6.906
030329A	144°	11:37:25.954	0.000, 2.266, 2.833, 3.520, 3.979, 4.351, 5.019, 6.226, 13.431, 14.335, 15.006, 15.687, 17.553
030519B	166°	14:04:52.951	0.000, 5.769, 6.352, 6.726, 7.027, 7.214, 7.625, 11.065
031027	102°	17:07:37.744	0.000, 3.236, 4.774, 6.065, 9.469
031111	156°	16:45:20.776	0.000, 0.329, 0.971, 1.329
040228	163°	00:08:50.910	0.000, 4.751, 6.291, 8.458, 13.995, 15.009, 17.221, 17.563, 18.338, 22.981, 27.748
040810	144°	14:16:40.241	0.000, 17.055, 24.995, 45.637
		Single-Pulse Sample	
020715	72°	19:21:07.907	0.000, 0.543, 0.759, 1.115, 1.236, 1.397, 1.521, 1.810, 5.135
030329A	144°	11:37:25.954	0.000, 2.280, 2.895, 3.356, 3.997, 4.355, 5.020, 5.287, 5.743, 6.287, 7.529, 9.616, 13.523
060805B	97°	14:27:15.989	0.000, 1.245, 1.632, 2.537, 3.428, 4.451

Table 4.1: Intervals used for spectral fitting. The intervals are quoted relative to the start time T_0.

For each subinterval, we applied the Bayesian Blocks algorithm again if the S/N of that interval was greater than 45. After segmentation halted, I dropped any leading or trailing subintervals with $S/N < 45$ and combined any "interior" subintervals with low S/N with the adjacent subinterval with lower S/N. The resulting subintervals all have $S/N > 45$. I conducted spectral fitting only on bursts with at least three subintervals.

The resulting burst sample consists of nine bursts and a total of 88 subintervals. Table 4.1 lists the bursts and intervals considered in this work. Figure 4.1 shows the distribution of subinterval length and S/N. These bursts are predominantly from early in the RHESSI mission because for those bursts a greater number of the detectors remained unaffected by radiation damage.

In order to investigate the spectral evolution of single GRB pulses in Section 4.4.3, it was necessary to set a lower S/N threshold. I used the modified Bayesian Blocks routine to identify subintervals with $S/N > 25$ within single, separated pulses. This "single-pulse" sample yielded 25 subintervals within 3 GRBs (Table 4.1).

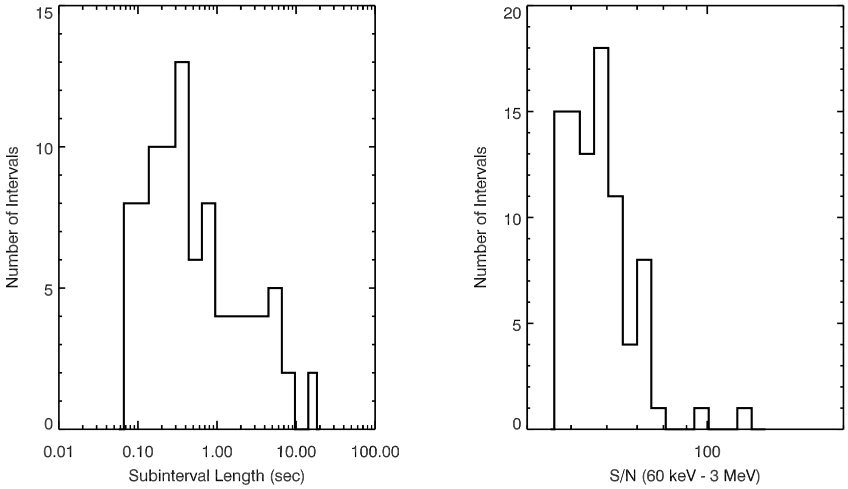

Figure 4.1: Distribution of subinterval length and signal-to-noise ratio for the high S/N burst sample considered here.

4.2.2 Spectral Fitting

Fit Methods

The RHESSI data were extracted in SSW-IDL[2]. I fit a third-order polynomial to background intervals immediately before and after the burst, allowing for a potential periodic modulation of the background with the RHESSI rotation. I selected energy binning for the spectra by requiring at least ten counts in each bin of the raw source spectrum. I used the same energy bins for all subintervals of each burst. Both the source and background spectra covered the energy range 30 keV–17 MeV.

I determined RHESSI's spectral response by simulating monoenergetic photons impinging on a detailed mass model in the Monte Carlo suite MGEANT (Sturner et al. 2000). For a grid of angles relative to the spacecraft rotation axis, I simulated photons along 60° arcs in rotation angle. After interpolating to the appropriate off-axis angle, I weighted the 60° sector responses by the burst light curve to generate the total response. Since many of the subintervals considered in this work were shorter than one-sixth of RHESSI's four second rotation period, responses for short intervals were often single sector responses. Our simulations indicate that the spectral response does not vary appreciably on shorter scales in rotation angle.

I utilized ISIS v1.4.9 (Houck & Denicola 2000) for spectral fitting. Fitting was automated via an ISIS script and the results stored in a database.

I used data from the RHESSI rear segments only for all bursts except for GRBs 021206

---

[2] `http://www.lmsal.com/solarsoft/`

and 021008A, which had off-axis angles small enough (18° and 50°, respectively) that appreciable counts were recorded in the front segments. (Coincidentally, these bursts also both had data decimation in the rear segments—only a fraction of the observed counts were recorded.) The fit energy band was 30 keV–17 MeV, with some exceptions: GRB 021206 had significant atmospheric backscatter in the rear segments (Wigger et al. 2008), so the front and rear segment data were kept separate and fit over the range 30 keV–2800 keV and 300 keV–17 MeV. (For all other bursts, data from all detectors were combined into a single spectrum.) GRBs 030519B and 040228 came through the extreme rear of the RHESSI cryostat (166° and 163°), where the low-energy response is more sensitive to the detailed mass modeling, so a fit range of 50 keV–17 MeV was employed. Finally, GRB 021008A required a fit band of 100 keV–17 MeV for adequate fitting; Wigger et al. (2008) found similar behavior in a time-integrated fit of this data.

Spectral Models

I fit both the time-resolved and the time-integrated spectra with a variety of spectral models commonly used to represent the GRB prompt emission. The Band function (Band) is a phenomenological model which fits the vast majority of broadband prompt spectra (Band et al. 1993). It is a broken power law with a smooth transition between the upper and lower power laws:

$$N_E = \begin{cases} A(E/E_{piv})^{\alpha}\exp(-E(2+\alpha)/E_{\mathrm{peak}}) & E < E_{break} \\ B(E/E_{piv})^{\beta} & E > E_{break} \end{cases} \tag{4.1}$$

with $E_{break} \equiv E_0(\alpha-\beta)$ and $B \equiv A(\frac{(\alpha-\beta)E_0}{E_{piv}})^{\alpha-\beta}\exp(\beta-\alpha)$. For $\beta < -2$ and $\alpha > -2$, E_{peak} corresponds to the peak of the νF_ν spectrum. The normalization A has units of photons cm^{-2} s^{-1} keV^{-1}, and E_{piv} is here taken to be 100 keV.

While the Band function is often assumed to be the "true" spectral model in fits of GRB spectra, data obtained over a more limited energy band or at lower S/N may not be sufficient to constrain its parameters. I also tested other empirical models with fewer free parameters. The cutoff power law (CPL) is equivalent to the Band function below E_{break}:

$$N_E = A(E/E_{piv})^{\alpha}\exp(-E(2+\alpha)/E_{\mathrm{peak}}) \tag{4.2}$$

I also fit a single power law (PL): $N_E = A(E/E_{piv})^{\alpha}$. While the PL model was a poor fit to these spectra, its fit spectral index was useful in comparison with the other models.

The simplest quasi-thermal spectral model is a black body plus power law model (BBPL). Proposed by Ryde (2005), it consists of Planck function and a simple power law:

$$N_E = A\frac{(E/E_{piv})^2}{\exp E/kT - 1} + B(E/E_{piv})^s \tag{4.3}$$

The approximation of the nonthermal emission by a simple power-law is generally sufficient over the BATSE energy band (Ryde 2005). However, it is not expected to fit over a broader band (Ryde 2004, 2005; Ryde & Pe'er 2009). Like the PL model, it diverges unphysically.

More sophisticated quasi-thermal models replace the nonthermal PL in the BBPL with an empirical function with more free parameters. I attempt to fit a black body plus cutoff power law (BBCPL) model as well:

$$N_E = A\frac{(E/E_{piv})^2}{\exp E/kT - 1} + B(E/E_{piv})^{\alpha}\exp(-E(2+\alpha)/E_{\mathrm{peak}}) \tag{4.4}$$

(I retain the notation of E_{peak} for the cutoff parameter of the BBCPL model for clarity of comparison, but in some cases the true peak of the νF_{ν} spectrum may be due to the peak of the black-body component at 3.92 kT.) However, the addition of more free fit parameters leads to convergence problems even with the relatively high S/N broad-band spectra. In addition to the unconstrained fits of the BBCPL model, then, I also perform fits in which the variation of the model temperature is constrained to an expected range. I describe the specifics of this constrained quasi-thermal model in the text below.

Given the convergence problems faced by the BBCPL model, I have not attempted fits of a black body + Band model, which contains an additional free parameter. In most cases, the simple CPL model provides an adequate representation of the RHESSI data, with the Band model offering only moderate improvements. Accordingly, the BBCPL model should provide a sufficient test of the importance of the black-body component over the RHESSI band.

4.3 Fit Results

I present the time-evolution of the fit parameters of the Band and BBPL models in Figures 4.2–4.10. The quality of the fits and the constraint of their parameters were generally good. For GRB 021206, the goodness of fit was poorer for some subintervals because of the separation of front and rear data. Slight offsets in the background subtraction created disagreements about the overall model normalization and increased the χ^2. I elected to take the averaged fluence value produced by the fit rather than introduce a fit normalization offset between the front and rear data for this burst. For GRB 021008A, the only other burst with front segment data, the combination of front and rear segment spectra averaged out such background subtraction problems and obviated the need for such offsets.

Wigger et al. (2008) fit RHESSI data for many of these bright bursts using an identical mass model but independent analysis and fit procedures. My fits of the total burst intervals are a good match to those results (Table 4.2). In the case of GRB 021206, the presence of excess high-energy emission not well-modeled by the Band function increased the χ^2 value for the fit to 17 MeV. (This component likely also contributed to the poor goodness of fit for this burst in the time-resolved fits, as discussed above, although its impact is harder to ascertain.) *HETE*-2 also observed three bursts in this sample. RHESSI fit higher E_{peak}

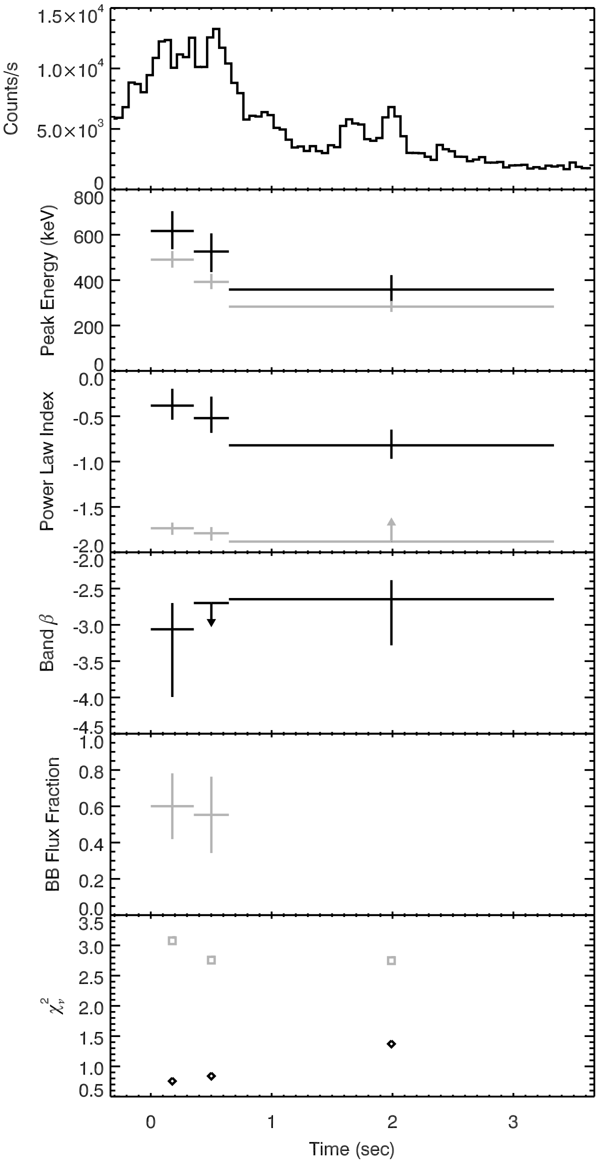

Figure 4.2: Spectral evolution of GRB 020715. The 60 keV–3 MeV lightcurve has 0.05 s time bins; counts are shown only for those segments used in the fits. The fit model parameters are black for the Band model and gray for the BBPL model. All errors are 90% C.L. Peak energies are $E_{\rm peak}$ for the Band model and 3.92 kT for the BBPL model. The Band model α is plotted with the power-law index s of the BBPL model. The errors on the fraction of the flux provided by the black body in the RHESSI band were estimated from a Monte Carlo bootstrap. Points where the value was unconstrained in the fit are omitted from the plot.

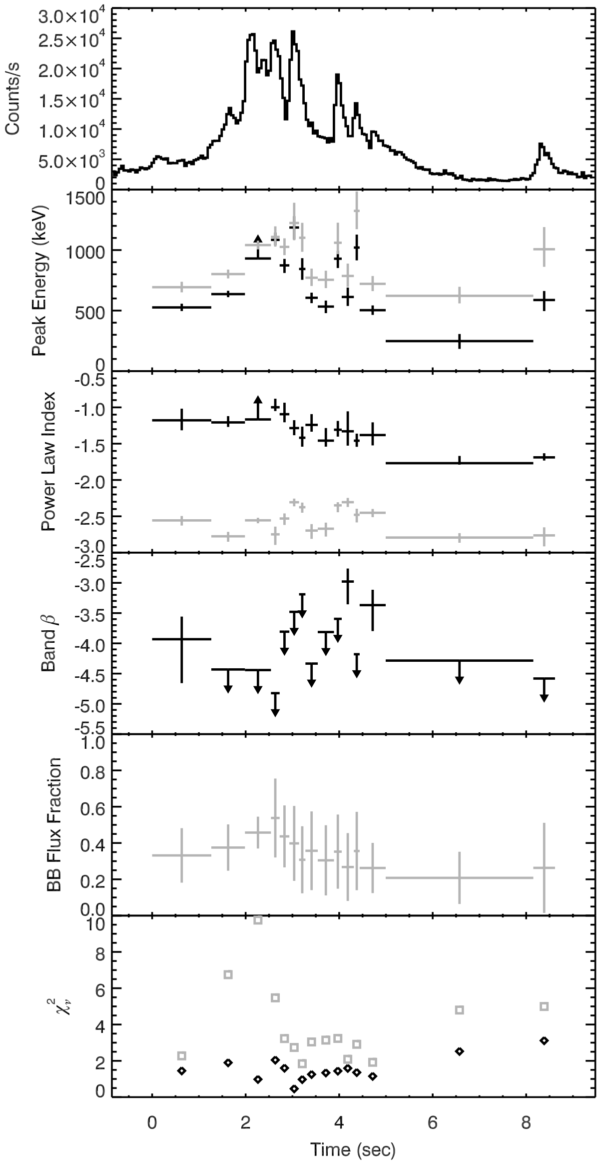

Figure 4.3: Spectral evolution of GRB 021008A. Symbols as in Fig. 4.2.

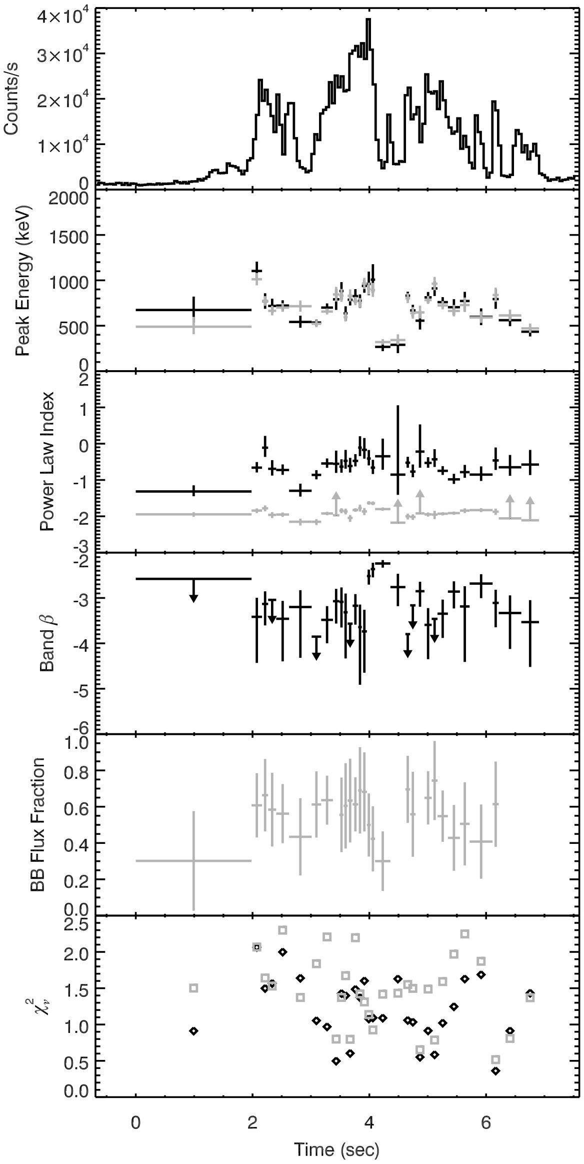

Figure 4.4: Spectral evolution of GRB 021206. Symbols as in Fig. 4.2.

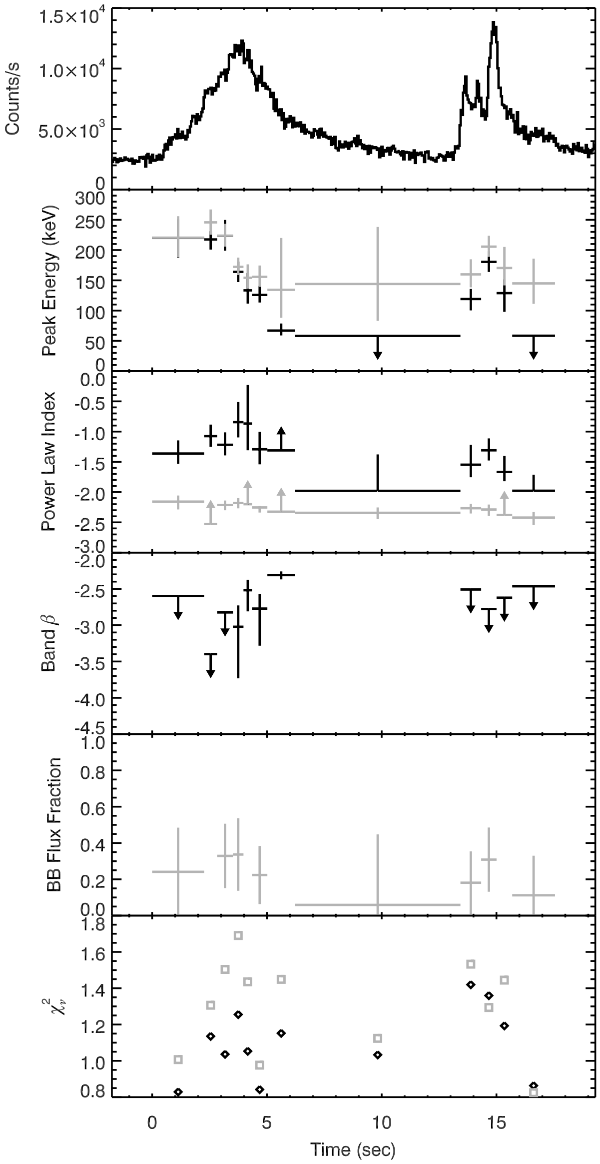

Figure 4.5: Spectral evolution of GRB 030329. Symbols as in Fig. 4.2.

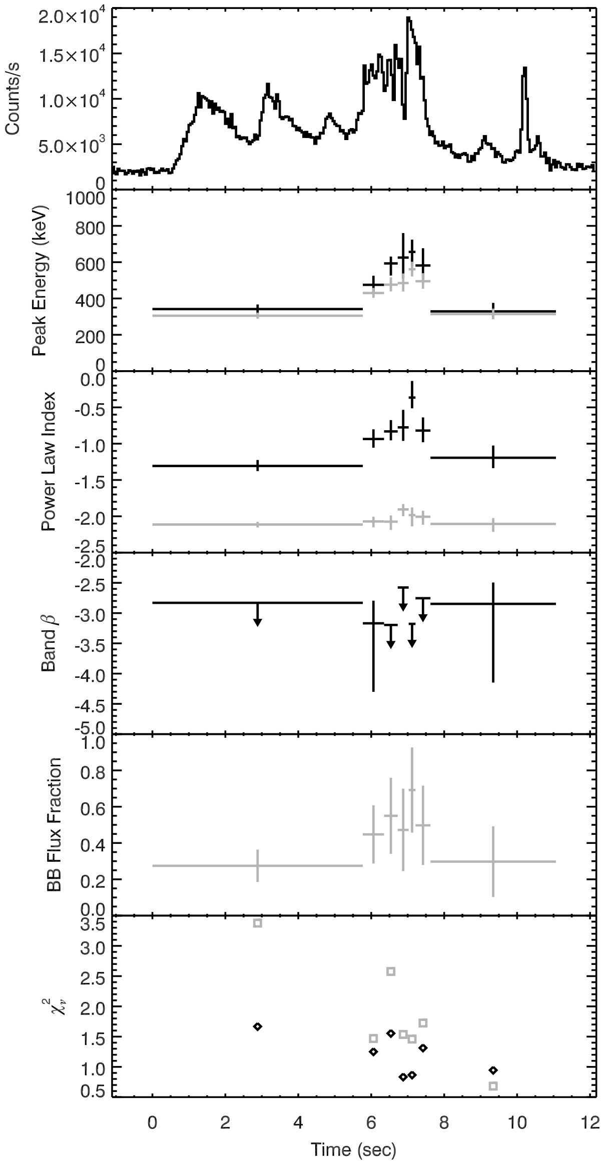

Figure 4.6: Spectral evolution of GRB 030519. Symbols as in Fig. 4.2.

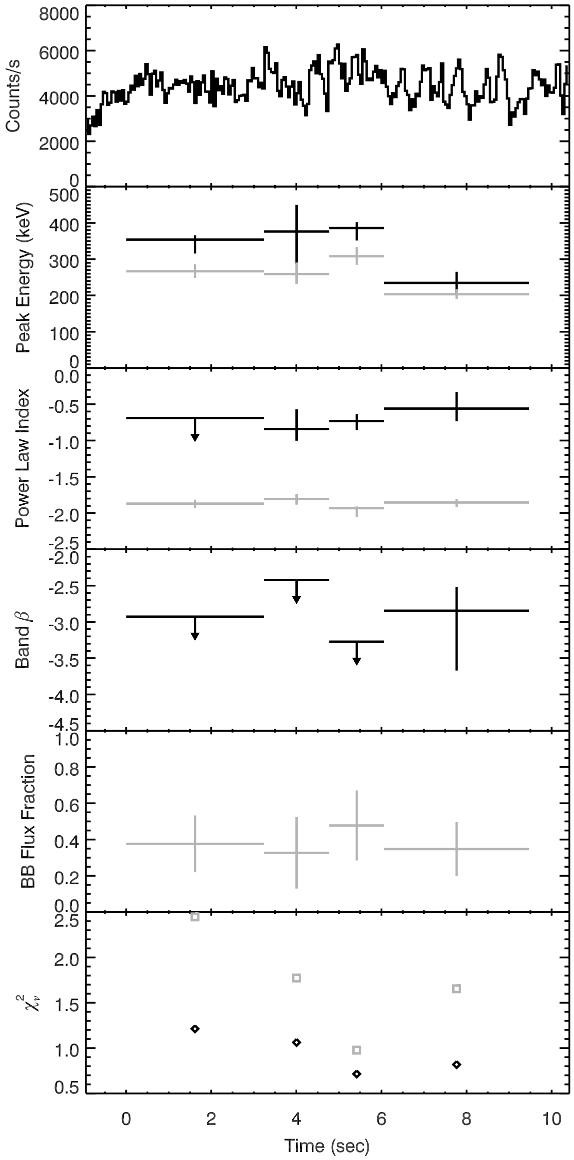

Figure 4.7: Spectral evolution of GRB 031027. Symbols as in Fig. 4.2. The lightcurve appears flat because the background level is not visible in the time interval plotted.

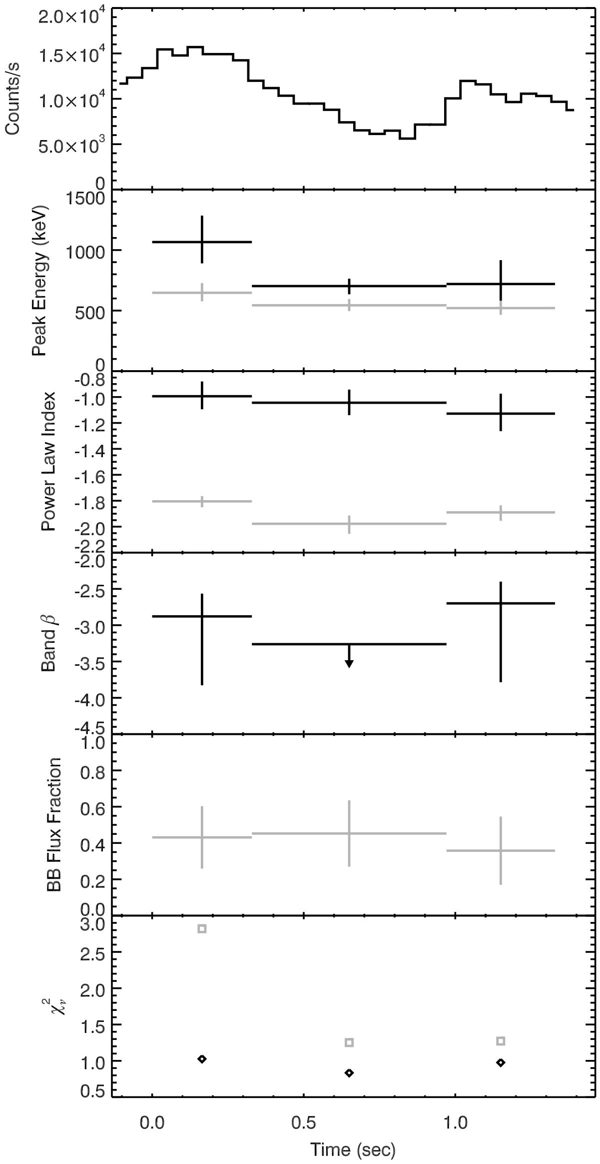

Figure 4.8: Spectral evolution of GRB 031111. Symbols as in Fig. 4.2.

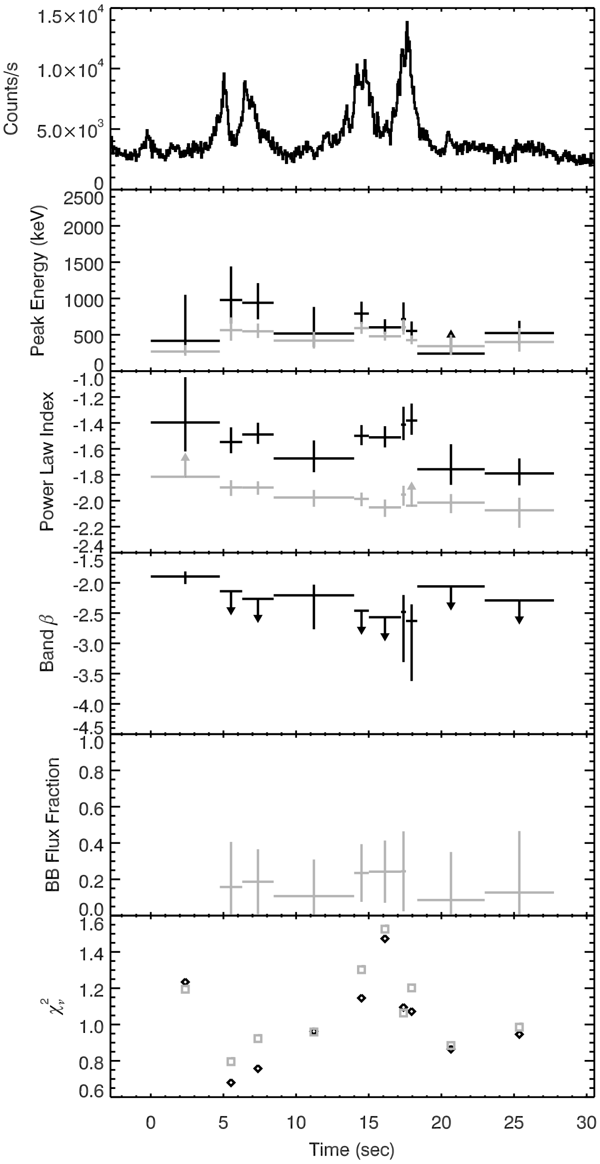

Figure 4.9: Spectral evolution of GRB 040228. Symbols as in Fig. 4.2.

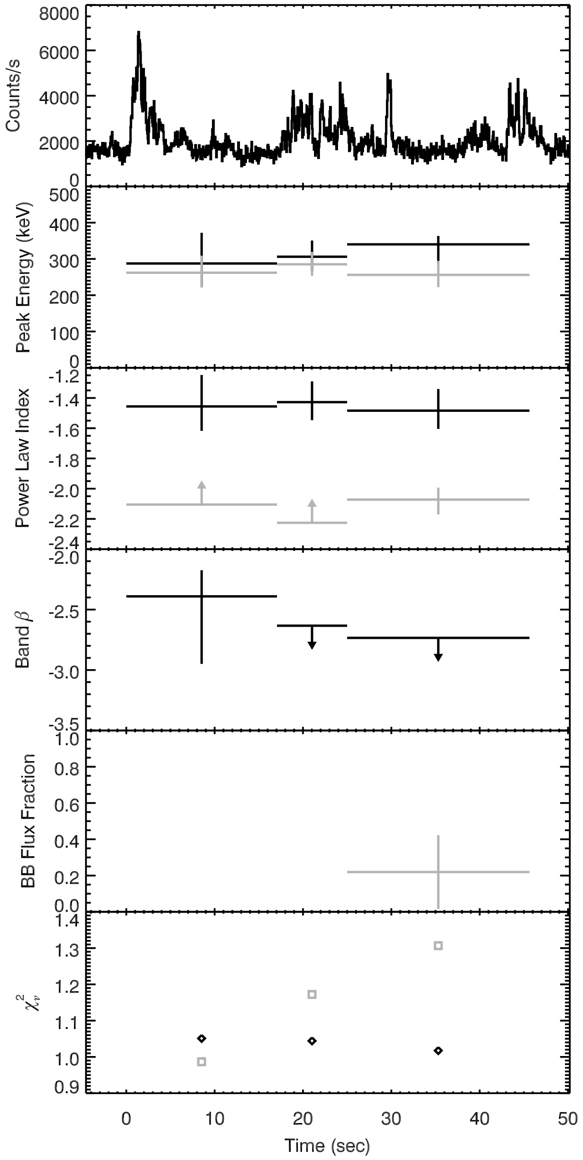

Figure 4.10: Spectral evolution of GRB 040810. Symbols as in Fig. 4.2.

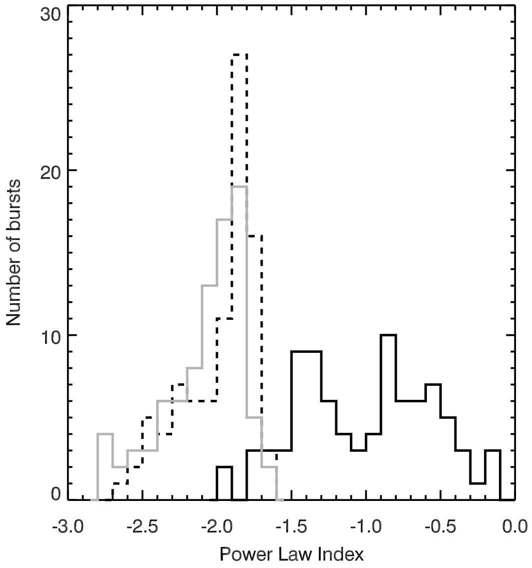

Figure 4.11: Histogram of the fit low-energy power law indices for the Band model (solid black), BBPL model (solid gray), and simple power-law model (dashed black). The indices of the PL model and the BBPL model are highly correlated. The apparent bimodality of the Band α index is likely an artifact of the limited burst sample (Section 4.3).

values for all three bursts; in two of the cases, the peak energies were above the 400 keV upper bound of the *HETE* energy band.

The distributions of the best-fit parameters differ somewhat from the BATSE results obtained by Kaneko et al. (2006). For my time-resolved Band function fits, the mean α is -1.00 with standard deviation 0.47 (Figure 4.11). The RHESSI mean E_{peak} is 580 ± 280 keV, and β has mean -3.50 and standard deviation 0.89. The time-resolved BATSE results for all good Band fits are $\alpha = -0.90^{+0.34}_{-0.39}$, $E_{\text{peak}} = 268^{+188}_{-145}$ keV, and $\beta = -2.33^{+0.39}_{-0.47}$, where I have converted the quartile dispersions to 1σ uncertainties under the simplifying assumption of an underlying normal distribution. Using Levene's test, I find that the variances of the BATSE and RHESSI distributions are consistent. Since the RHESSI distributions are not normal, I cannot compare the means using Student's t-test. The nonparametric Kolmogorov-Smirnov test rejects the null hypothesis BATSE and RHESSI parameter samples are drawn from the same distribution. However, this result is not surprising, given the different fit energy ranges and the few RHESSI bursts fit here. Of the three parameters, the alpha distributions are most consistent despite the apparent bimodality of the RHESSI sample (Figure 4.11).

GRB	Instrument	Fit Band	α	E_{peak} (keV)	β	χ^2/dof	Reference
020715	RHESSI	30 keV–17 MeV	$-0.71^{+0.11}_{-0.10}$	477^{+59}_{-52}	$-2.79^{+0.24}_{-0.50}$	34.5/26	(1)
	RHESSI	30 keV–15.7 MeV	-0.776±0.072	531±39	-3.14±0.41	106.3/113	(2)
021008A	RHESSI	100 keV–17 MeV	$-1.360^{+0.035}_{-0.034}$	733^{+16}_{-16}	$-3.59^{+0.11}_{-0.14}$	59.7/30	(1)
	RHESSI	300 keV–15.7 MeV	-1.493±0.092	677±54	-3.73±0.30	79.5/84	(2)
021206	RHESSI	30 keV–17 MeV	$-0.817^{+0.031}_{-0.030}$	718^{+17}_{-17}	$-2.912^{+0.053}_{-0.059}$	118/68	(1)
	RHESSI	70 keV–4.5 MeV	-0.692±0.033	711±12	-3.19±0.07	176.5/174	(2)
030329A	RHESSI	30 keV–17 MeV	$-1.648^{+0.060}_{-0.053}$	139^{+7}_{-7}	$-3.03^{+0.24}_{-0.53}$	101.4/46	(1)
	RHESSI (peak 1)	34 keV–10 MeV	-1.608±0.063	157.2±8.6	-3.48±0.87	84.3/90	(2)
	RHESSI (peak 2)	34 keV–7 MeV	-1.78±0.11	85±18	-3.04±0.49	103.3/83	(2)
	HETE	2 keV–400 keV	-1.32±0.02	70.2±2.3	-2.44±0.08	...	(3)
	HETE	2 keV–400 keV	$-1.26^{+0.01}_{-0.02}$	68±2	$-2.28^{+0.05}_{-0.06}$	213.7/139	(4)
030519B	RHESSI	50 keV–17 MeV	$-1.171^{+0.049}_{-0.046}$	437^{+23}_{-22}	$-3.11^{+0.23}_{-0.40}$	66/35	(1)
	RHESSI	70 keV–15 MeV	-1.048±0.069	417.2±21	-3.11±0.30	86.3/75	(2)
	HETE	2 keV–400 keV	-0.8±0.1	138^{+18}_{-15}	-1.7±0.2	92.0/124	(4)
031027	RHESSI	30 keV–17 MeV	$-0.759^{+0.089}_{-0.080}$	319^{+26}_{-24}	< -2.79	63.9/56	(1)
	RHESSI	60 keV–6 MeV	-0.94±0.13	338±25	...	...	(2)
031111	RHESSI	30 keV–17 MeV	$-1.071^{+0.073}_{-0.061}$	841^{+96}_{-89}	$-2.83^{+0.22}_{-0.38}$	50.2/56	(1)
	RHESSI	38 keV–15.7 MeV	-1.102±0.059	844±97	-2.364±0.11	128.3/117	(2)
	HETE	2 keV–400 keV	$-0.82^{+0.05}_{-0.5}$	404^{+68}_{-51}	...	...	(5)
040228	RHESSI	50 keV–17 MeV	$-1.60^{+0.037}_{-0.034}$	769^{+120}_{-99}	$-2.50^{+0.18}_{-0.36}$	107.9/84	(1)
040810	RHESSI	30 keV–17 MeV	$-1.45^{+0.12}_{-0.10}$	321^{+50}_{-45}	< -2.52	55.7/56	(1)

Table 4.2: Comparison of time-integrated Band fit parameters for bursts fit in other works. Results of the closest analogous fit are shown. Only the limits of the RHESSI fit energy band are presented when different ranges were used for the front and rear segments. Parameter uncertainties have been converted to 90% C.L. where necessary. References: (1) This work (2) Wigger et al. (2008) (3) Vanderspek et al. (2004) (4) Sakamoto et al. (2005) (5) Pélangeon et al. (2008)

4.4 Evaluating Quasi-thermal Models

I did not attempt to determine the best-fit model for each subinterval spectrum fit in this work. The Maximum Likelihood Ratio Test and the related F-test frequently used in model comparisons are not applicable for the models I employ here—the model parameters are not nested subsets of one another, and so the distribution of the likelihood ratio is unknown (Eadie et al. 1971; Freeman et al. 1999). Instead, I have opted to evaluate the effectiveness of the quasi-thermal models in three ways: first, by directly comparing goodness-of-fit for those pairs of quasi-thermal and empirical models with identical degrees of freedom; second, by assessing the physical plausibility of the model fits; and third, by considering the robustness of the fits and their relative consistency with each other and previous work.

To anticipate my conclusions, I find poor goodness of fit of the BBPL model, which may be attributed to the inadequacy of the simple PL over the RHESSI band. However, the potentially more realistic BBCPL model fit is dominated by its CPL component, which is virtually indistinguishable from the simple Band fit for these data. Accordingly, even statistically rigorous determination of the best-fit model[3] is unlikely to provide insight into the properties of the thermal component. Qualitative assessment of the behavior of the fit black body is sufficient to allow us to draw conclusions from these data.

4.4.1 BBPL

I begin by considering the simplest quasi-thermal model, the black body + simple power law (BBPL). This model is not expected to be effective over a broad energy band (e.g., Ryde 2005; Ghirlanda et al. 2007). It is instructive to ask, however, how the properties of the BBPL fits change when fit over a broader band. In particular, evidence of band-dependence calls into question the universality of results obtained even in a narrow band centered on the peak of the prompt emission.

The Band and BBPL models each have four fit parameters ($\alpha, E_{\mathrm{peak}}, \beta$, and the normalization for Band; kT, s, and the two normalizations for the BBPL). Comparing their χ^2 values for each subinterval (see Figure 4.12), I found that in 73 of 88 cases, the Band function has a lower χ^2 value and is thus statistically favored.

As in previous studies, I found that the peak of the blackbody emission (3.92 kT) in BBPL fits corresponded closely to the value of E_{peak} obtained in Band fits (Figure 4.13b). Moreover, the contribution of the BBPL black-body flux to the overall flux in the band was significant (Figure 4.14).

Contrary to my expectation, I did not find systematic deviation in the residuals of the fit BBPL model at low or high energy. Such deviation would be symptomatic of the need for additional spectral components (e.g., Ryde & Pe'er 2009).

RHESSI's broader energy band did affect the best-fit value of s, the power law index of the BBPL model. The distribution of s reported by Ryde et al. (2006) peaks around -1.5,

---

[3] e.g., via a Monte Carlo bootstrap or Bayesian hypothesis testing.

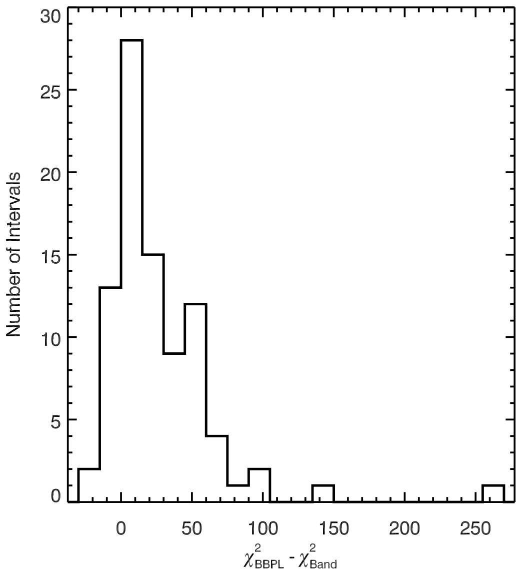

Figure 4.12: Difference in the χ^2 values for fits to the BBPL and Band models, which have identical degrees of freedom. The BBPL χ^2 value is larger in the majority of cases, indicating that the Band model is generally preferred. The few cases where the BBPL model is a better fit are irregularly distributed throughout the sample with no characteristic trend (Figures 4.2–4.10).

while my histogram of s peaks near -1.9 (Figure 4.11). This shift may be due to the small sample of bursts fit here, although as discussed in Section 4.3 the fit Band index α shows only a small shift compared to the BATSE sample.

However, a softer fit index is expected when fitting a power law to GRB data extending to higher energies, as GRB spectra generically fall off more sharply above E_{peak}. The fit single power law index is thus a band-dependent average of the more complicated spectral shape. Indeed, the distribution of s obtained is quite similar to that of the index of a simple power-law fit to these data (Figure 4.11), and s is highly correlated with the fit PL index for individual intervals. Since the asymptotic spectral index must be greater than -2 below the peak energy and less than -2 above it, fitting a power law to a band of sufficient width which includes the peak energy will average to an intermediate value.

One of the strengths of the BBPL model is that its nonthermal component typically is softer than the “line of death” of $-2/3$ predicted for optically thin synchrotron emission. However, this argument appears to be weakened by the sensitivity of the fit power-law index to the range of the data above the peak energy. It is not clear that the fit value of s provides useful insight into the nonthermal emission physics, as its value may be an artifact of the fit band.

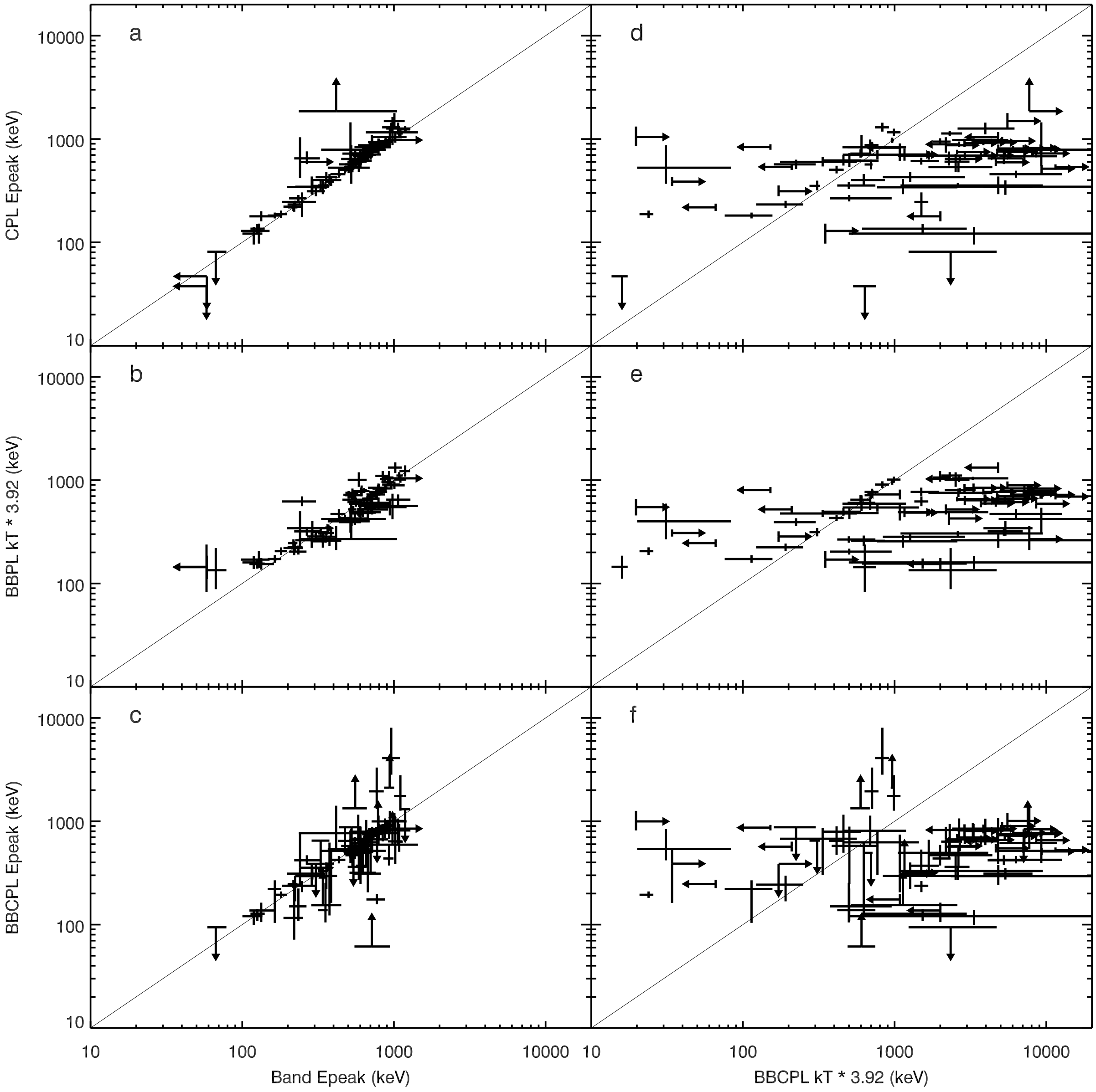

Figure 4.13: Comparison of peak energies obtained in Band, CPL, BBPL, and BBCPL fits. As expected, there is good agreement between the E_{peak} values of the Band and CPL models (panel a). Notably, the black-body peak (3.92 kT) of the BBPL model and the BBCPL E_{peak} parameter also match the Band function E_{peak} (panels b and c). However, the black-body peak of the BBCPL model shows little correlation with the spectral peak identified by the other models (panels d–f). A few points which were completely unconstrained in one dimension are omitted in the plot.

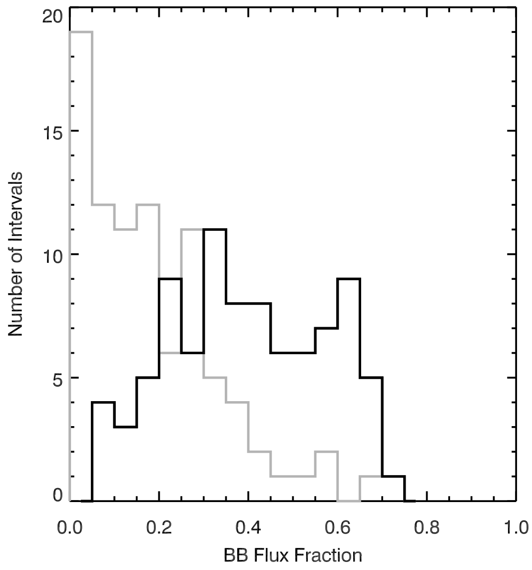

Figure 4.14: Histogram of the proportion of flux in the RHESSI band contributed by the black-body component in the BBPL (black) and BBCPL (gray) models. With the nonthermal component providing the spectral break in the BBCPL model, the relevance of the black body component diminishes.

4.4.2 BBCPL and Variants

Given the challenges faced by the BBPL model in the RHESSI band, we tried more complicated nonthermal components in an attempt to find a functional broad-band quasi-thermal model. I sought to evaluate the efficacy and robustness of such models and to assess whether the thermal component retained physical relevance and realism.

After a simple power-law, the cutoff-power law (CPL) model is the next most basic nonthermal model. Unlike the PL model, it has the advantage of providing a generally adequate representation of the RHESSI data considered here over the full band. Accordingly, I tested a black-body plus cutoff power law (BBCPL) model.

Given the success of the basic CPL model at fitting these data, it is perhaps not surprising that the CPL component of the BBCPL model dominates the fits. Figure 4.13c shows that the E_{peak} of the BBCPL fits closely corresponds to the peak energy fit by the Band function. The peak energy of the black-body component alone, however, is almost completely uncorrelated with the peak energy of the phenomenological models (Figures 4.13d–f). This behavior is in marked contrast to the success of the BBPL model of identifying the spectral peak with the black-body peak (Figure 4.13b). Moreover, many of the fit values of kT in the BBCPL model are limits only.[4] With the CPL component providing the curvature and flux

---

[4] In the fits of all models, the 90% C.L. errors of the peak energies–E_{peak} for the Band, CPL, and BBCPL

in the BBCPL model, the BB component weakens and shifts to the limits of the fit band.

The bolometric black-body flux is obtained by integrating the differential energy spectrum of the Planck function EN_E over all energies; it equals $A(kT)^4 E_{piv}^2 \pi^4/15$. Its value is fairly similar for the BBPL and BBCPL models. However, since the best-fit black-body temperature is often near the limits of the RHESSI band, the fraction of the flux in the RHESSI band provided by the black body drops sharply in the BBCPL model (Figure 4.14). The black-body component is accordingly of less relevance in explaining the observed data.

Following Ghirlanda et al. (2007), I also attempted "constrained" fits of the BBCPL model in an attempt to force the black-body component to provide the peak of the spectral emission. I fit a BBCPL model with the black-body peak energy (3.92 kT) constrained to lie within the 90% confidence limit of the best-fit Band E_{peak} value.[5] While the χ^2 of the BBCPL fit is similar to that of the Band fits, as expected the χ^2 value for the constrained BBCPL fits increases dramatically (Figure 4.15). Moreover, the best-fit kT value typically does not have 90% confidence limits within the specified band. The black-body contribution to the total flux in the RHESSI band is not significantly different than for the regular BBCPL model and remains small.

4.4.3 Time Evolution

One of the most notable features of the BATSE BBPL fits presented by RP09 is the remarkably universal behavior of the time evolution obtained in the BBPL fits. For their sample of single-pulse bursts, they found that both the fit black-body temperature and the bolometric black-body flux exhibit a regular power law rise and decay. They found identical break times for the flux and temperature evolution in a given burst. Moreover, a dimensionless proxy for the black-body normalization, $\mathcal{R}(t) \equiv (F_{BB}/\sigma T^4)^{1/2} = 1.01 \times 10^{-16} A^{1/2} E_{piv}^{-1}$, is related to the size of the photospheric emission region and increases monotonically even for bursts with complex light curves.

I consider the time evolution of the black-body components of the RHESSI BBPL and BBCPL fits in an attempt to reproduce these behaviors. Since the RP09 time-evolution results were obtained from bursts with simple single-pulse time profiles, I used a single-pulse burst sample with slightly lower signal-to-noise ratio than my high S/N sample of mostly complex bursts. Unfortunately, only 3 bursts met the selection criteria described in Section 4.2.1. These bursts, GRBs 020715, 030329A, and 060805B, have 8, 12, and 5 subintervals, respectively. Accordingly, caveats of small sample size and limited time resolution apply to my analysis of their time evolution.

I plot the time evolution of the temperature, bolometric black-body flux, and $\mathcal{R}(t)$ in

---

models, and $3.92kT$ for the BBPL and BBCPL models–were required to converge within 70% of the lowest energy of the fit data and 130% of the highest energy. The peak energies are reported as upper or lower limits when the confidence limit did not converge before the lower or upper bound. The convergence behavior was not sensitive to the precise limits chosen.

[5] My approach is less restrictive than that of Ghirlanda et al. (2007), who fixed the black-body peak at E_{peak}.

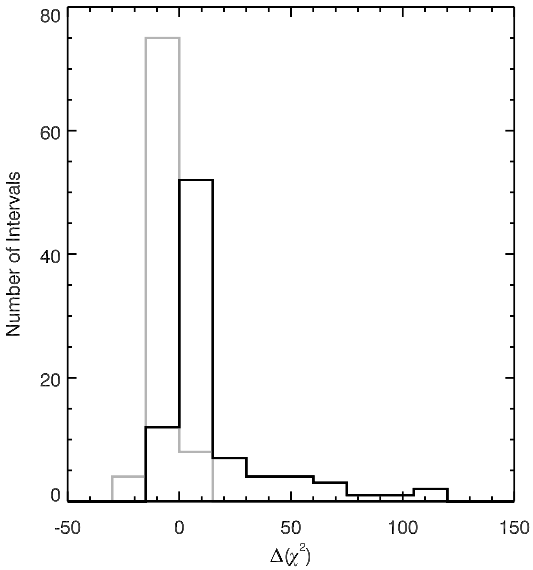

Figure 4.15: Difference in the chi-squared values for fits to the constrained BBCPL and BBCPL models (black). Requiring the black-body peak to lie near the peak of the spectrum causes a major increase in the chi-squared value. The difference in chi-squared for the Band and BBCPL fits (gray) is much smaller. Three outlying histogram bins were omitted for plot clarity.

log-log space in Figures 4.16, 4.17, and 4.18. Within the moderate time resolution of these data, there is a clear suggestion of the correlated power-law rise, break, and decay of the temperature and black-body flux for the BBPL model, as found by RP09.

For these three bursts, the BBPL $\mathcal{R}(t)$ values are generally consistent with a constant value. While a minority of the RP09 sample showed such behavior, far more frequently the RP09 bursts had $\mathcal{R}(t)$ values which increased as a power-law over an order of magnitude. The authors interpreted this increase in terms of the expansion of the photospheric emission region. RP09 also found frequent monotonic increases in $\mathcal{R}$ for bursts with complex lightcurves. My high S/N sample, consisting primarily of bursts with such lightcurves, also all have $\mathcal{R}(t)$ consistent with a constant. The values of $\mathcal{R}$ I obtain are consistent with the RP09 sample, however. Both the single-peak and the high S/N samples range from 7×10^{-20}–2×10^{-18} and peak near 3×10^{-19}.

The time evolution of the BBCPL black body exhibits few clear trends, as expected given the black body's convergence problems and minimal contribution to the fit. For the single-pulse sample, the bolometric black-body flux seems to track that obtained in the BBPL model (Figures 4.16–4.18). There is less correlation between the temperatures of the two models, though, and the time evolution of $\mathcal{R}(t)$ for both the single-pulse sample and the high S/N sample shows little temporal regularity. Moreover, the BBCPL $\mathcal{R}(t)$ value can be more than an order of magnitude different than that obtained in the BBPL fits, ranging from 10^{-23}–10^{-17}. Such changes would imply orders of magnitude change in the inferred size of photospheric emission region, casting further doubt on the physical significance of the black-body component of my BBCPL fits.

4.5 Conclusions

I have systematically tested quasi-thermal spectral models of GRB prompt emission over a broader energy band (30 keV–17 MeV) than considered pre-*Fermi*. Many of the successes of the BBPL model in the BATSE band (acceptable χ^2_ν, physical spectral slopes for the nonthermal component, universal time evolution) are not reproduced consistently in the RHESSI data considered here. I have attempted to construct more realistic quasi-thermal models by combining a black body with a cutoff power-law (BBCPL). However, even using intervals selected for high quality (S/N> 45), the BBCPL model exhibits convergence difficulties within the RHESSI band. More crucially, though, the fit black-body component loses its relevance as the origin of the spectral peak.

Data obtained over an even wider energy band, particularly from *Fermi*-GBM and LAT, could clarify the transitions between thermal and nonthermal emission. Results from GRB 080916C, the first bright long burst observed by both instruments, indicated that a Band function provided good representation of the burst spectrum over the full 8 keV–200 GeV energy range (Abdo et al. 2009b). In a study by Zhang et al. (2010), time-resolved spectra for 14 of 17 GRBs observed by the LAT+GBM through May 2010 were best fit by a simple Band function. In contrast, the *Fermi* LAT+GBM data for GRB 090902B required a high-energy power-law component in addition to the Band function (Abdo et al. 2009a). Ryde et al. (2010) found that the GRB 090902B data, when resolved into sub-second time bins, were also compatible with a new quasi-thermal model. This model retains the simple nonthermal power-law component of the BBPL but introduces a multicolor blackbody, a superposition of Plank functions distributed as a power-law up to a maximum temperature. A more detailed study of this burst by Pe'er et al. (2010) showed that careful physical modeling was required to realistically treat the interaction of the thermal and nonthermal emission. Systematic testing of quasi-thermal models with data from multiple bursts, detailed model comparisons, and careful physical modeling will all be needed to draw reliable conclusions about the emission mechanisms of GRBs.

The challenges of untangling the origins of the prompt GRB emission from the prompt gamma-rays alone are long-standing. New observations of higher energy gamma-rays by *Fermi*-LAT, of simultaneous long-wavelength emission by transient monitoring campaigns, and of gamma-ray polarization by Compton telescopes will enrich our view of the prompt emission and provide new clues to its origin.

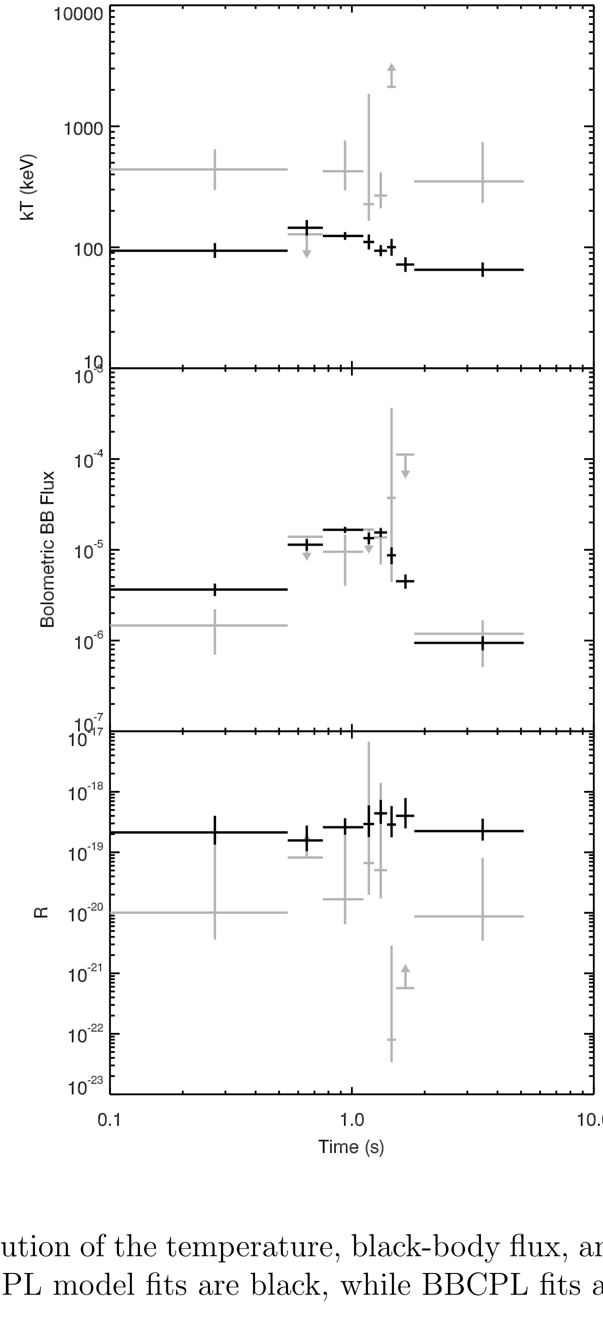

Figure 4.16: Time evolution of the temperature, black-body flux, and $\mathcal{R}$ for the single-pulse burst GRB 020715. BBPL model fits are black, while BBCPL fits are gray.

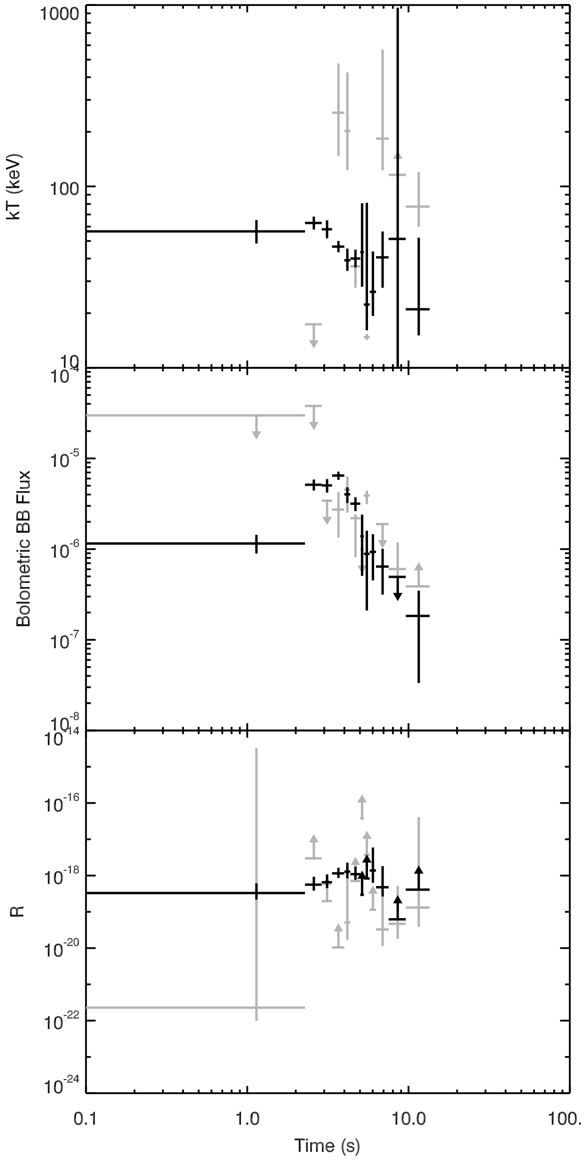

Figure 4.17: Data for the single-pulse burst GRB 030329. Symbols as in Fig. 4.16.

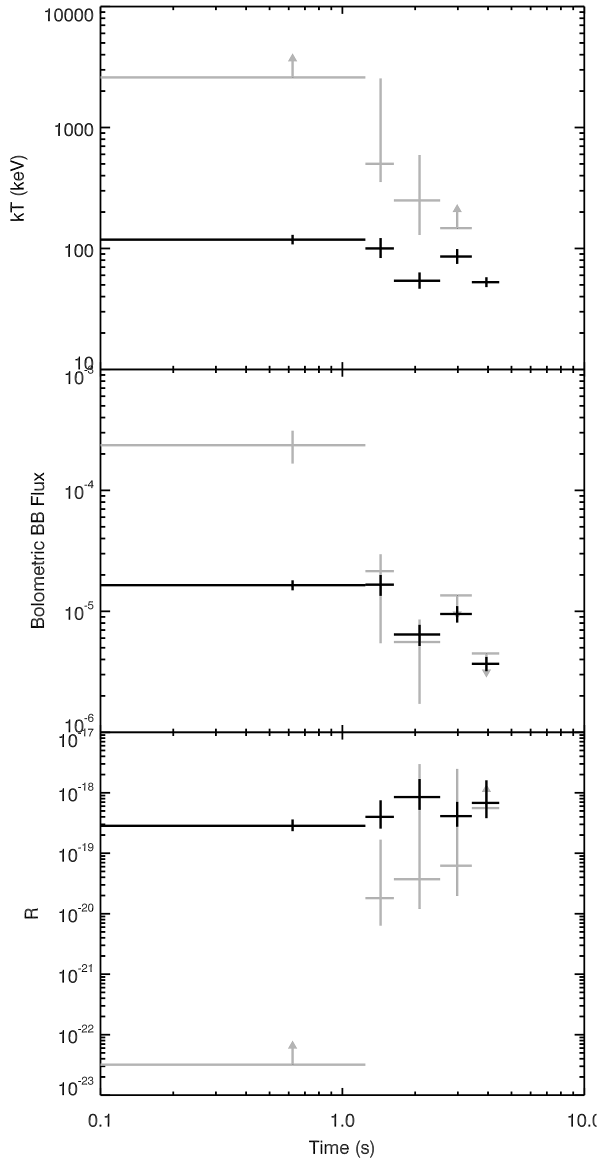

Figure 4.18: Data for the single-pulse burst GRB 060805. Symbols as in Fig. 4.16.

Chapter 5

Overview of the Nuclear Compton Telescope

Abstract

The Nuclear Compton Telescope (NCT) is a balloon-borne Compton telescope. It uses planar germanium strip detectors for soft gamma-ray imaging and spectroscopy (0.2–10 MeV) and polarimetry (0.2–2.0 MeV). I discuss the Compton imaging principle used by NCT, describe the instrument and its flight history, and detail the analysis methods needed to reduce its data.

5.1 Compton Telescopes

The MeV gamma-ray band is scientifically rich but observationally challenging. Astrophysical sources emitting in the soft gamma-ray regime include nuclear lines from Galactic nucleosynthesis (e.g., ^{26}Al, 1.809 MeV; ^{60}Fe, 1.173 and 1.332 MeV; ^{44}Ti, 1.157 MeV), the 511 keV positron annihilation emission at the Galactic Center, gamma-ray bursts (GRBs), soft gamma repeaters (SGRs), pulsars and other compact objects, and active galactic nuclei (AGN). However, atmospheric absorption requires gamma-ray telescopes be flown on stratospheric balloons or satellites. Additionally, high background rates of photons, charged particles, and induced radioactivity limit sensitivity (Dean et al. 2003).

Prior and current observations of the gamma-ray sky have used several non-focusing imaging approaches. The earliest instruments did not image at all, but used collimated on-off observations to measure source and background count rates (e.g., the HEAO-1 A-4 and HEAO-3 C-1 instruments; Matteson 1978; Mahoney et al. 1980). Later instruments were indirect imagers, which use passive material to occult the source flux in characteristic patterns which can be deconvolved into an image. Indirect imaging methods which have been utilized include rotation modulation collimators (RMCs), as on RHESSI (Hurford et al.

2002), and coded aperture masks, as on *Swift*-BAT (Barthelmy et al. 2005). However, since the image reconstruction includes background from all photons detected by the instrument, these indirect approaches are intrinsically less sensitive than those which image the photons directly[1].

Compton imaging is a direct imaging method[2]. Compton telescopes use the Compton scatter formula to reconstruct the direction of an individual observed photon to an annulus on the sky. In the simplest scenario, a photon with an initial energy of E_0 scatters by an angle θ in one detector and is absorbed in a second detector (Figure 5.1). According to the Compton formula (Compton 1923), the scattered photon will have an energy E':

$$E' = \frac{E_0}{1 + \frac{E_0}{m_e c^2}(1 - \cos\theta)} \tag{5.1}$$

By recording the energy of the scattered photon E' as well as the energy deposited in the recoil electron $E_e = E_0 - E'$, a Compton telescope can determine the scattering angle θ. The geometric positions of the scattering and absorption events then localize the photon to an annulus on the sky.

Telescopes which track the recoil electron from the first Compton scatter may further constrain the source photon to an arc, with concomitant improvement in sensitivity. Compton instruments are effective in the MeV band, where Compton scattering is the dominant photon interaction (Figure 2.6).

The Klein-Nishina scattering cross section (Equation 7.1) varies in azimuth relative to the direction of the electric field vector. Accordingly, polarized sources will produce a characteristic modulation pattern in the observed azimuthal scatter angle distribution (ASAD; Section 7.1). The magnitude of this modulation and the location of its maxima can be used to infer the polarization strength and angle of the source, making Compton telescopes intrinsic polarimeters.

Historically, Compton telescopes have employed two primary configurations and a wide variety of detector materials. The first generation of Compton telescopes, typified by COMPTEL (Schönfelder et al. 1993) on the Compton Gamma-Ray Observatory, used two widely-separated detector planes (Figure 5.2). The first, a low-Z converter, scattered the incident gamma-ray. The second plane, a high-Z absorber, absorbed the scattered gamma-ray. Time-of-flight data distinguished physical events from chance coincidences and upward-going pho-

---

[1] The best sensitivity would be provided by focusing optics, as the effective area of the telescope would then be set by the lens rather than the detector plane. Laue lenses provide one prospect for gamma-ray optics. They use Bragg scattering in mosaic crystals to focus gamma-rays, albeit with a narrow bandpass and small field of view. Balloon instruments (Halloin et al. 2003; von Ballmoos et al. 2005) and satellite concepts (Knödlseder et al. 2009; Boggs et al. 2010) using Laue lenses for science observations are in development. Another focusing concept using Fresnel zone plates has been discussed (Skinner 2001, 2010). Such lenses require extremely long focal lengths (10^6 km) unlikely to be practical in the near term, although microarcsecond angular resolution is theoretically possible. Deviations from ideal designs could reduce focal lengths to hundreds of km (Skinner 2002).

[2] Pair telescopes, such as *Fermi*-LAT (Atwood et al. 2009), are also direct imagers. They are effective at tens of MeV and above, where the pair production cross section becomes significant (Figure 2.6)

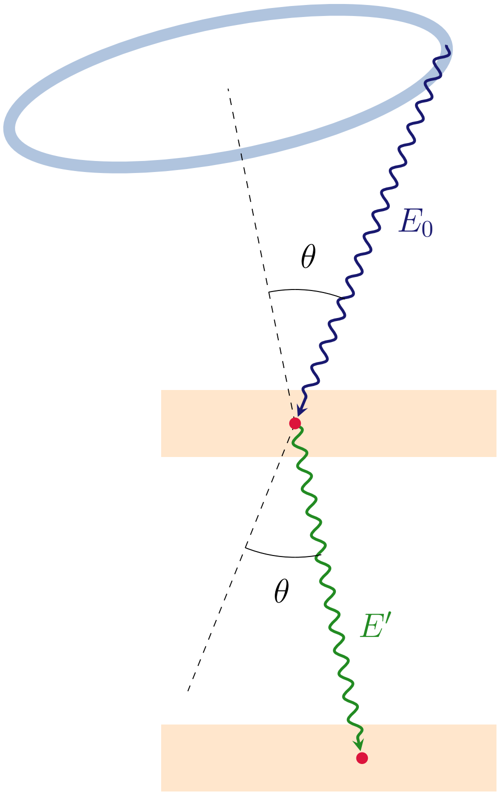

Figure 5.1: The Compton imaging principle, illustrated for a classical COMPTEL-type telescope. The photon scatters in the first detector plane before being absorbed in the second.

tons. This configuration enabled pioneering maps of Galactic ^{26}Al (Diehl et al. 1995; Plüschke et al. 2001), detection of ^{44}Ti from supernova remnants (Iyudin et al. 1994, 1998), and a significant source catalog (Schönfelder et al. 2000). However, due to the large separation of detector planes it suffered from a narrow field of view (40–60° FWHM, depending on energy and event cuts) and extremely low efficiency ($A_{eff} \lesssim 10$ cm^2) (Schönfelder et al. 1993). Moreover, shallow scattering angles led to poor polarimetric sensitivity.

Next-generation Compton telescopes have been designed using a "compact" geometry. In this configuration, the instrument contains multiple closely-packed detector planes, yielding a wide field of view and greater efficiency, as a larger proportion of scattered photons are absorbed in the active detector volume. Additionally, multiple scattering events are possible before the final photo-absorption. Instead of using time-of-flight data to determine the order of interactions, the event reconstruction process determines the optimal ordering of events satisfying the Compton kinematics (Boggs & Jean 2000).

Several balloon and laboratory instruments have developed the compact Compton telescope concept. Some have retained the scatter/absorber concept of classical Compton

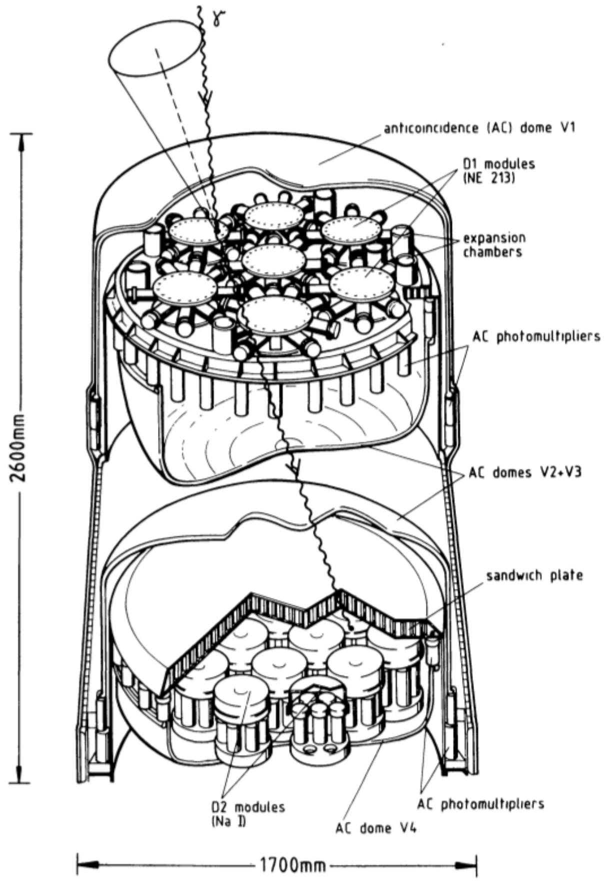

Figure 5.2: Schematic of Compton imaging with COMPTEL (Figure 2 of Schönfelder et al. 1993).

telescopes by using multiple detector materials, typically silicon trackers and a scintillator calorimeter. Instruments of this type include MEGA (Bloser et al. 2002; Kanbach et al. 2004) and TIGRE (Bhattacharya et al. 1999), and their use of silicon trackers enables measurement of the direction of the recoil electron. Other instruments have used homogeneous detector volumes, simplifying the instrument and potentially increasing the field of view. LXeGRIT (Aprile et al. 1996; Curioni et al. 2007) used liquid xenon to provide a large sensitive volume in its time projection chamber. The Nuclear Compton Telescope (NCT), described here, uses closely packed germanium strip detectors (Figure 5.3). Germanium has unsurpassed spectral resolution, which is optimal for studies of line emission, and germanium crystals can be fabricated in large sizes. However, germanium detectors require cryogenic cooling, and germanium has higher Doppler broadening than silicon, decreasing its theoretical best achievable angular resolution (Zoglauer & Kanbach 2003).

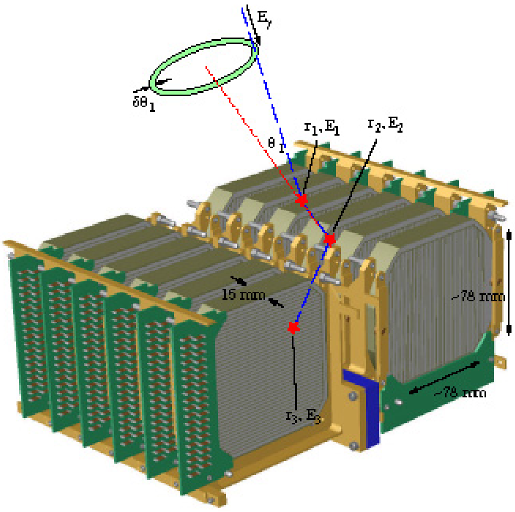

Figure 5.3: Schematic of Compton imaging with NCT showing the reconstruction of a 3-site event (Figure 1 of Boggs et al. 2003).

5.2 The NCT Detectors

NCT uses planar high-purity germanium cross-strip detectors to image gamma-rays. Each germanium detector is 8 × 8 × 1.5 cm. There are 37 aluminum strips deposited on each face; the strips are oriented orthogonally to provide 2D x and y positions for interactions within the detector volume (Figure 5.4). The charge collection time difference (CTD) between the two faces determines the depth of interaction z (Amman & Luke 2000; Amrose et al. 2003; Coburn et al. 2003; Bandstra et al. 2006) to 0.5–0.8 mm (Chiu et al. 2009). The strips have a 2.0 mm pitch and a 0.25 mm gap between each strip. The 3D localization of events is accordingly 2 mm^3, which is dominated by the strip width. A 2.0 mm instrumented guard ring around the edge of the detector provides veto signals.

The detectors are processed by Lawrence Berkeley National Laboratory (LBNL) from ORTEC crystals. Seven of the current ten NCT detectors use amorphous germanium (Luke et al. 1992) bipolar blocking contacts; the remaining three use amorphous silicon cathodes to improve their performance after thermal cycling (Amman et al. 2007). In both cases, the thin ($\sim$ 0.1 micron) layer of amorphous semiconductor deposited over the entire detector passivates the surface. The aluminum strips are evaporated onto the amorphous layer and provide electrical contacts.

The ten NCT detectors are mounted on a common coldfinger (Figure 5.5) and cooled to 85 K by liquid nitrogen. The 50 L tank capacity provides 7–8 days of cooling. During flight, the tank is capped with a 5 psi valve to keep the LN2 pressurized; a solenoid assembly operable by remote command enables depressurization if required.

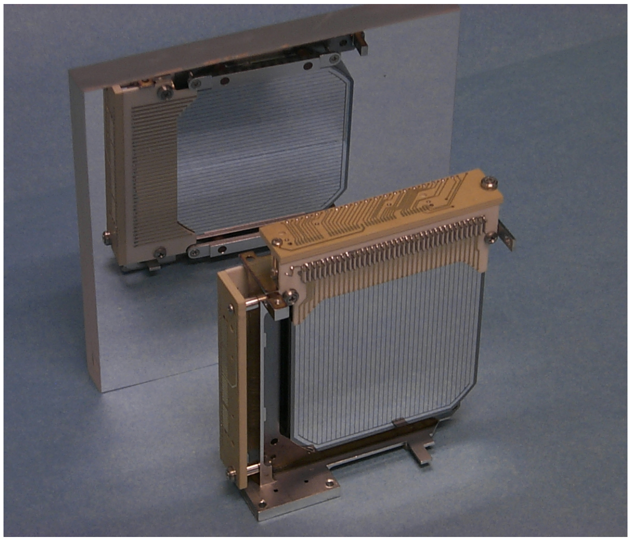

Figure 5.4: Image of an NCT detector showing the orthogonal horizontal and vertical strips (Figure 3 of Bandstra et al. 2009).

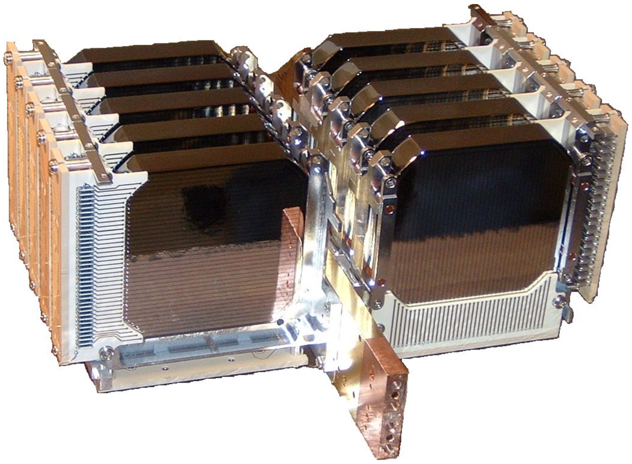

Figure 5.5: The ten NCT detectors mounted on the dewar coldfinger.

5.3 Instrumentation

The NCT detectors are instrumented by conventional signal-processing electronics (Coburn et al. 2004). Two low-power charge-sensitive preamplifiers (Fabris et al. 1999) obtain signals from each detector. To minimize complexity and weight, the signals are carried from the preamps to the electronics bay by coaxial ribbon cables. Signals from each detector are processed by a "card cage" containing printed circuit boards implementing the pulse-shaping amplifiers, digital signal processing logic, and low- and high-voltage power supplies. Signals from each strip are passed to fast and slow pulse-shaping channels to generate timing and energy values. A bipolar shaper in the fast channel time-stamps the data at the signal zero-crossing. The slow channel uses a 6 μs time-to-peak unipolar shaper; the signal is then passed through a peak detect and stretch function.

Eight "analog boards" of ten channels each are required to instrument one detector. The analog boards pass information through the card cage backplane to a DSP board (Hung et al. 2009) that provides the trigger logic, generates housekeeping data, and maintains the Ethernet command and data link to the flight computer.

5.4 Gondola Systems

NCT is carried on a balloon gondola (Figure 5.6) originally used by the HIREGS instrument (Pelling et al. 1992; Boggs et al. 1998). The cryostat, dewar, and shields are held in an instrument cradle (Figure 5.7) in the front of the gondola protected by roll bars. The tilt of the cradle can be adjusted for each campaign to optimize sensitivity for the chosen observing plan. The flight computer, card cages, batteries, and other electronics reside within an insulated electronics bay (Figure 5.8) at the rear of the gondola. The CSBF SIP communications package is held below the gondola and protected by a metal cage.

To reduce the background, particularly from albedo photons, the NCT cryostat is surrounded by a well of 5 cm bismuth germanate (BGO) active shielding (Figure 5.7). Shield vetoes are the dominant source of instrument dead time (8%).

NCT's broad field of view and moderate angular resolution yield relatively modest pointing requirements: several degree pointing accuracy, and aspect reconstruction to half a degree or better. During flight, the instrument cradle is held at fixed elevation, while a rotor assembly turns the gondola in azimuth. A dual-axis pointing magnetometer feeds into a nulling servo loop to orient the gondola relative to the local magnetic field. The flight computer achieves absolute pointing by using a magnetic field model[3] to determine the local magnetic declination (the offset between true and magnetic north) and adjusting the pointing magnetometer to obtain the desired orientation. A Magellan ADU5 differential GPS system provides real-time location and attitude data at 1 Hz for post-flight aspect determination. A three-axis magnetometer and accelerometer provides redundant aspect information.

---

[3] The World Magnetic Model, `http://www.ngdc.noaa.gov/geomag/WMM/DoDWMM.shtml`

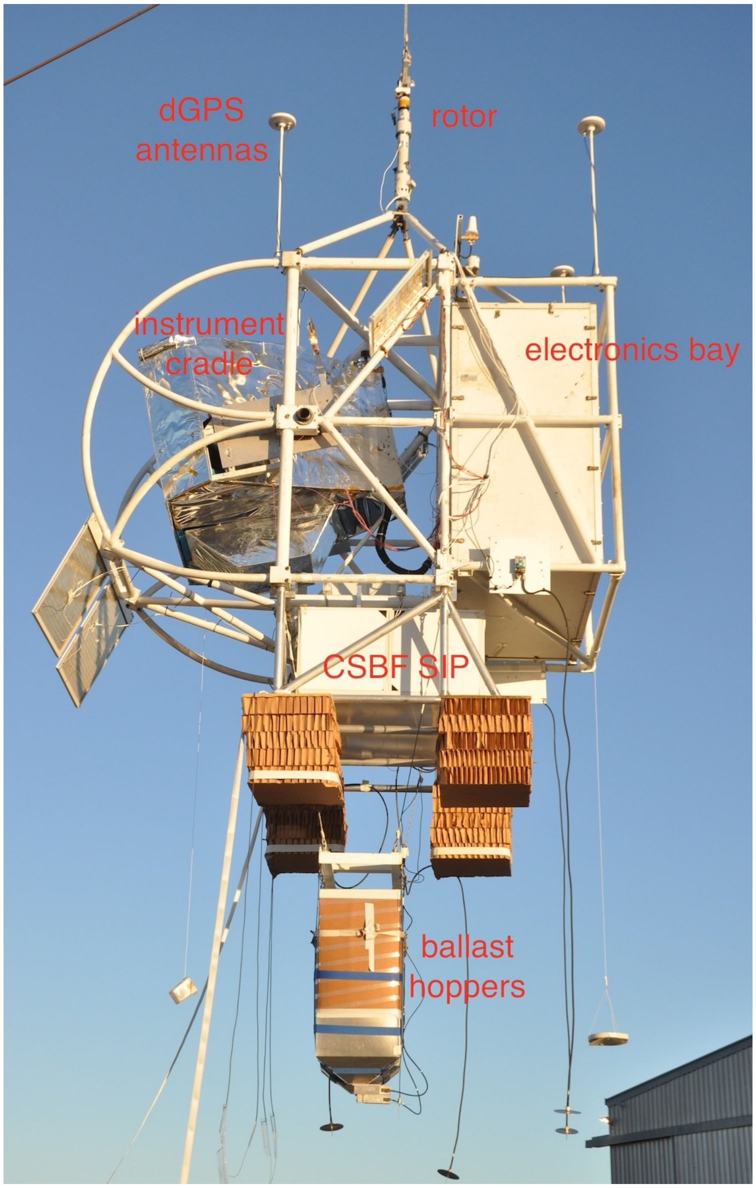

Figure 5.6: The NCT gondola as configured in 2010.

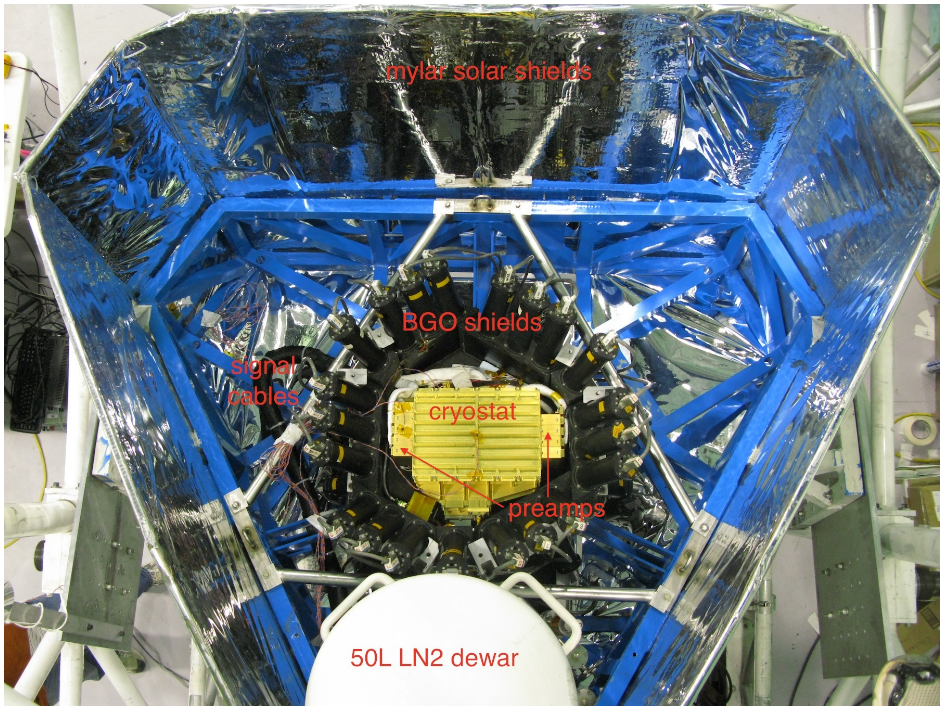

Figure 5.7: The NCT instrument cradle in 2010.

For short (1–4 day) conventional balloon flights, NCT may be powered by batteries alone. In preparation for potential Long Duration Balloon Flights (LDBFs) lasting 1–3 weeks, for the 2009 campaign NCT used large solar panels to recharge the on-board batteries powering the instrument.

The NCT flight computer communicates with and commands the card cages, executes the pointing plan, handles commands and telemetry from the ground, and stores data to disk. The flight software boots from a 4 GB CompactFlash card and runs on a 1.4 GHz single-board computer. The multithreaded flight software, derived from that of HIREGS, is written in C and runs under Linux. Data are archived to redundant 64 GB solid state drives and telemetered to the ground via a line-of-sight UHF link at 384 kbps.

5.5 Flight History

NCT has participated in three mid-latitude balloon campaigns, flying twice. A two-detector prototype of NCT flew on June 1, 2005, from the NASA Columbia Scientific Ballooning Facility (CSBF) location at Ft. Sumner, New Mexico (Coburn et al. 2005; Boggs et al. 2006a). The 6-hour flight allowed detailed characterization of the background at float altitudes (Figure 5.9; Bowen et al. 2007) despite a failure of a servo system in the azimuthal pointing system.

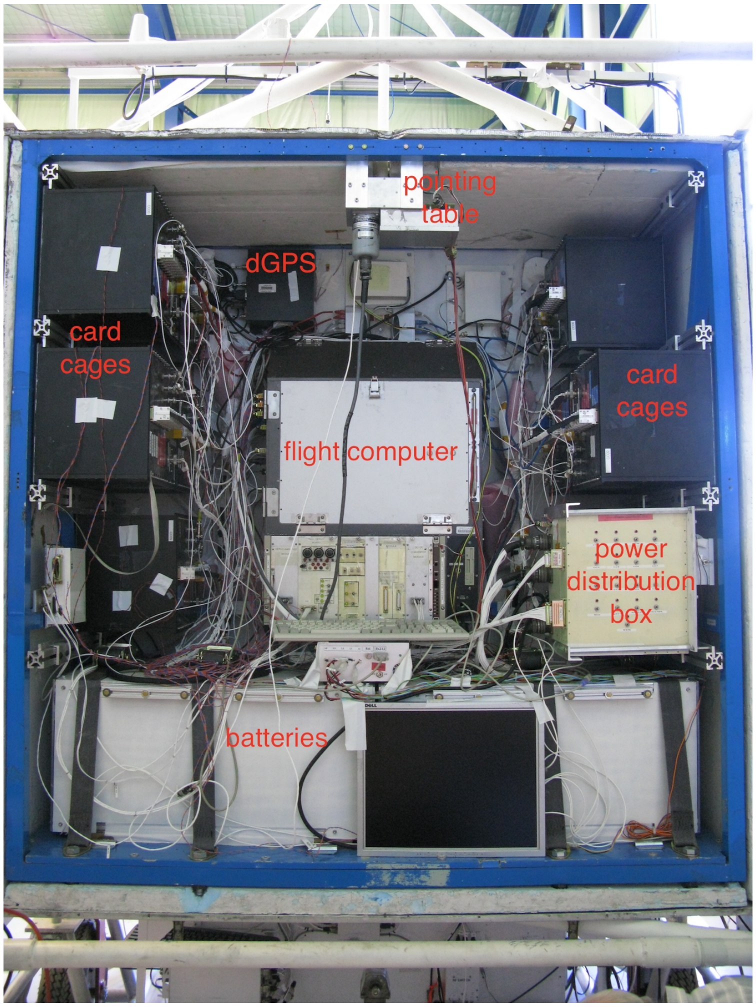

Figure 5.8: The NCT electronics bay as configured in 2010.

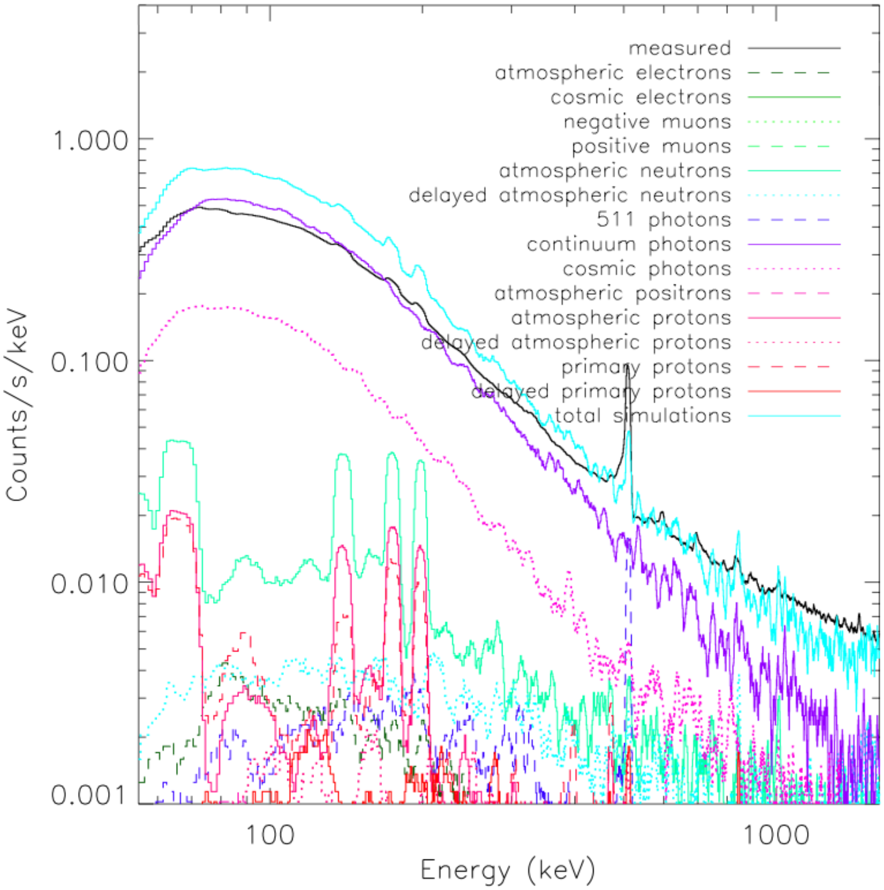

Figure 5.9: Comparison of observed background data to simulations for the 2005 NCT prototype flight (Figure 13 of Bowen et al. 2007).

NCT flew again from Ft. Sumner on May 17–18, 2009 (Bandstra et al. 2009) with ten detectors and updated electronics (Bellm et al. 2009). The total flight time was 38.5 hours; malfunctions in the solar panels limited science observations to 22 hours. A problem with the strain gauges in the rotor torque bridge made reliable pointing difficult, compromising source exposure. However, the data collected were sufficient to image the Crab Nebula with 4.0σ significance (Figure 5.10; Bandstra 2010).

In 2010, NCT participated in the CSBF balloon campaign in Alice Springs, Australia. The major science goal of the campaign was detection of the 511 keV positron emission from the Galactic Center. However, a launch mishap on April 29, 2010 due to the failure of the CSBF gondola release mechanism (NASA 2010) caused extensive damage to the NCT systems (Bellm et al. 2010). While the gondola and aspect systems were completely destroyed, the detectors and readout electronics suffered only minor damage. Reconstruction efforts are ongoing. Calibration data obtained before the launch attempt were valuable in characterizing NCT's response over a wider energy band (Chapter 6).

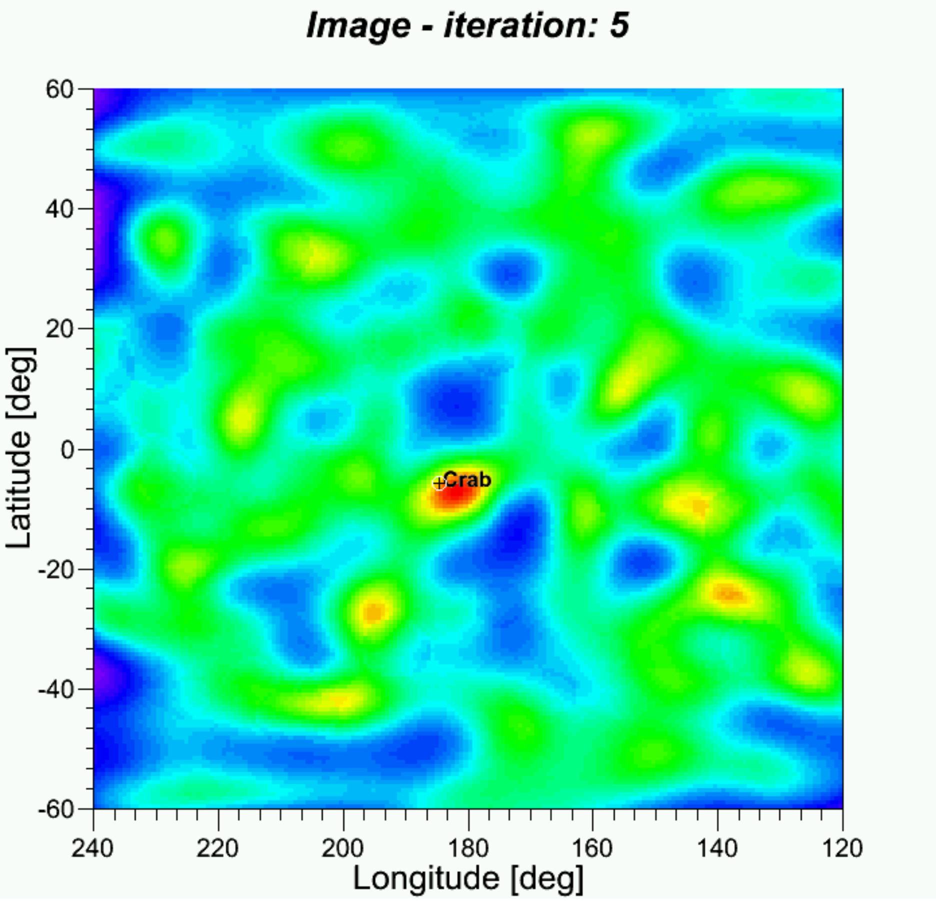

Figure 5.10: NCT image of the Crab Nebula from the 2009 flight (Bandstra 2010). The image, from 25 ks of data, uses 2-site events from 200–1500 keV. There are 49,000 photons in the backprojection, of which 700 are expected from the Crab. Five iterations of the MLEM algorithm were applied to the image (Section 5.6).

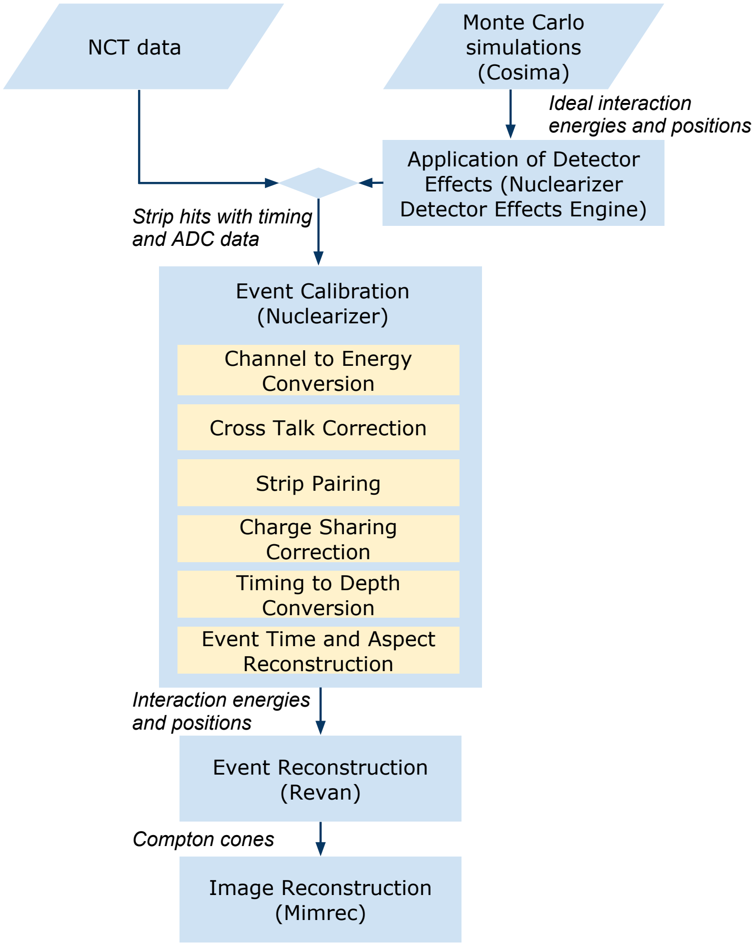

Figure 5.11: Flowchart showing the steps to analyze NCT data (adapted from Figure 3.9 of Bandstra 2010). The Detector Effects Engine enables identical reduction procedures for real and simulated data.

5.6 Analysis Methods

Analysis of the NCT data requires several stages (Figure 5.11). The MEGAlib software package (Zoglauer et al. 2004a, 2006) provides a common framework for the reduction.

The raw NCT data from each detector consist of x and y strip hits, the charge collection time difference, and the event time tagged by the 10 MHz clock. A modular NCT-specific routine built on the MEGAlib library, Nuclearizer, converts these raw data into physical interactions with energies, positions, and absolute time. The software applies the results obtained from energy calibrations with radioisotopes of varying energies (Chiu et al. 2009), using a nonlinear (power law plus Gaussian) model to convert analog-to-digital converter (ADC) channels to energies (Bandstra 2010). Nuclearizer corrects for electronic cross-talk

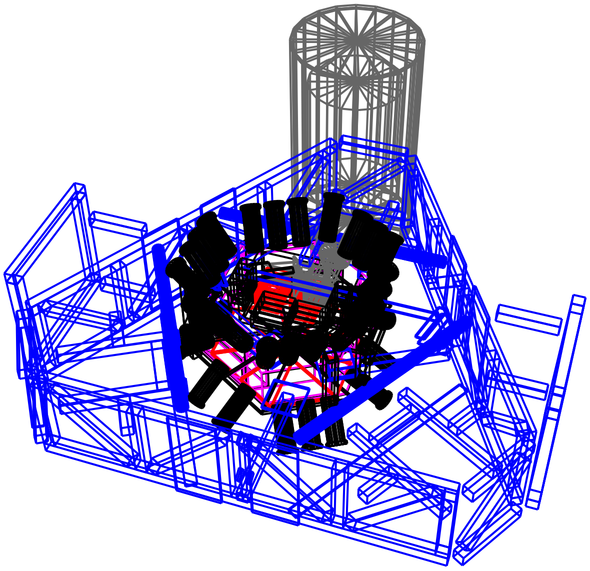

Figure 5.12: The NCT mass model.

observed when adjacent strips trigger (Liu et al. 2009; Bandstra 2010). The software determines the best pairing of strip hits into interactions with x and y positions, then accounts for charge sharing between the strips (Bandstra 2010). Finally, Nuclearizer applies the conversion of CTD to depth of interaction z obtained from calibrations (Bandstra et al. 2006; Chiu et al. 2009).

Cross-checks with Monte Carlo simulations are vital for verifying laboratory and flight results. The NCT tools provide a method for straightforward comparison of Monte Carlo results to observed data. The GEANT4-based (Allison et al. 2006) simulation tool Cosima in MEGAlib provides a capable and flexible simulation environment well-integrated in the analysis framework. Our group has produced a detailed mass model of NCT for use in the simulations (Figure 5.12). To assure the most realistic comparison with real data, a module in Nuclearizer converts the precise positions and energies generated by the Monte Carlo simulation into the form of raw NCT data (strip hits, ADC channels, and CTD) by inverting the calibration routines and applying detector effects like charge sharing between strips. The rest of the analysis chain then processes these simulated hits in the same manner as real NCT data.

Nuclearizer generates a list of interactions with physical positions and energies. The next program in the analysis chain, MEGAlib's Revan, determines the most probable interaction sequence for coincident events. Typically, NCT analysis uses a χ^2 approach (Boggs & Jean 2000) which compares the scatter angles implied by the energy deposits to the geometric angles determined by the physical positions for a given interaction ordering. The best ordering minimizes the difference between the implied Compton scatter angles and the geometric angles between the sites. Bayesian approaches to event reconstruction are also possible (Zoglauer et al. 2007). The output of Revan are Compton cones: with the event ordering determined, the first and second interaction localize the photon to an annulus on the sky.

The final stage of NCT analysis uses the MEGAlib package Mimrec. Mimrec performs Compton imaging, backprojecting the Compton cones in 2D or 3D coordinate systems and applying list-mode maximum-likelihood expectation maximization (MLEM) (Wilderman et al. 1998; Zoglauer 2005) to reconstruct the backprojected image. Additionally, Mimrec performs event selections and can extract energy spectra, determine angular resolution, perform polarimetric analysis, and generate other distribution and quality metrics.

5.7 Summary

NCT is a balloon-borne Compton telescope with a compact detector geometry that provides high efficiency and a wide field of view in the soft gamma-ray band. The NCT detectors are planar cross-strip germanium detectors with excellent energy resolution and good uniformity. NCT's data analysis methods employ the mature MEGAlib toolkit, and the methods have been validated with results from calibration data and Monte Carlo simulations. NCT is a flight-proven instrument; in two stratospheric balloon flights from New Mexico, NCT has performed a detailed measurement of the background at float altitudes and imaged the Crab Nebula.

Chapter 6

Effective Area Calibration of the Nuclear Compton Telescope

Abstract

Instrumental calibrations with radioactive sources are necessary to quantify performance, confirm analysis methods, and validate science results. I present results of high-level calibrations of NCT's effective area and compare them to Monte Carlo simulations. Simulation-derived values are a factor of 1.5–2.0 larger than those obtained from the calibration data; this offset may be due to imperfect event calibrations.

6.1 Overview

Effective area (A_{eff}) is used to specify the efficiency of X-ray and gamma-ray telescopes. It identically relates the number of detected counts N_{det} from a known source flux F [photons cm^{-2} s^{-1}] over an integration time Δt:

$$A_{\text{eff}} \equiv \frac{N_{det}}{F \Delta t}. \tag{6.1}$$

The units of A_{eff} are [cm^2 counts photon^{-1}]. For a mono-energetic point source of activity r_{decay} [Bq] at distance d from the detector,

$$A_{\text{eff}} = \frac{N_{det} 4 \pi d^2}{r_{decay} \Delta t}. \tag{6.2}$$

The uncertainty σ_A of the effective area is thus

$$\sigma_A = A_{\text{eff}} \sqrt{\left(\frac{1}{N_{det}}\right) + \left(\frac{\sigma_r}{r_{decay}}\right)^2 + \left(\frac{\sigma_{\Delta t}}{\Delta t}\right)^2 + 4\left(\frac{\sigma_d}{d}\right)^2}. \tag{6.3}$$

Radioisotope	Primary spectral lines (keV)	Activity (μCi, 1/1/2010)
^{133}Ba	356.0	145.9 (Aus.)
^{137}Cs	661.7	76.0 (NM), 68.6 (Aus.)
^{60}Co	1173.2, 1332.5	22.7 (NM), 22.0 (Aus.)
^{88}Y	1836.1	165.3 (Aus.)

Table 6.1: Calibration sources used for this work during the New Mexico (NM) and Australian (Aus) campaigns. All New Mexico sources have 3.1% activity uncertainty (99% C.L.), while all Australian sources have 3.0% uncertainty.

Effective area typically varies throughout the field of view as a function of detection energy band and event cuts.

6.2 Experimental Setup

To calibrate the NCT detectors, the NCT team placed radioactive sources of known activity (Table 6.1) at target calibration points throughout the NCT field of view. The source distances, typically 4–5 m from the detectors, were a compromise between minimizing the observation time and ensuring that the sources were in the far-field of the instrument. (In practice, the logistics of the hangars where the calibrations took place enforced the source–detector distances used.) These distances gave acceptable numbers of counts over a two-hour integration time. The deviation of the photons from parallel at the detector was much less than the angular resolution of the telescope: $\theta \sim d/L \lesssim 1.5^\circ$, where L is the half-width of the telescope, ~ 10 cm.

The 99% C.L. uncertainties in the source activities are $\sim 3.1\%$ (Table 6.1), so $\sigma_r \approx 1.2\%$. For σ_r to be the dominant contribution to the error in A_{eff}, the other components of σ_A (Equation 6.3) must be smaller by a factor ξ. For definiteness, I choose $\xi = 0.1$. This prescription gives the following constraints on the experimental setup:

- $\sigma_{\Delta t} < 27$ seconds for a 2 hour exposure—easily achieved by a two-hour timer on the data acquisition program. However, the ∼2% deadtime of the card cages must be accounted for (Figure 6.1).
- $\sigma_d < 0.76$ cm for $d = 4.0$ m—the theodolite position reconstruction described below achieves localizations near this accuracy (Figure 6.4).
- $N_{det} > 69,000$ counts—not practical for the relatively weak sources used here, so Poisson errors contribute appreciably to the total effective area uncertainty.

Accordingly, calculations of σ_A presented here include contributions from σ_r, N_{det}, and the (generally negligible) σ_d.

To position sources during calibration, we used a 30 in. × 40. in. aluminum sheet with a grid of punched holes. A machined acrylic clamp screwed into the center of this “source

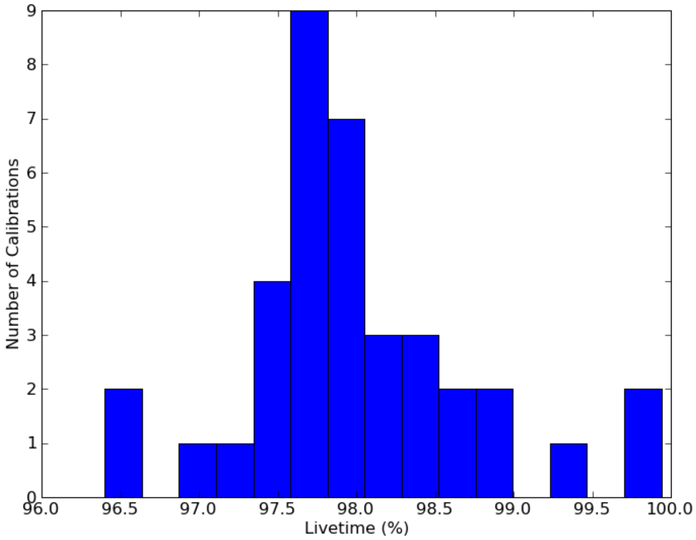

Figure 6.1: Distribution of average livetime for the effective area calibration data.

board", securing the source in place and precisely registering its position. An overhead hoist lifted the source board to the appropriate height. We moved the gondola into position for the target source angle, using a laser angle finder to aid in positioning. Figure 6.2 shows the completed laboratory setup.

To reconstruct the position of the source relative to the detectors, we used a Sokkisha TM6 theodolite with 6 arcsecond direct reading accuracy in both the vertical and horizontal angles. For each calibration, we measured the angles to four sight points at the corners of the source board as well as four corners of the cryostat. We also measured baselines to one reference corner of each using plumb bobs to determine their vertical height and horizontal distance from the theodolite axis.

Given the known sizes of the source board and the cryostat, the baselines and angles determine the 3D positions of each in the frame of the theodolite. Appropriate transformations give the source position in the coordinate system centered on the cryostat used by the NCT mass model. A numerical bootstrap which perturbs the measured readings in angle and distance using the estimated uncertainties provides error estimates for all the derived quantities. Figure 6.3 shows the source localization distribution for one of the calibrations, while Figure 6.4 shows the distribution of distance localization uncertainties for all measurements.

6.3 Data Analysis

Using the theodolite-derived positions, I generated Cosima Monte Carlo simulations corresponding to each calibration run. I reduced the data and simulations using the methods

Figure 6.2: Laboratory setup for effective area calibrations.

described in Section 5.6; Table 6.2 describes the event cuts I employed.

I used an automated procedure to fit a Gaussian function to the reconstructed photopeak for each calibration line. Table 6.3 presents examples of these fits. Figure 6.5 shows the fit FWHM energy resolutions generated by this procedure, and Figure 6.6 shows the effective area throughout the field of view obtained by selecting Compton events within $\pm 2\sigma$ of the fit photopeak.

Including cuts on the direction of the incoming photon is required to derive a measure of the effective area relevant for astrophysical observations, particularly of point sources. I reconstructed images of the calibration data and simulations and determined the source positions in spherical coordinates from the maximum image value. I extracted ARM[1] histograms for each line and fit them with an asymmetric Gaussian plus Lorentzian function (Table 6.4). Figure 6.7 shows the resulting ARM values, and Figure 6.8 gives the effective area using both the photopeak energy and ARM cuts.

---

[1] The Angular Resolution Measure is defined for each Compton cone as the shortest angular distance between the cone and the assumed true origin of the photons.

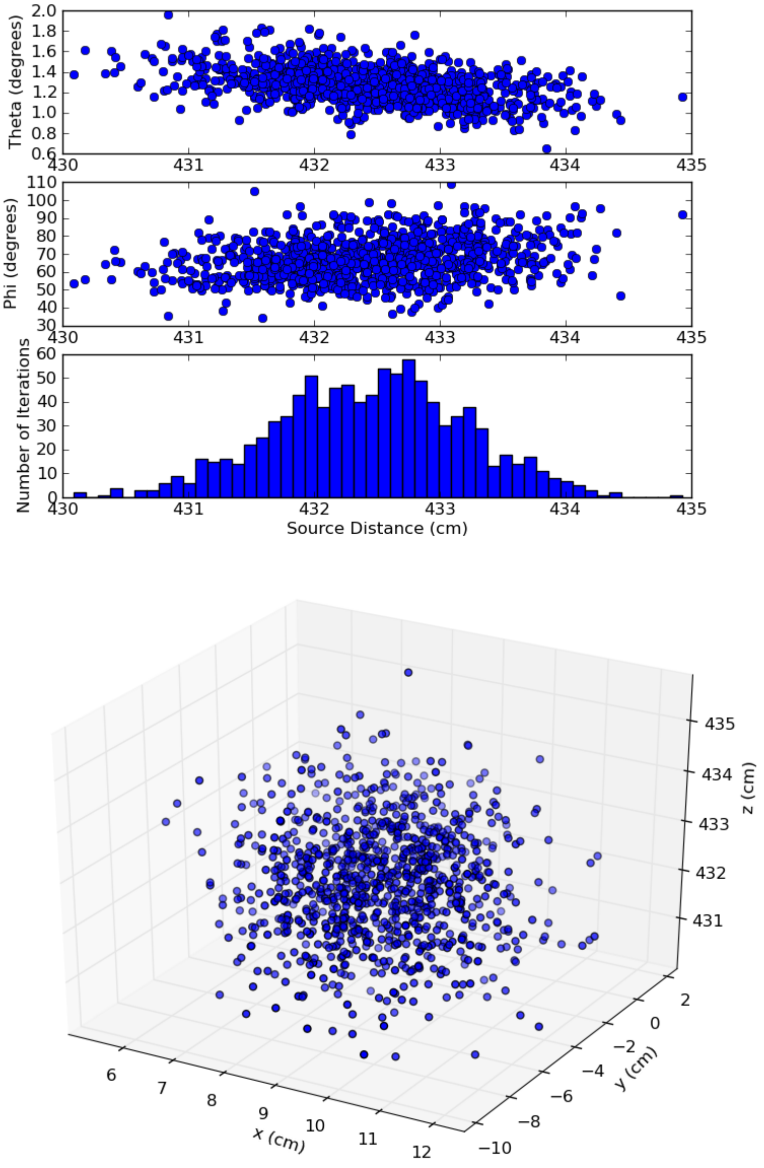

Figure 6.3: Example of theodolite localization in spherical (top) and Cartesian (bottom) coordinates for a calibration source located nearly on-axis. A numerical bootstrap produces the observed spread.

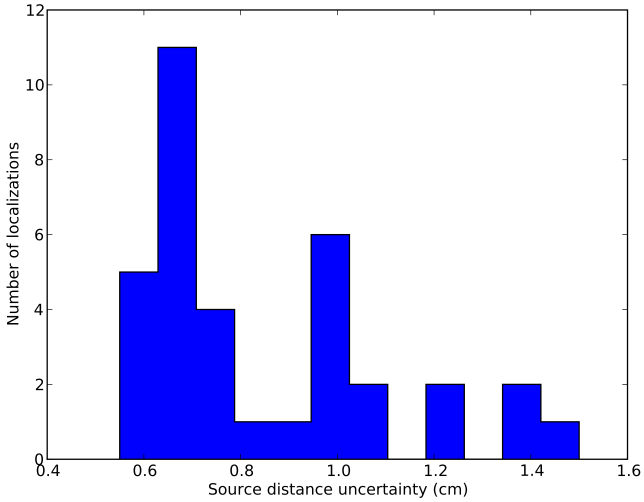

Figure 6.4: Uncertainties (1σ) in the source–detector distance derived from the theodolite measurements.

Parameter	Allowed Range
Photon Energy	$\pm 2\sigma$ from fit photopeak
ARM (optional)	$\pm 2\times$ fit FWHM
Number of Interactions	2–7
Compton scatter Angle (θ)	any
Distance between first two interactions	1–20 cm
Distance between other interactions	any
Compton Quality Factor	0–1

Table 6.2: Event cuts used for the effective area analysis.

Energy (keV)	Data	Simulation
356	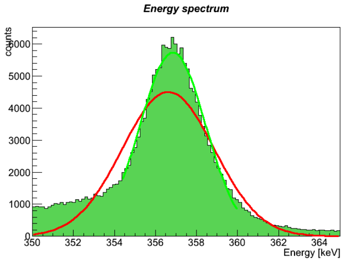	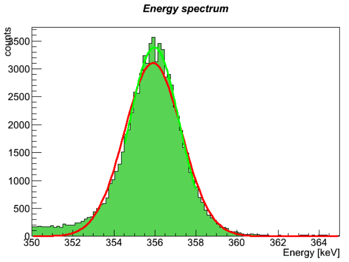
662	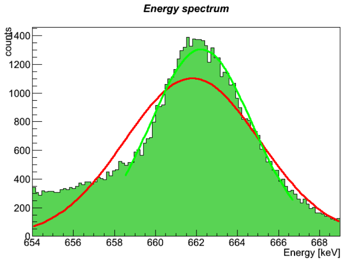	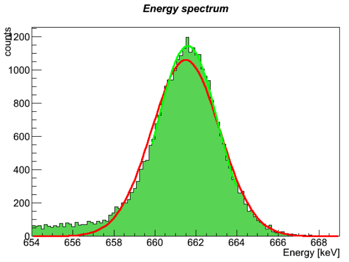
1173	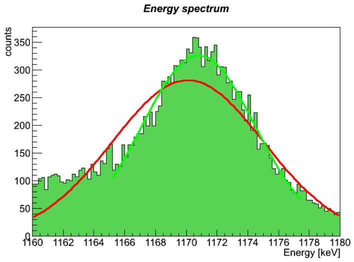	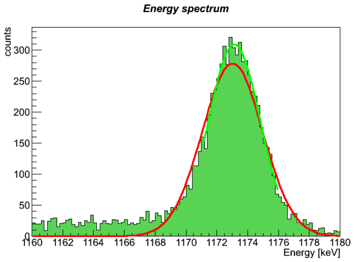
1333	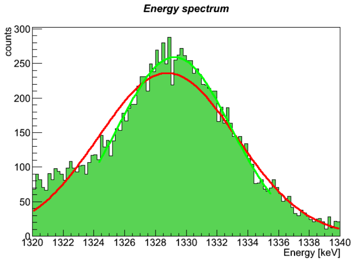	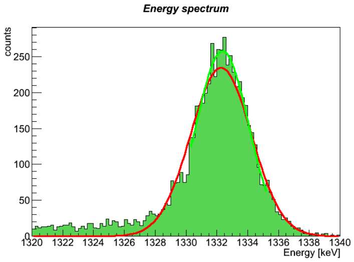
1836	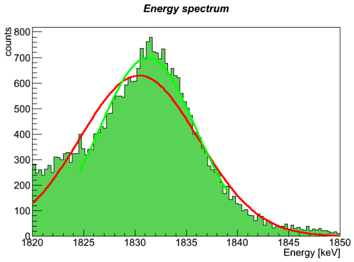	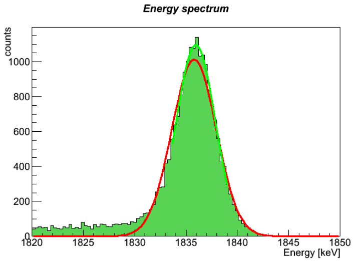

Table 6.3: Example Gaussian fits of the data and simulation photopeaks, using the on-axis 2010 data. Preliminary fits (red lines) provided the initial conditions for the final fits (green lines).

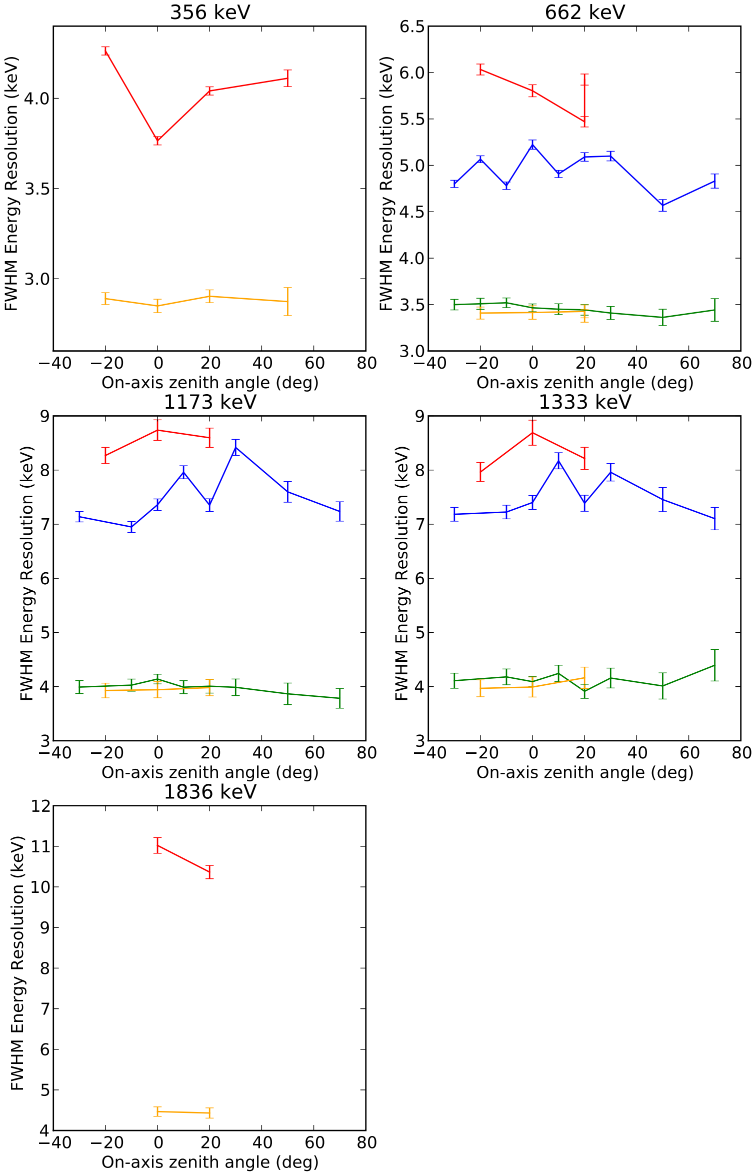

Figure 6.5: Reconstructed photopeak energy resolution (fit FWHM) for effective area calibrations. Fit values for each calibration line are presented versus the zenith angle along the detector centerline. Values from the 2009 New Mexico campaign are blue (data) and green (simulation), while those from the 2010 Australia campaign are red (data) and yellow (simulation). Errors are 90% C.L.

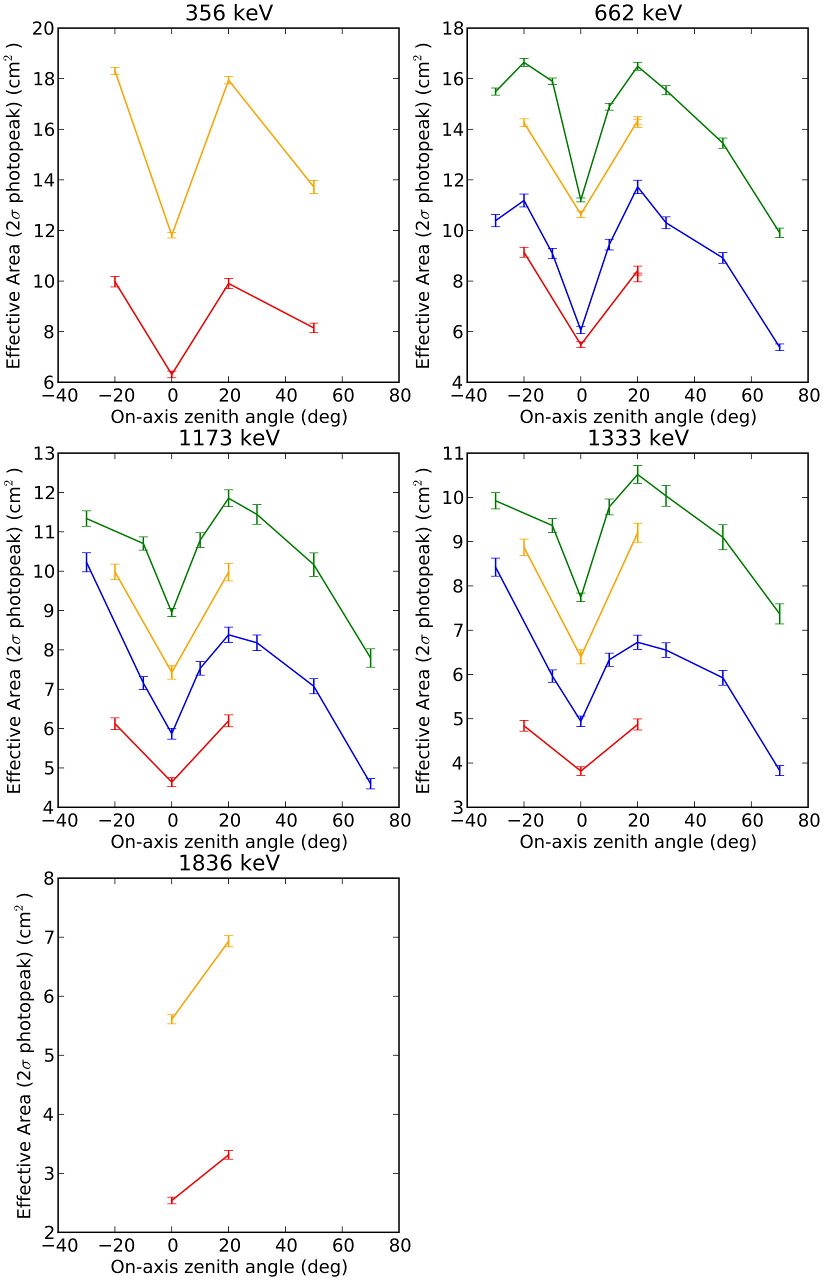

Figure 6.6: Effective area (cm^2) for events within 2σ of the fit photopeak. Colors and symbols as in Figure 6.5.

<table>
<tr><th>Energy (keV)</th><th>Data</th><th>Simulation</th></tr>
<tr><td>356</td><td>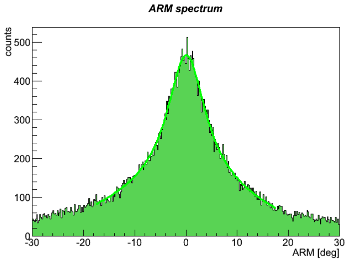
</td><td>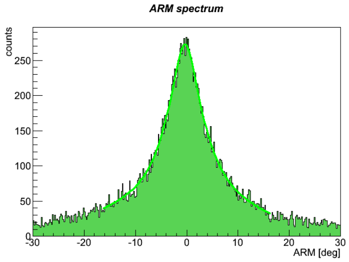
</td></tr>
<tr><td>662</td><td>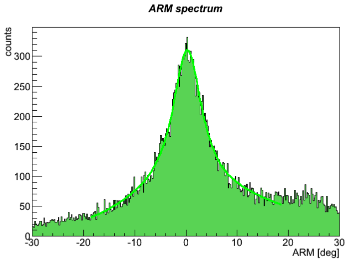
</td><td>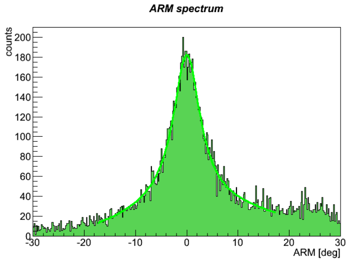
</td></tr>
<tr><td>1173</td><td>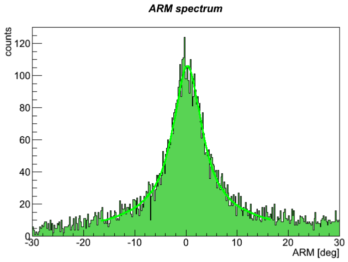
</td><td>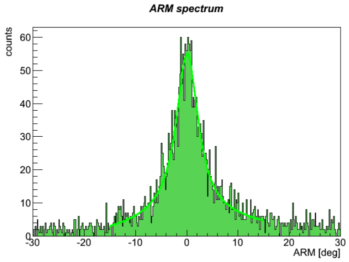
</td></tr>
<tr><td>1333</td><td>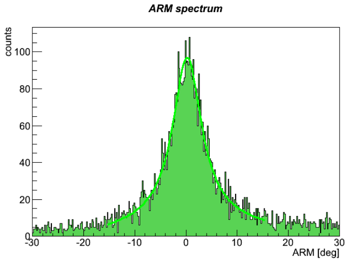
</td><td>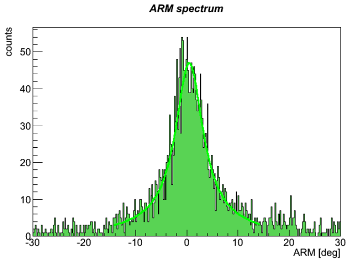
</td></tr>
<tr><td>1836</td><td>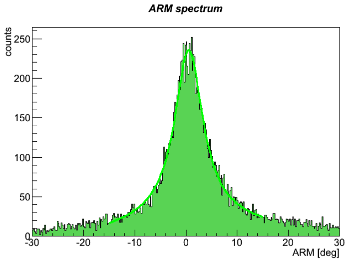
</td><td>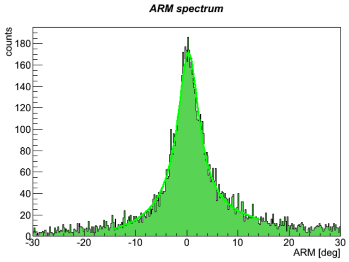
</td></tr>
</table>

Table 6.4: Example ARM fits of the data and simulations for the on-axis 2010 calibrations.

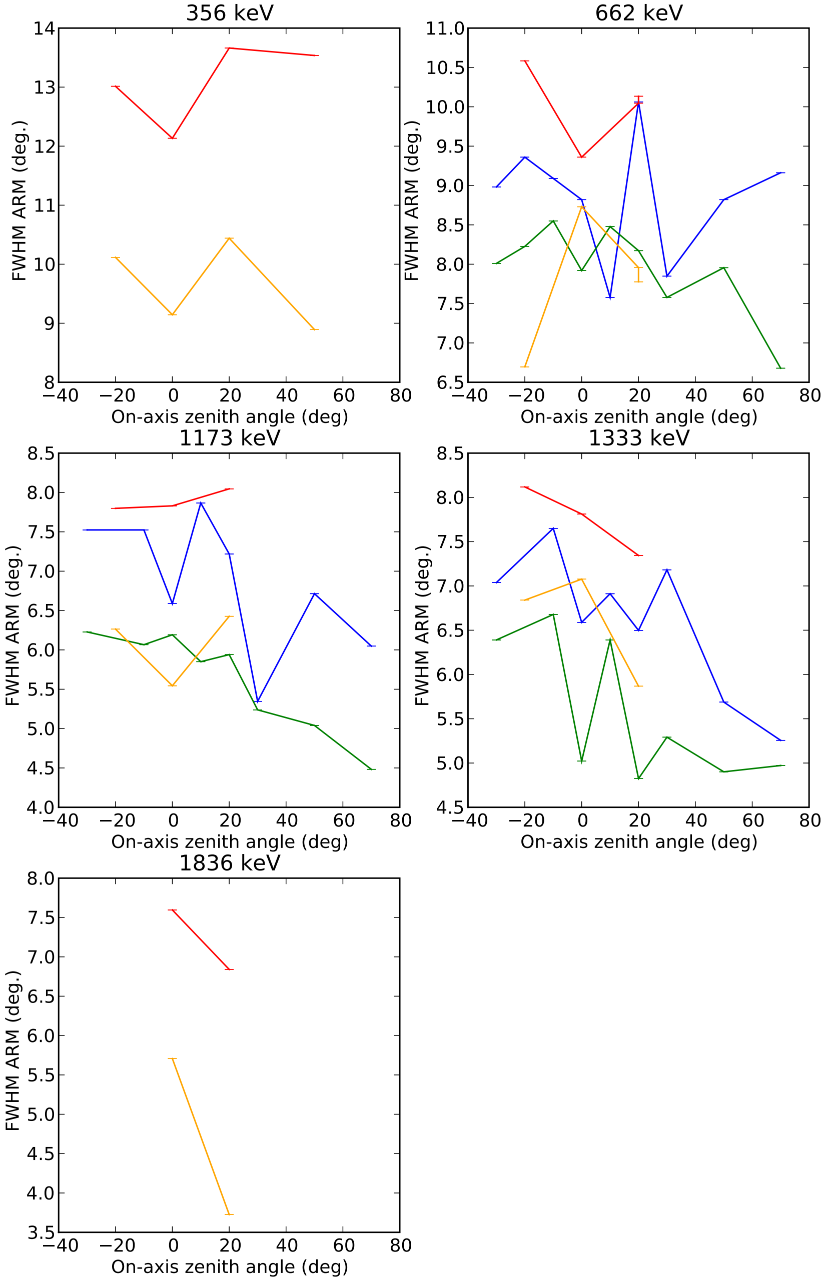

Figure 6.7: FWHM fit ARM for effective area calibrations. Colors and symbols as in Figure 6.5.

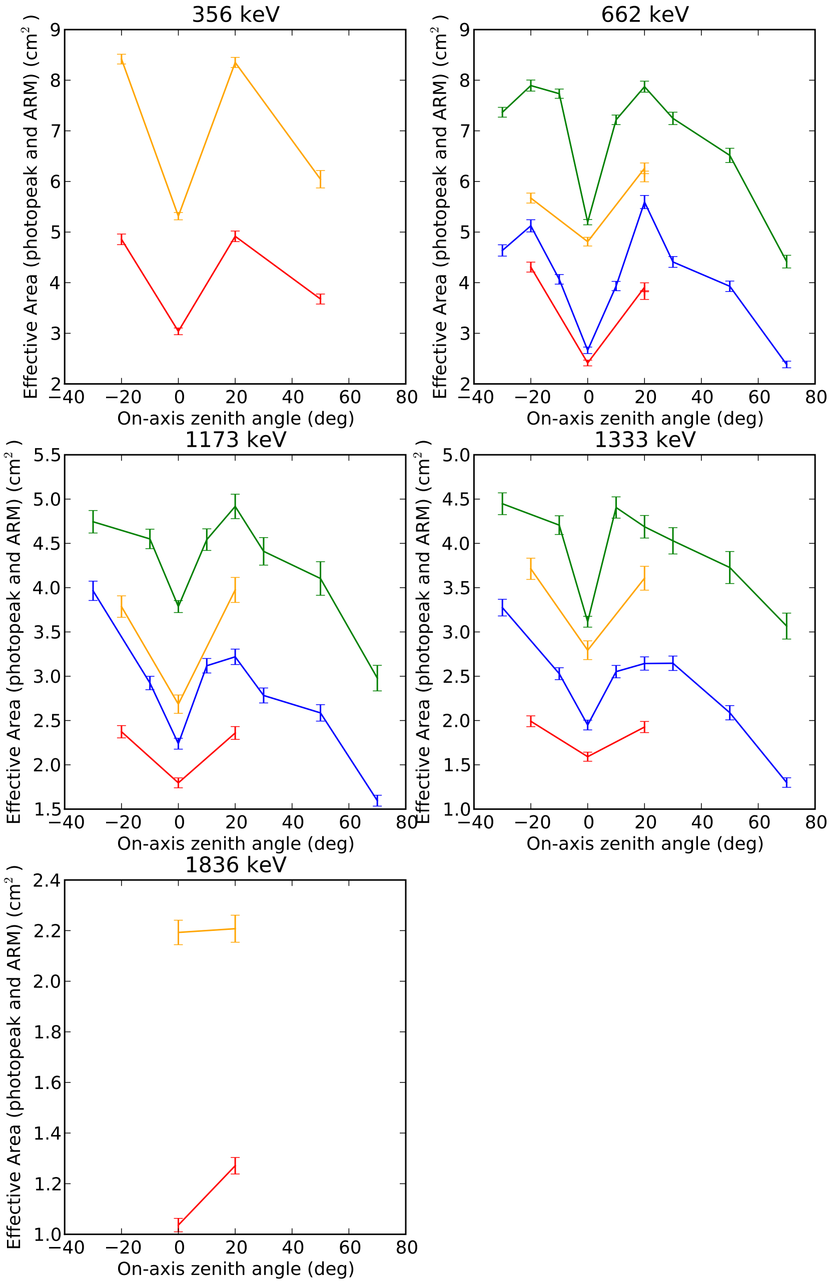

Figure 6.8: Effective area (cm^2) for events within 2σ of the fit photopeak and twice the fit ARM FWHM. Colors and symbols as in Figure 6.5.

6.4 Discussion

Several trends are apparent on examination of the effective area calibration data. First, the widths of the reconstructed photopeaks are significantly larger for the real data than for the simulations (Table 6.3 and Figure 6.5). This suggests that the low-level calibrations used by Nuclearizer (Section 5.6) to process the data may yet be improved. The energy resolution obtained for the 2010 data are slightly higher than those from 2009. This difference results from the need to use a linear energy calibration for these data due to a smaller available energy calibration data set from the Australian campaign.

The fit ARM values are again slightly larger for the data than for the simulations (Figure 6.7), although there is a great deal of overlap and fewer systematic trends are visible.

The derived effective area values (Figures 6.6 and 6.8) show NCT's broad field of view. The 2010 values are lower than those from 2009, as only eight of ten detectors were in operation in Australia[2]. The dip present at zero degrees zenith angle (i.e., on axis) is due to a geometric effect: with the detectors oriented vertically in the cryostat (Figure 5.5), on-axis photons encounter less projected detector area due to the gaps between the detectors. (This gap disappears for photons more than 8° away from zenith along the detector centerline.)

The effective area derived from simulations is systematically higher than that derived from the data. The ratio of the simulated effective area to the data-derived values is roughly 1.4–2.0 for all energies and angles (Figures 6.9 and 6.10). Some characteristic structure is apparent in these ratios, but no regular systematic effects in energy or angle are evident. For some of the larger outliers (the 2009 +70° data and the 2010 0° 662 keV and 1836 keV data), the accuracy of the theodolite localizations are questionable. Potentially, mis-location could contribute to these observed shifts, but the position estimates are the best possible with available data. The addition of the ARM cut does not change the ratios appreciably (Figures 6.9 and 6.9).

The energy and ARM cuts (2σ and $2\times$ the fit FWHM, respectively) for each data point were determined by their fit values, so the broader photopeaks obtained for the data would not create the deficit in the effective area relative to the simulations.

Searching further for differences between the data and simulations, I determined the proportion of single-site and multiple site events in an energy band surrounding the calibration line for these data. For a given isotope and data type (simulation or calibration) the proportion of multiple-site events was constant. The simulations have a slightly higher proportion of multiple-site events: roughly 5% for the ^{137}Cs and ^{60}Co data and 15% for ^{133}Ba. The ^{88}Y simulations showed no such excess. These counts were determined by processing the event files after the application of the calibrations and strip pairing by the Nuclearizer program. The difference is not surprising, therefore, as real data events are more likely to be rejected by Nuclearizer due to imperfect calibrations, with multiple-site events increasing the probability of rejection. Since only multiple-site events may be Compton imaged,

---

[2] The cryostat high-voltage lead to Detector 0 broke during recovery and return transit from New Mexico, while Detector 6 failed to deplete under applied high voltage on arrival in Alice Springs.

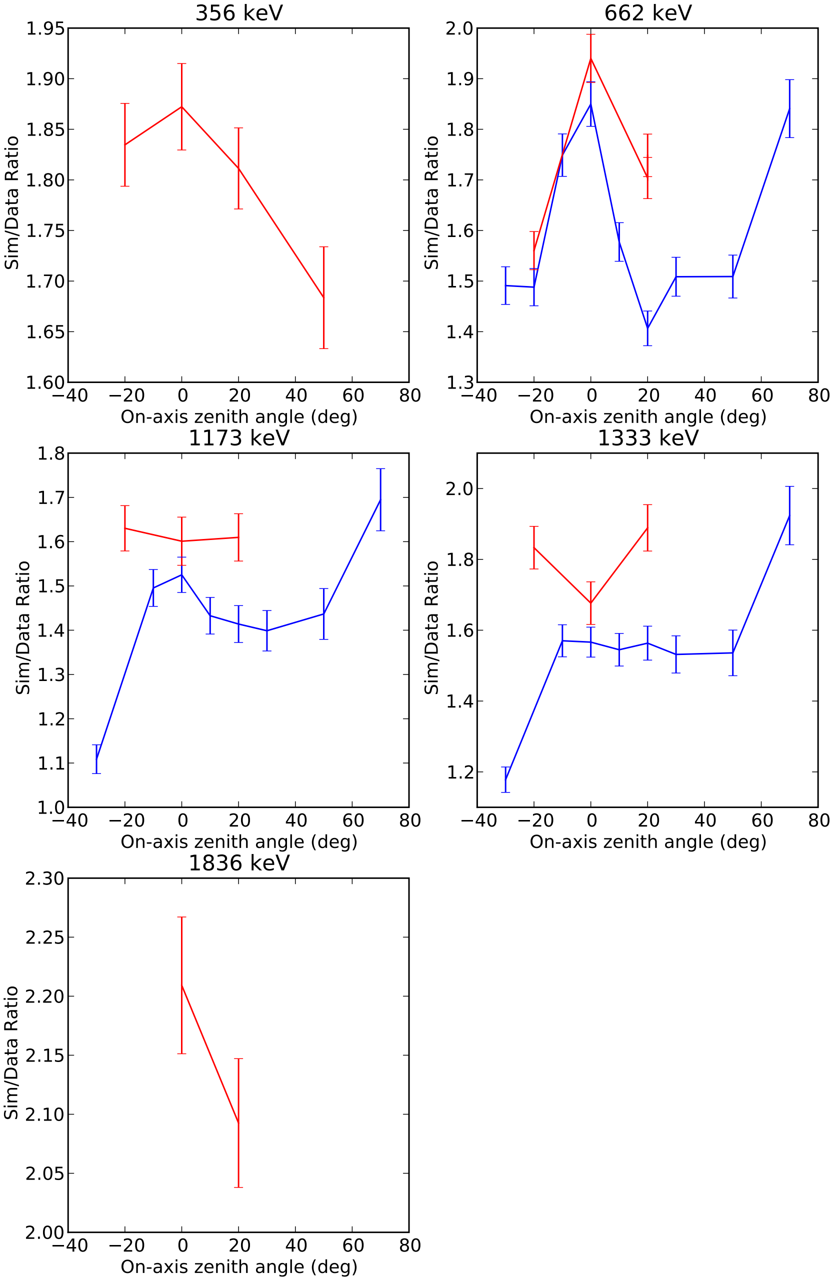

Figure 6.9: Ratio of the simulated effective area to that derived from the data using the energy photopeak cut. Ratios for 2009 are in blue, while those from 2010 are in red.

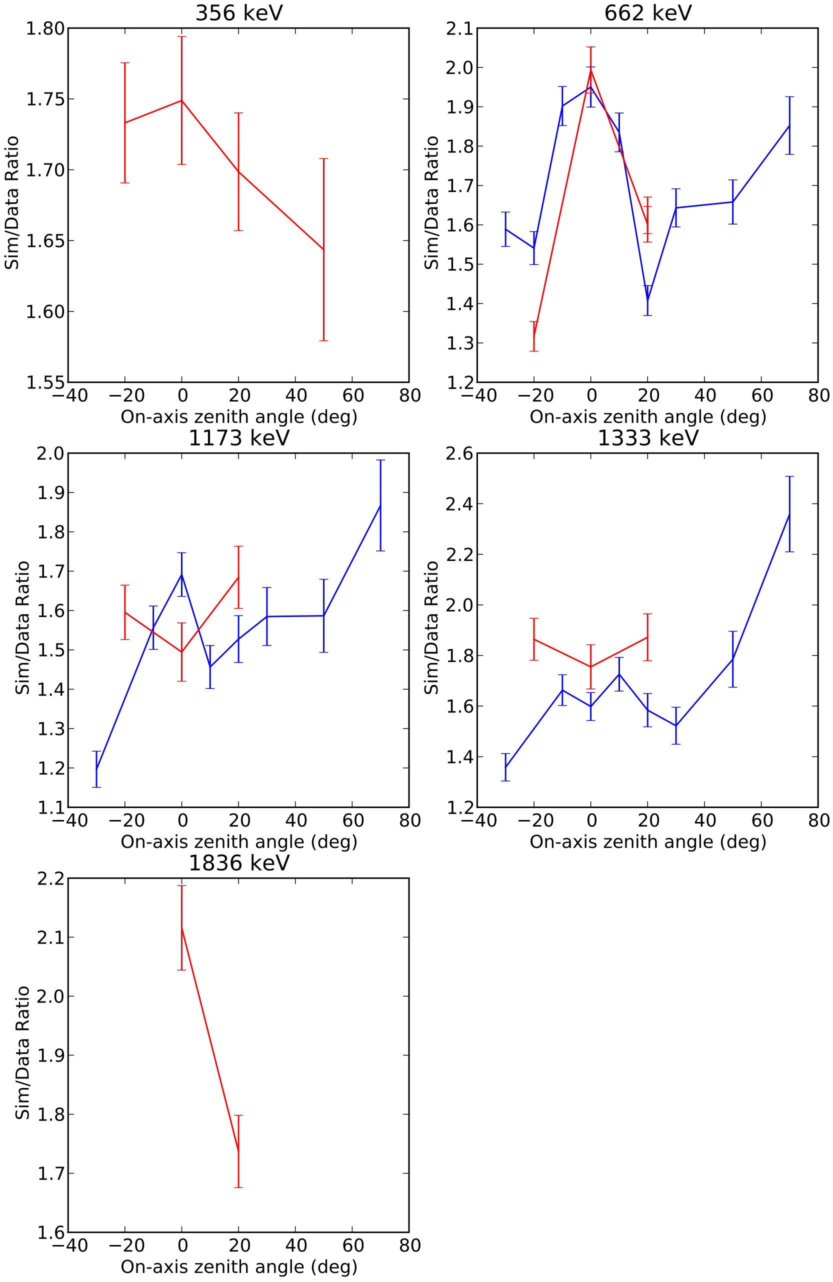

Figure 6.10: Ratio of the simulated effective area to that derived from the data using the energy photopeak and ARM cuts. Colors as in Figure 6.9.

these differences will contribute to the observed effective area discrepancy. In any case, the moderate value of this effect is too small to explain the observed deviation in effective area values.

While the specific cause of the event deficit in the real data is not apparent, there are several areas where this analysis shows potential for improvement in the underlying calibrations. The reconstructed photopeak lines are broader for the real data than for the simulation (Table 6.3), implying that the energy calibration is imperfect. Future energy calibrations with a larger collection of spectral lines may improve the accuracy. More sophisticated treatments of the challenging problems of charge sharing, charge loss, and electronic cross-talk between strips may also narrow the reconstructed linewidth. Further improvements in the strip pairing algorithms should increase the overall detection efficiency for both data and simulations.

The Detector Effects Engine used in the analysis chain for simulations (Section 5.6) takes the ideal interactions generated by Monte Carlo simulations and generates strip hits and ADC energy channels in the same form as the real data. To do so, it implies inverse forms of the energy, depth, and other calibrations. A potentially fruitful means of understanding the observed differences in effective area would be to further degrade the simulated data with the Detector Effects Engine in order to match the properties of the real data. By adding further noise to the calibration inversion, it should be possible to learn the relative influence of the various calibrations on the reconstruction process. This procedure could yield a more faithful representation of the real data as well as guide future calibration efforts.

In summary, the correspondence between data and simulations for these calibrations is imperfect. However, the results are consistent with a generic offset, likely due to incomplete reconstruction caused by imperfect calibrations. Further improvements to the low-level calibrations are possible and may narrow the gap.

Compared to COMPTEL (Figure 31 of Schönfelder et al. 1993), NCT has a smaller maximum effective area but more sensitivity below 1 MeV (Figure 6.11). (Note, however, that the energy and ARM cuts used here are more restrictive than the 3σ cuts of Schönfelder et al.). NCT's ARM values are also significantly higher (Figure 6.12). However, NCT has much better energy resolution (Figure 6.13) and a wider field of view. These results illustrate the potential of compact Compton telescopes like NCT to provide improved observations of astrophysical sources of soft gamma-rays.

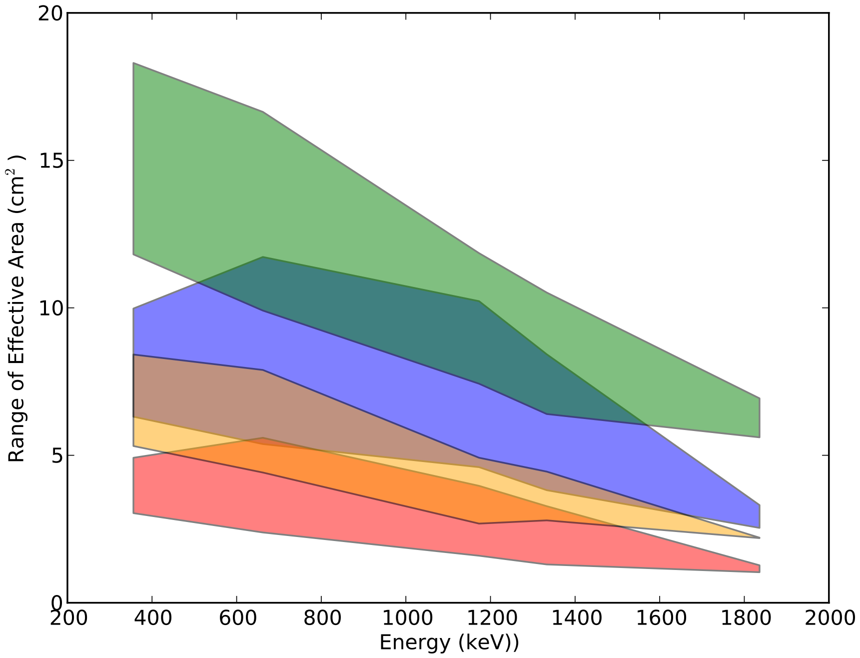

Figure 6.11: Range of effective area values versus energy. Maximum and minimum values for all simulated angles (omitting error bars) are plotted for each energy. Only 2010 (8-detector) data at limited angles are available at 356 and 1836 keV. Blue (green) bands are effective area values from the data (simulations) using the 2σ energy cut on the photopeak. Red (orange) are values from data (simulations) including both the energy and the ARM cuts.

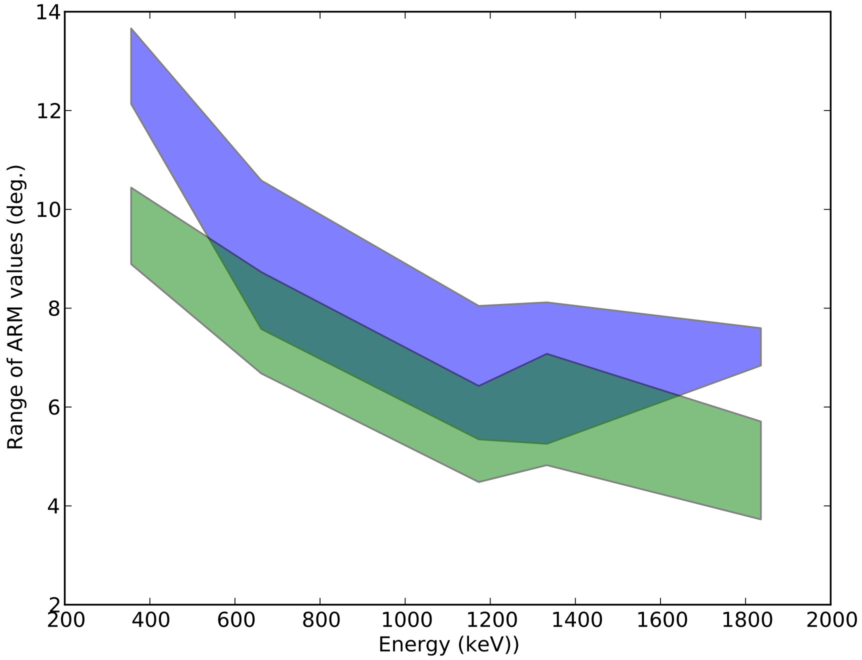

Figure 6.12: Range of ARM values versus energy. Values for data are in blue, while values from simulations are in green. Data selections as in Figure 6.11.

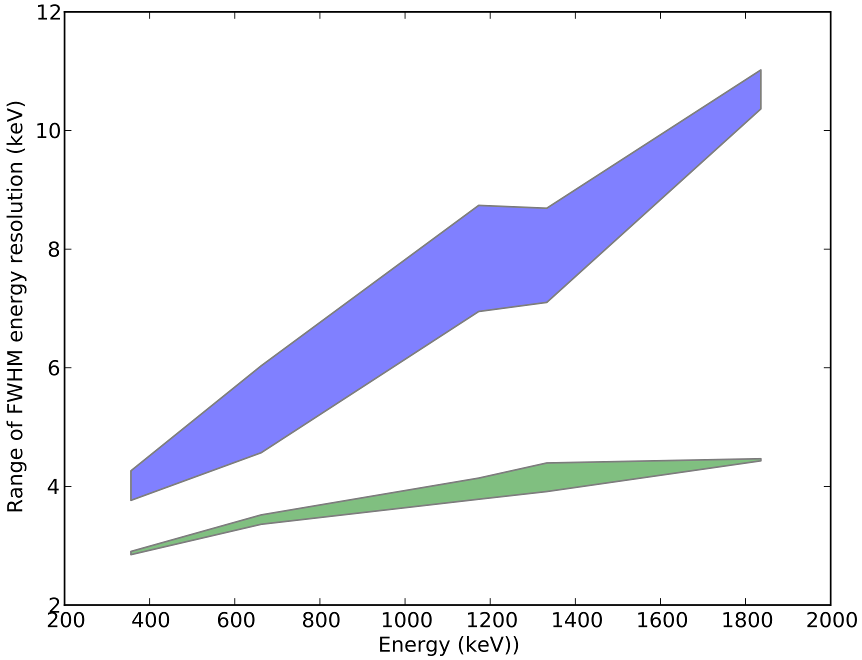

Figure 6.13: Range of FWHM energy resolution values versus energy. Values for data are in blue, while values from simulations are in green. Data selections as in Figure 6.11.

Chapter 7

Polarimetric Performance of the Nuclear Compton Telescope

Abstract

As a Compton telescope, NCT is intrinsically sensitive to polarization. To assess NCT's performance as a polarimeter, I measured a partially-polarized beam in the laboratory and compared its output with Monte Carlo simulations. There is good correspondence for some measurements, but systematic geometric effects are present. Normalizations based on real calibration data yield better results than those derived from simulations. I consider the magnitude of false modulation patterns and assess NCT's performance throughout its field of view.

7.1 Fundamentals of Compton Polarimetry

The Klein-Nishina scattering cross section varies in azimuth relative to the direction of the electric field vector:

$$\frac{d\sigma}{d\Omega} = \frac{r_0^2}{2}\left(\frac{E'}{E_0}\right)^2\left(\frac{E_0}{E'} + \frac{E'}{E_0} - 2\sin^2\theta\cos^2\eta\right) \tag{7.1}$$

where the final photon energy E' is related to the initial energy E_0 by the Compton scatter formula

$$E' = \frac{E_0}{1 + \frac{E_0}{m_e c^2}(1-\cos\theta)} \tag{7.2}$$

and η is the azimuthal angle between the electric field vector of the incoming gamma-ray and the direction of the scattered photon (Figure 7.1).

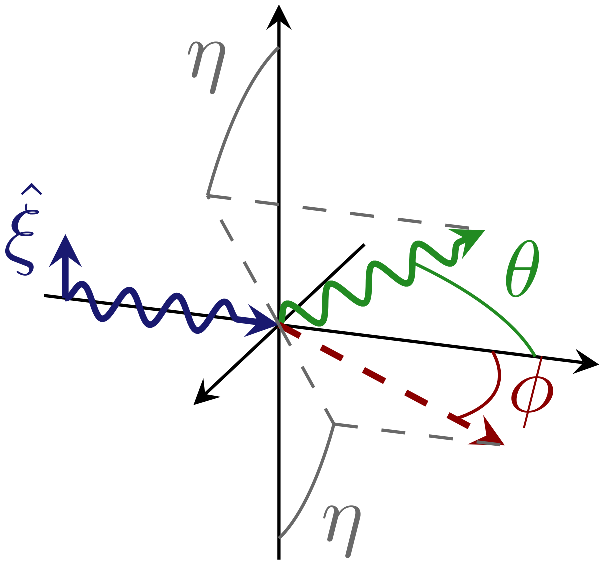

Figure 7.1: Diagram of scattering angles for Compton polarimetry. The azimuthal scatter angle η is defined relative to the direction of the electric field vector $\hat{\xi}$ of the initial photon (blue) and the direction of propagation of the scattered photon (green). The scattered photon has a Compton scatter angle θ relative to the initial direction of propagation, while the recoil electron (red) has angle ϕ.

A polarized beam will therefore be modulated in azimuth (Figure 7.2; see Lei et al. 1997 for a review), with an azimuthal scatter angle distribution (ASAD) at fixed Compton scatter angle θ described by

$$C(\eta) = A\cos 2(\eta - \eta_0) + B \tag{7.3}$$

A and B vary with energy and scatter angle; η_0 is the polarization angle.

The modulation of the ASAD may be described by the modulation factor

$$\mu = \frac{C_{\max} - C_{\min}}{C_{\max} + C_{\min}} = \frac{A}{B} \tag{7.4}$$

and the corresponding linear polarization is

$$\Pi = \frac{\mu}{\mu_{100}} \tag{7.5}$$

where μ_{100} is the modulation of a completely polarized beam. Because of detector geometry and efficiency, reconstruction uncertainties, etc., μ_{100} will in general be less than the ideal modulation

$$Q = \frac{d\sigma(\eta = 90) - d\sigma(\eta = 0)}{d\sigma(\eta = 90) + d\sigma(\eta = 0)} = \frac{\sin^2\theta}{E'/E + E/E' - \sin^2\theta}. \tag{7.6}$$

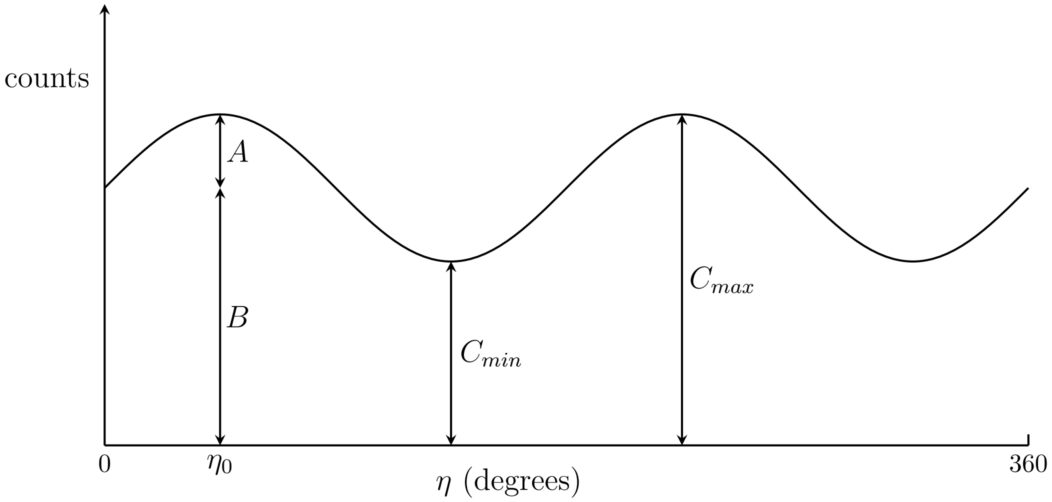

Figure 7.2: Schematic of the Azimuthal Compton Scatter Angle Distribution (ASAD). The maximum and minimum (C_{max} and C_{min}) or amplitude and mean (A and B) define a modulation μ which is determined by the polarization of the source.

Figure 7.3 shows the ideal modulation as a function of Compton scatter angle for several photon energies. The maximum modulation Q_{max} peaks near $\theta_{max} = 90°$ at low energies and decreases as a function of energy, with the location of the peak moving to smaller scatter angles (Figure 7.4).

The minimum detectable polarization at 99% C.L. is

$$\mathrm{MDP} = \frac{4.29}{\mu_{100} S}\sqrt{\frac{S+B}{T}} \tag{7.7}$$

for source count rate S, background count rate B, and observation time T. Since the amplitude of a fit ASAD will always be positive, chance fluctuations may produce an ASAD with nonzero amplitude even when the true polarization is zero. The MDP defines the polarization at which there is only a small chance (here, 1%) that the measured modulation is due to chance fluctuations of an unpolarized source (e.g., Weisskopf et al. 2010; Krawczynski 2011).

Because geometric effects can create azimuthal variations even for unpolarized beams, it is necessary to normalize the ASAD with the ASAD of an identical unpolarized source. Correcting for false modulation patterns is one of the most challenging aspects of polarimetric analysis (e.g., Bloser et al. 2009). These false modulations may arise due to geometric effects in the detector configuration as well as variation in the efficiency of individual detector elements. Typically, a normalization ASAD is produced by simulating (or obtaining calibration data from) a completely unpolarized source which is analogous to the source being analyzed. The source ASAD is then divided by the normalization ASAD. However, discrepancies between the data and normalization can compromise the analysis.

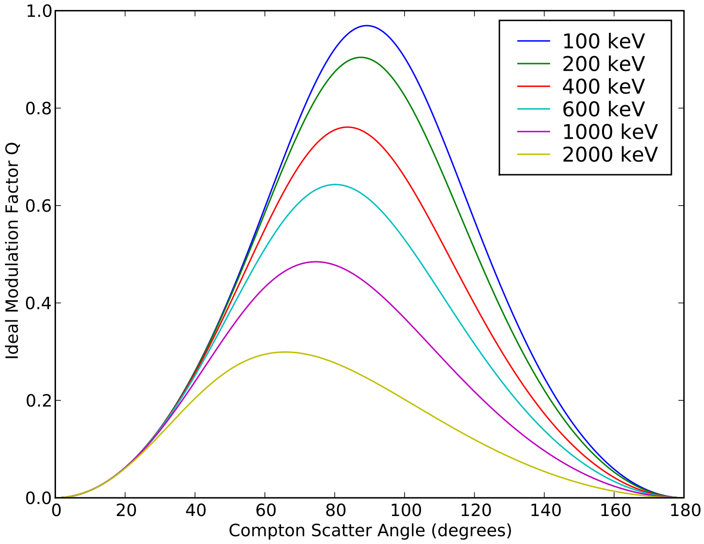

Figure 7.3: Polarimetric modulation as a function of Compton scatter angle for several energies.

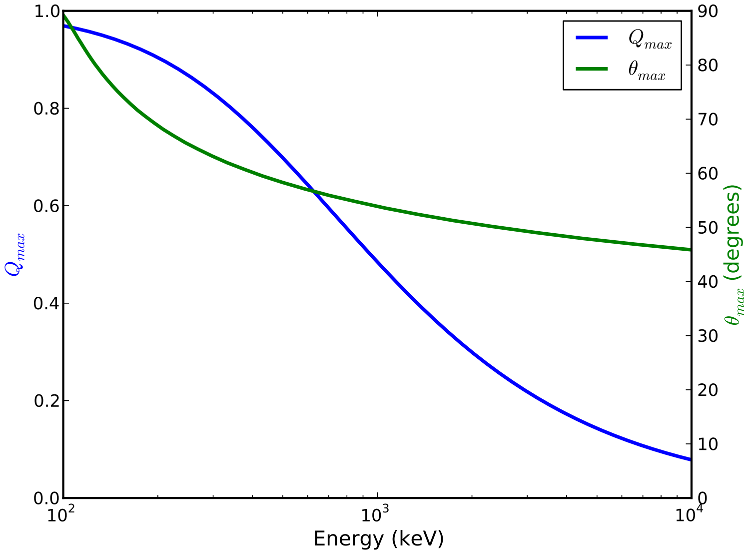

Figure 7.4: Dependence of the maximum modulation Q_{max} (blue) and the Compton scatter angle at which it occurs θ_{max} (green) on the energy of the incident photon.

The analysis method described above requires binning the scattering data for a selected range of Compton scatter angles. Greater sensitivity may be achieved with a Maximum Likelihood approach which utilizes the Compton and azimuthal scattering angles for each event (Krawczynski 2011).

While the polarimetric sensitivity of Compton cameras has been exploited in the laboratory since the 1920s (e.g., Jauncey & Harvey 1931, and references therein), astrophysical Compton polarimetry remains in its infancy. The shallow-angle scattering geometry of COMPTEL and lack of low-energy sensitivity limited its modulation factors to < 0.10 and prevented meaningful polarimetric measurements (Lei et al. 1996). Polarimetric studies of GRBs, solar flares, and the Crab Nebula have been performed with RHESSI (Coburn & Boggs 2003; Wigger et al. 2004; Boggs et al. 2006b), INTEGRAL-SPI (Kalemci et al. 2007; McGlynn et al. 2007; Dean et al. 2008), and INTEGRAL-IBIS (Götz et al. 2009; Forot et al. 2008). However, the large spatial localization of events in these detectors, lack of polarimetric calibration, and high backgrounds complicated these analyses. A wide variety of instruments capable of Compton polarimetry have been implemented as balloon payloads (e.g., Aprile et al. 1994; Bhattacharya et al. 1999; Boggs et al. 2004; Bloser et al. 2006; Kishimoto et al. 2007; Kamae et al. 2008; Ueno et al. 2008; Krawczynski et al. 2009). To date, the small size of these payloads and short observations permitted by balloon flights has prevented polarimetric constraints on astrophysical sources. Many Compton polarimeters have been proposed as satellite instruments; the first in development is the Soft Gamma-ray Detector (SGD) on the Japanese mission Astro-H (Kokubun et al. 2010).

7.2 Laboratory Tests of NCT's Polarimetric Sensitivity

7.2.1 Experimental Setup

To test NCT's polarimetric response, I produced a partially polarized beam by scattering 662 keV photons from a ^{137}Cs source at 90° off of a planar CsI scintillator slab[1]. Ideal scattering would produce a 288 keV beam with 57.8% polarization (Equations 7.2 and 7.6). In practice, the near-field geometry allowed photons scattered through a range of angles to reach the detector, broadening the energy spectrum and decreasing the polarization. I chose the 0.5 m slab–detector and slab–source separations by optimizing a semi-analytic calculation of the expected net polarization versus the integration time achievable with overnight calibrations. These calculations also confirmed that greater polarization would be achieved by placing the source on a line perpendicular to the wide edge of the slab.

Figure 7.5 shows the laboratory setup for one calibration. Machined aluminum mounts held the slab at a user-determined angle in 15° increments. An overhead crane suspended the slab; after positioning with plumb bobs and a laser angle finder, I secured it in position with twine. I used lead bricks to shield the source from the detectors to keep data rates into the card cages low.

---

[1] For one measurement, I used a 45° scattering angle to produce a lower-energy beam (Table 7.1).

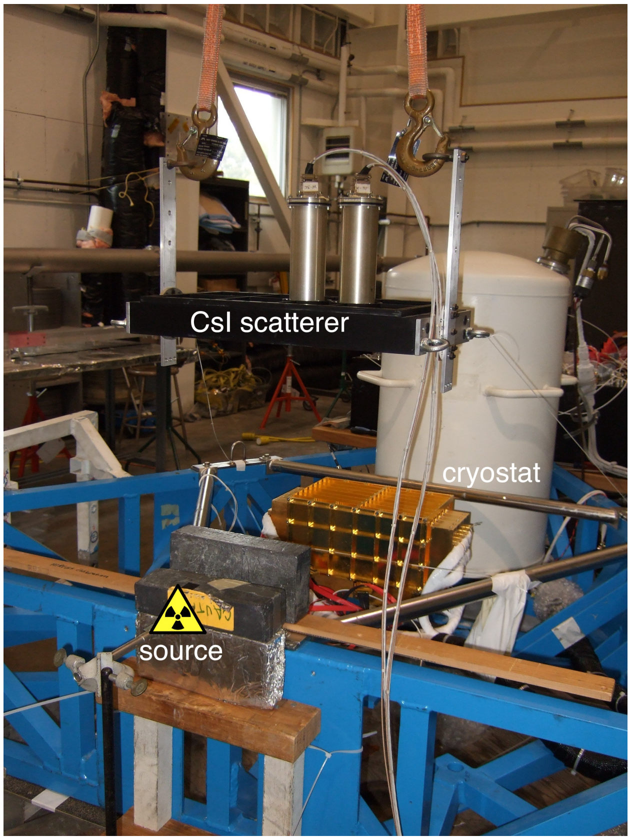

Figure 7.5: Laboratory setup for polarization calibrations. The configuration shown is for the 091006 and 091007 measurements (Table 7.1).

I triggered the CsI slab in coincidence with the NCT detectors using the "soft-veto" mode of the NCT shield electronics. (These calibrations occurred between the 2009 and 2010 balloon campaigns, and the BGO shields were removed for the calibrations.) Only events triggering both the CsI slab and the NCT detectors were used for further analysis, reducing background. Figure 7.6 shows the background spectrum obtained with coincidence triggering active but no source. The background rate is much lower than the source rate, and chance coincidences are thus negligible in these calibrations. Figure 7.7 shows an example Compton image of the scattering geometry; the CsI slab is clearly visible.

I generated partially polarized beams at several positions within the field of view and at several polarization angles. Table 7.1 summarizes the observations presented here, while Table 7.2 shows the geometric configuration for each calibration.

7.2.2 Analysis Methods

I reduced the data using the methods described in Section 5.6. I used theodolite measurements to determine the position of the CsI slab and the radioactive source relative to the

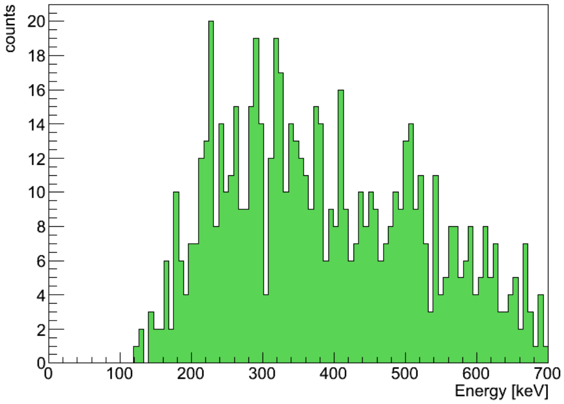

Figure 7.6: Coincidence background spectrum for polarization measurements. The spectrum includes two hours of data, and events were selected from within a 20°-radius circle about an arbitrary point.

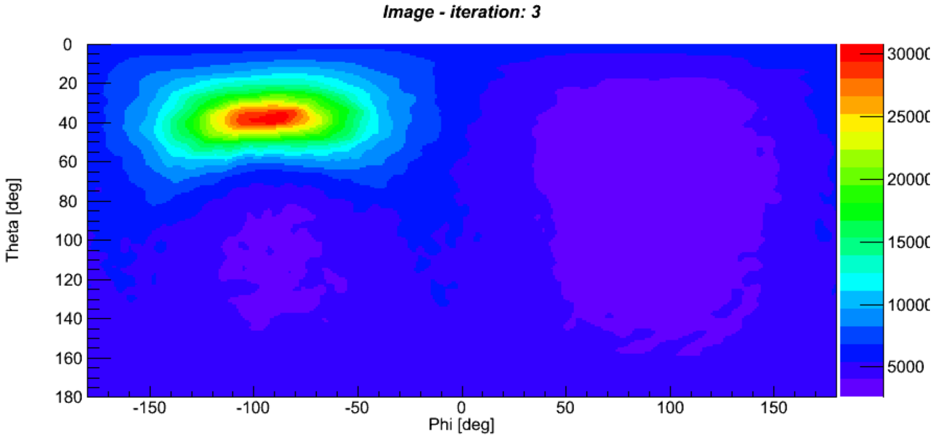

Figure 7.7: Compton image of the polarized scattering off of the CsI slab for the 091006 calibration. Three iterations of Maximum Likelihood Expectation Maximization were applied. Photon energies were restricted to ±1σ, which for this observation corresponded to 212–301 keV.

Date	Compton Scatter Angle	Beam Center (θ, ϕ)	Azimuth of Source	Beam Energy (keV)
090921	45°	45°, 0°	0°	204 ± 34
091006	90°	45°, 0°	0°	256 ± 44
091007	90°	45°, 0°	0°	258 ± 44
091022	90°	45°, 0°	-90°	260 ± 58
091103	90°	0°, 0°	-90°	253 ± 62
091104	90°	0°, 0°	0°	258 ± 68
091105	90°	0°, 0°	90°	251 ± 70
091112	90°	30°, 45°	45°	252 ± 51

Table 7.1: Configuration of the polarization calibrations presented in this work. Here, azimuth angles of 0 correspond to the forward direction, with angles increasing counterclockwise. The measured mean and 1σ beam energies are listed. Calibrations with identical beams but varying polarization angles are separated from other measurements by horizontal lines.

cryostat. These positions allowed me to recreate the scattering geometry for each calibration in a Cosima mass model (Table 7.2). I directly simulated the full scattering geometry in order to obtain the best comparison with the measured beam. Figure 7.8 shows example energy spectra for the calibration and scattering simulations. I compare polarimetric fits of the simulated and measured partially polarized beams in the next section.

Table 7.2: Cosima mass models of the scattering geometries for the polarization calibration. The CsI slab, lead shielding, and source (green dot) are visible.

Calibration Date	Configuration
090922	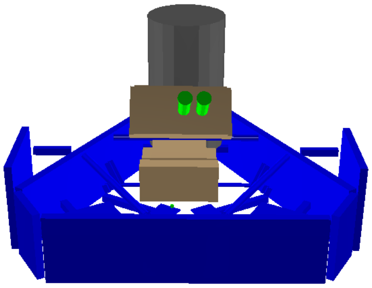

Continued on next page

Table 7.2 – continued from previous page

Calibration Date	Configuration
091006, 091007	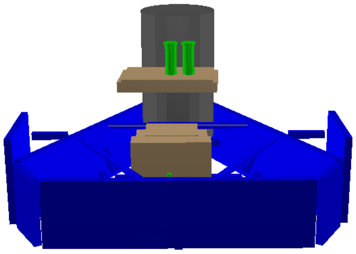
091022	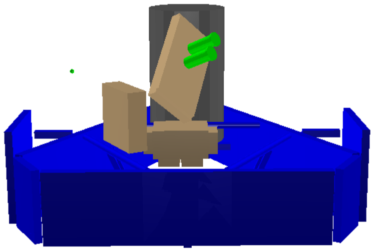
091103	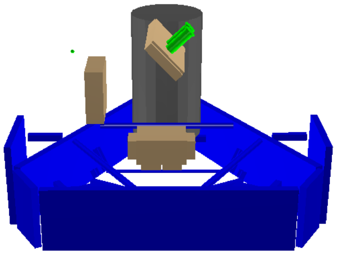

Continued on next page

Table 7.2 – continued from previous page

Calibration Date	Configuration
091104	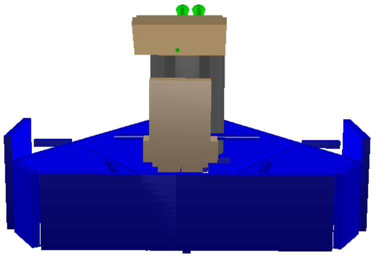
091105	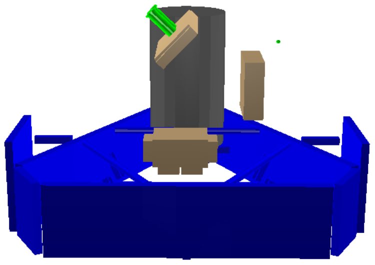
091112	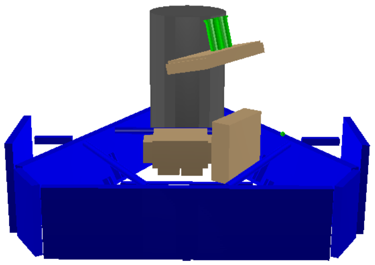

Generation of an analogous unpolarized normalization for this calibration configuration is challenging. The near field geometry means that photons reaching the detector have scattered at different angles from the slab. Accordingly, there is a complex spatially-dependent

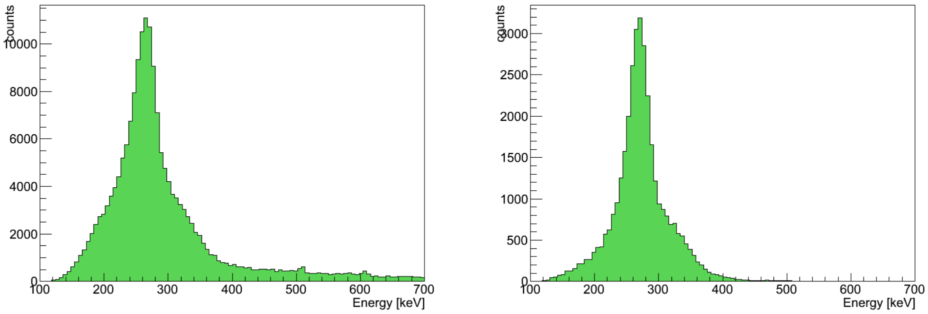

Figure 7.8: Example energy spectra for the measured (left) and simulated scattering (right) data for the 091006 calibration. A 20° ARM cut restricts the beam origin to the CsI slab.

Parameter	Allowed Range
Photon Energy	$\pm 1\sigma$ from fit photopeak
ARM	20°
Number of Interactions	2–7
Compton scatter Angle (θ)	any
Distance between first two interactions	1–20 cm
Distance between other interactions	any
Compton Quality Factor	0–1

Table 7.3: Event cuts used for the polarization analysis.

energy flux from the slab which results directly from the scattering process. To attempt to match as much of the process as possible, I obtained energy spectra for each calibration run. I used these spectra as tabulated source spectra for new simulations. To retain the near field geometry, I used a 3D source beam in the shape and position of the actual scattering CsI slabs.

Table 7.3 describes the event cuts used to analyze the scattering data. To improve the homogeneity of the beam, I used a 1σ energy cut. The 20° ARM cut corresponded to the angular size of the CsI slab at the 0.5 m distance. While the polarization modulation varies with Compton scattering angle (Figure 7.3), I included all scattering angles in the analysis.

To determine the maximum modulation for each calibration μ_{100}, I simulated 100% polarized beams using the measured energy spectra for each calibration. To avoid the complications of the near-field beam, for these simulations I simulated point sources at infinity. I normalized the ASADs for each simulation with a 0% polarized beam with the same input parameters.

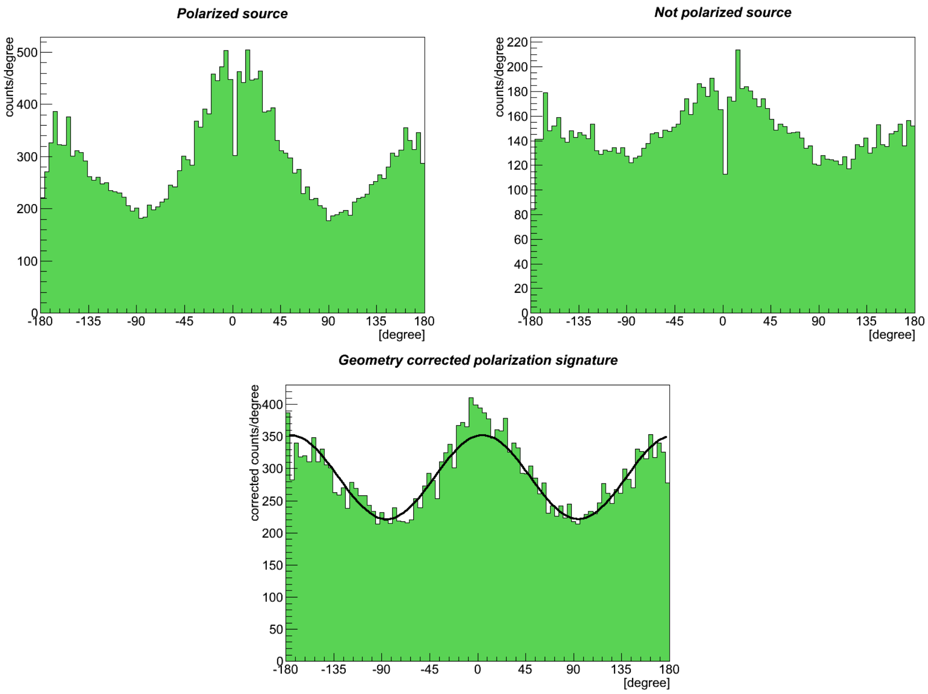

Figure 7.9: The raw ASAD, unpolarized normalization, and fit modulation of the 091006 calibration.

Date	μ_{data}	μ_{sim}	μ_{100}	Π_{data}
090922	0.062±0.013	0.035±0.039	0.542±0.050	0.114±0.026
091006	0.228±0.009	0.209±0.019	0.459±0.043	0.497±0.050
091007	0.230±0.009	”	”	0.501±0.051
091022	0.149±0.009	0.246±0.025	0.473±0.044	0.315±0.035
091103	0.115±0.007	0.211±0.024	0.446±0.041	0.258±0.028
091104	0.172±0.008	0.224±0.026	0.508±0.041	0.339±0.032
091105	0.124±0.007	0.224±0.025	0.500±0.038	0.248±0.023
091112	0.166±0.009	0.219±0.025	0.539±0.039	0.308±0.028

Table 7.4: Fit modulation factors for the polarization calibrations and 1σ errors.

7.2.3 Results

I used MEGAlib to fit Equation 7.3 to the measured data, scattering simulations, and μ_{100} simulations. Each ASAD was normalized by a corresponding unpolarized simulation as described in the previous section. Figure 7.9 shows an example fit. Table 7.4 lists the fit modulations for each calibration.

The correspondence between the fit modulations of the calibration data (μ_{data}) and the scattering simulations (μ_{sim}) range from excellent to moderate, with several systematic trends. The best match occurs for the (geometrically identical) 091006 and 091007 calibrations; μ_{data} and μ_{sim} agree within errors.

Data and simulation also agree for the low-energy 090922 calibration. While the modulation should be largest at lowest energies (Figure 7.3), both μ_{data} and μ_{sim} are small for this measurement, where a 45° Compton scatter angle produced a beam of 200 keV, about 50 keV lower than the other calibrations. The μ_{100} value for this calibration is large, however. Since there is agreement between the data and the scattering simulations, these low modulations likely indicate that the polarized beam generated by the shallow scattering off of the CsI slab was of poor quality. The large simulated μ_{100} value shows that NCT has significant polarimetric capability at 200 keV.

For the other calibrations, μ_{data} is smaller than μ_{sim} by 20–50%. As with the effective area data (Chapter 6), the largest deviations occurs with on-axis beams. There seems to be a connection between the data–simulation disagreement and the geometry of the calibration: those calibrations with source polarization angles perpendicular to the detector faces fare the worst. (This occurs when the scattering source is to the side of the detectors.) The largest disagreements are thus the 091103 and 091105 calibrations; the on-axis beam means the beam polarization is exactly perpendicular. Intermediate cases of disagreement (091022 and 091112) have only a component of the polarization vector perpendicular to the detector faces or (091104) are on-axis but have polarization parallel to the detector faces.

The fit polarization angles were consistent within errors between the measurements and scattering simulations (Figure 7.10), except for 091105 which had a less secure theodolite localization. The expected 90° shift occurs between the calibrations with varying polarization angle (091006 and 091022; 091103, 091104, and 091105; see Table 7.1).

The μ_{100} simulations use the measured energy spectra as inputs, but they do not depend on the theodolite localization or near-field geometry. The inferred modulations are roughly constant for all calibration angles considered (Table 7.4), suggesting that the variation in the observed modulation factors reflects the difficulty of producing a partially-polarized beam by scattering rather than intrinsic variation in NCT's polarimetric response.

Due to the variation in μ_{data}, the inferred polarizations $\Pi_{data} \equiv \mu_{data}/\mu_{100}$ vary from 0.25–0.50. The mean energies of the energy spectra (Table 7.1) imply that most photons are scattered at angles $\theta = 101°$–$105°$ off of the CsI slab. The corresponding ideal modulations Q are in the range 0.49–0.45, which are exceeded slightly by the 091006/091107 calibrations but are significantly larger than the measured Π_{data} for all other calibrations.

7.2.4 Other Normalization Approaches

Normalizing the measured ASAD by the ASAD of an unpolarized beam is essential to avoid false modulations induced by geometric effects (Section 7.2.5). However, any discrepancies between the unpolarized beam and the source beam can influence the fit values.

I used multiple calibration data sets to generate unpolarized ASADs to compare with the Monte Carlo-based normalizations used in the previous section. The three on-axis calibrations (091103, 091104, and 091105) have polarization angles which increase consecutively

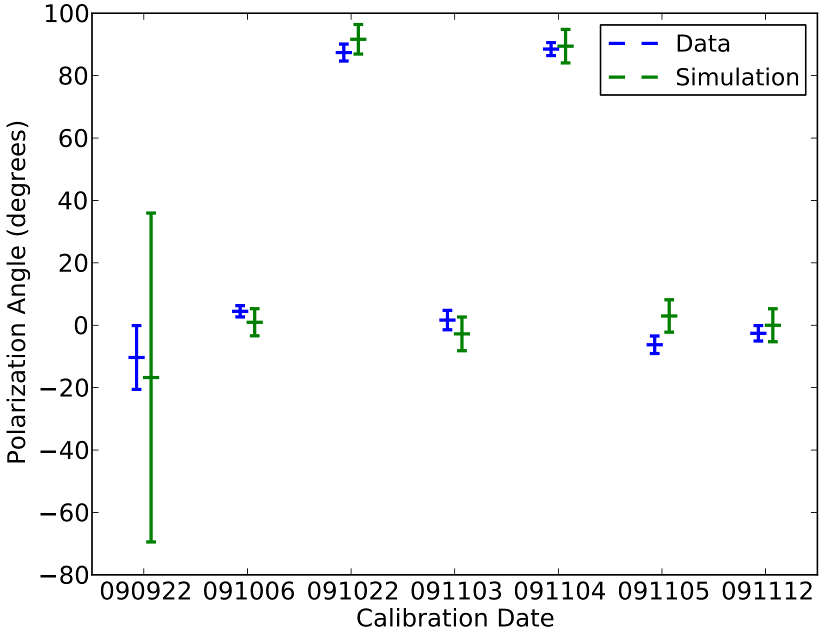

Figure 7.10: Fit polarization angles η_0 for each calibration. Measured values are blue, while those from the scattering simulations are green. The zero-point of the ASAD is defined by the direction of the incoming beam. Uncertainties are 90% C.L.

by 90°. Accordingly, combining adjacent pairs produces an unpolarized beam which can be used as a normalization for the third calibration. Thus, I fit the 091103 data normalized by the (091104+091105) data and the 091105 data normalized by the (091103+091104) data. Table 7.5 shows the resulting fits.

The fit values obtained with normalizations derived from real data are superior to those obtained from Monte Carlo simulations. The modulations obtained (0.186±0.008 for 091103 and 0.175±0.007 for 091105) are closer to the expected values of μ_{sim} than the simulation-normalized results (Table 7.4). The fit polarization angles are unchanged. Most notably, however, the goodness of fit of the ASAD modulation improves markedly: from $\chi^2/\mathrm{dof} = 156.7/87$ to $80.9/87$ for 091103 and from $\chi^2/\mathrm{dof} = 165.4/87$ to $114.9/87$ for 091105.

These results emphasize that polarimetric measurements are particularly sensitive to any discrepancies between the Monte Carlo simulations and the real detectors (see also Bloser et al. 2009). Variations in the channel-to-channel response due to readout electronics are particularly difficult to capture in simulations. Imperfections and simplifications in mass models will also compromise the fidelity of polarimetric simulations.

Since GRBs can come from any direction and have varied continuum spectra, it is impossible to obtain unpolarized laboratory calibration data at all astrophysically relevant energies, directions, and polarization angles. However, Monte Carlo normalizations should

Calibration Date	Simulation Normalization	Data Normalization
091103	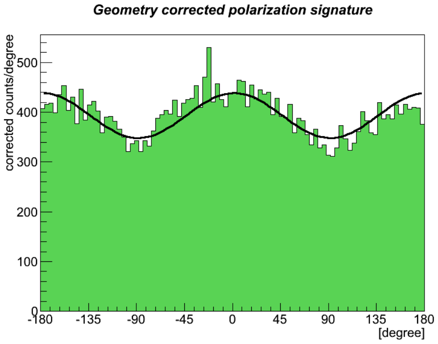 Geometry corrected polarization signature	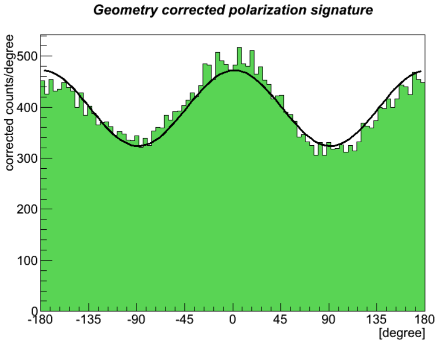 Geometry corrected polarization signature
091105	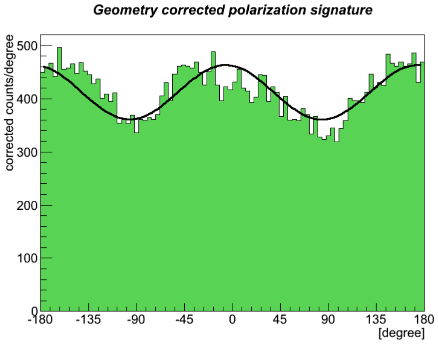 Geometry corrected polarization signature	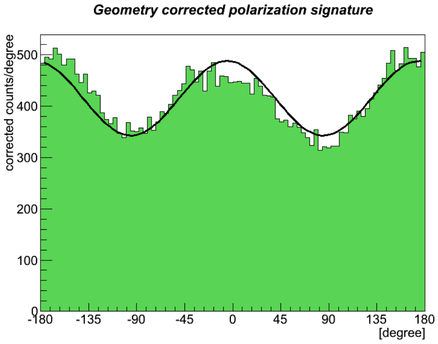 Geometry corrected polarization signature

Table 7.5: ASAD fit comparison for calibration data normalized by simulations (left) and unpolarized real data (right). Two partially-polarized beams with perpendicular polarization angles were combined to produce the unpolarized normalization. The statistical quality of the fits are better with the real data normalization.

be grounded with laboratory calibrations for reliability. "Re-normalizing" simulations with relevant laboratory data would be an important step towards mature Compton polarimetry; confronting this problem is a challenge which remains for future analysis.

7.2.5 False Modulation Effects

In order to determine the magnitude of the false modulations introduced by geometric and detector effects in the NCT detectors, I fit modulation curves to the ASADs of the effective area calibration data using the event cuts of Chapter 6. I used the 2009 ^{137}Cs data and the 2010 ^{133}Ba data. The fit modulation amplitudes were 0.050–0.094 at 356 keV for the ^{133}Ba data and 0.004–0.074 at 662 keV for the ^{137}Cs data. Since the effective area calibrations have 0.5–3.0 $\times 10^4$ counts after the energy and ARM cuts, these amplitudes are larger than would be expected from random fluctuations at 99% C.L. ($4.29/\sqrt{N} = 0.025$–0.060).

Several effects are likely to contribute to these false modulations. Geometric and detector effects not captured in the Monte Carlo simulations prevent optimal normalization. Also, imperfect theodolite localizations mean that the spatial cuts derived from the calibra-

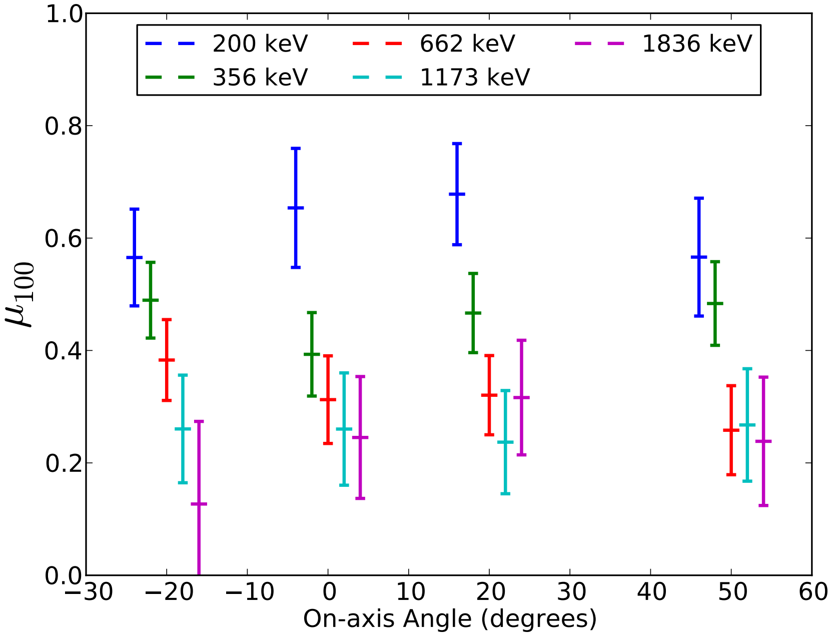

Figure 7.11: Modulation factors for 100% polarized beams of several energies throughout the NCT field of view. Points are offset about the incident angle for clarity. Uncertainties are 90% C.L.

tion data may not match the simulation source direction exactly[2]. Finally, two detectors were not functioning in 2010, decreasing the homogeneity of the detector volume.

7.3 Monte Carlo Characterization of NCT's Polarimetric Performance

Section 7.2 explored the correspondence between NCT's laboratory polarimetric performance and simulations. Because of the challenges of the near-field scattering geometry–partially polarized beams, difficult normalization, broad energy spectra–I turn to Monte Carlo simulations to determine astrophysically-relevant polarimetric modulation factors. I simulated 100% and 0% polarized monoenergetic point sources at several energies throughout the field of view. I simulated photons at NCT's lower-energy limit, 200 keV, where the expected modulation is greatest (Equation 7.6). I also simulated photons at 356, 662, 1173, and 1836 keV to compare with ^{133}Ba, ^{137}Cs, ^{60}Co, and ^{88}Y simulations, respectively. Figure 7.11 shows the modulation factors at four points in the NCT field of view.

---

[2] This problem may be avoided by extracting normalization ASADs with independent spatial cuts.

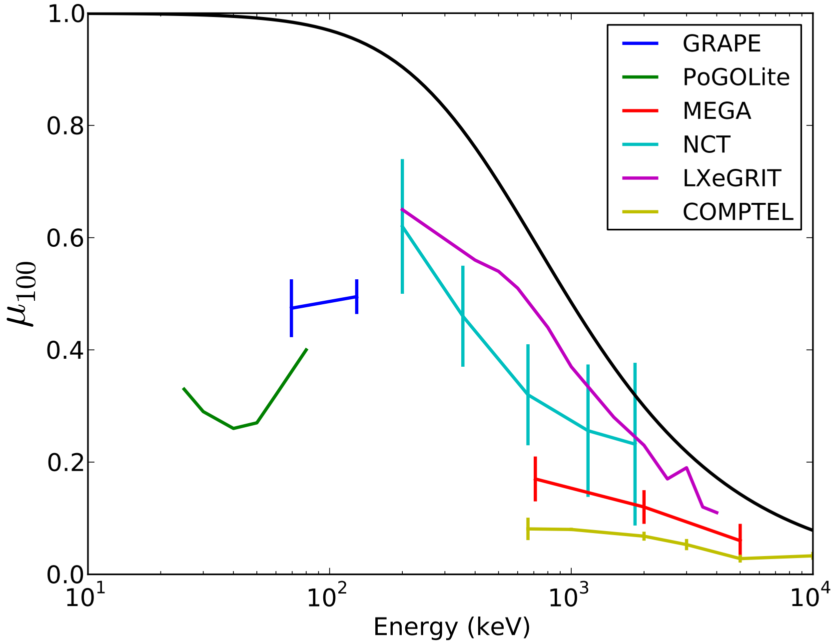

Figure 7.12: Maximum modulation μ_{100} as a function of energy for several Compton polarimeters. The maximum modulation at a given energy $Q_{max}(E)$ is overplot; the plot modulations include a range of Compton scatter angles and accordingly must be smaller than Q_{max}. Errors are 1σ.
References for the data: GRAPE: Bloser et al. (2009); PoGOLite: Kamae et al. (2008); MEGA: Zoglauer et al. (2004b); NCT: this work; LXeGRIT: Aprile et al. (1994); COMPTEL: Lei et al. (1996).

While there is variation throughout the field of view, the modulation values are consistent with a constant at a given energy. The mean values and 1σ errors at each energy are $\mu_{100}(200\text{ keV}) = 0.62 \pm 0.12$, $\mu_{100}(356\text{ keV}) = 0.46 \pm 0.09$, $\mu_{100}(662\text{ keV}) = 0.32 \pm 0.09$, $\mu_{100}(1173\text{ keV}) = 0.26 \pm 0.12$, and $\mu_{100}(1836\text{ keV}) = 0.23 \pm 0.14$. Figure 7.12 plots these modulations as a function of energy and compares them to values obtained by other instruments.

7.4 Summary

I conducted laboratory tests of NCT's polarimetric sensitivity and compared the results with Monte Carlo simulations. The fit modulation amplitudes showed good correspondence for some calibrations, while in others the data showed lower modulation than predicted by simulations. These differences were correlated with the geometric configuration of the partially polarized beam. I found that normalization of the scattering angle distribution by real data yielded better results than Monte Carlo normalization. NCT's polarimetric performance is comparable to other Compton polarimeters. These results highlight the challenges of accurate polarimetric analysis and emphasize the need for extensive ground calibration.

Chapter 8

NCT as a Transient Monitor

Abstract

NCT's wide field of view, moderate effective area, and imaging capability make it well-suited to detect gamma-ray transients like GRBs. I use flight data, ground calibrations, and Monte Carlo simulations to characterize NCT's sensitivity to GRBs. I calculate expected GRB detection rates and discuss the potential to place polarimetric constraints on the prompt emission.

8.1 Transient Detection Characteristics

Key parameters for evaluating the performance of a transient monitor include its field of view, temporal resolution, detection efficiency, and background.

NCT has a wide field of view, with a total extent of $\sim\pi$ sr (Figure 8.1). Its extent is determined by the presence of the BGO shields. For a balloon-borne instrument, this configuration is optimal, as it shields the instrument from atmospheric background while allowing observations of celestial sources at elevations above 30°. (At lower elevations, heavy atmospheric absorption limits sensitivity.) As presently configured, NCT's liquid nitrogen dewar blocks some of the field of view, while the vertical orientation of the detectors creates a deficit in the effective area on-axis. Future versions of NCT may be reconfigured with a cryocooler and the detectors oriented horizontally, improving both the potential flight duration and its overall sensitivity .

NCT has extremely fine time resolution. Events are tagged by a 10 MHz clock, although in practice the absolute timing accuracy is limited by the need to interpolate between the 1 Hz GPS time references. Because the data are stored event by event, no time binning is imposed *a priori* on transient analyses.

NCT's effective area for imaged Compton events (2 or more interactions) is small relative to high-energy survey instruments like BATSE or *Swift* (Chapter 6). However, NCT also

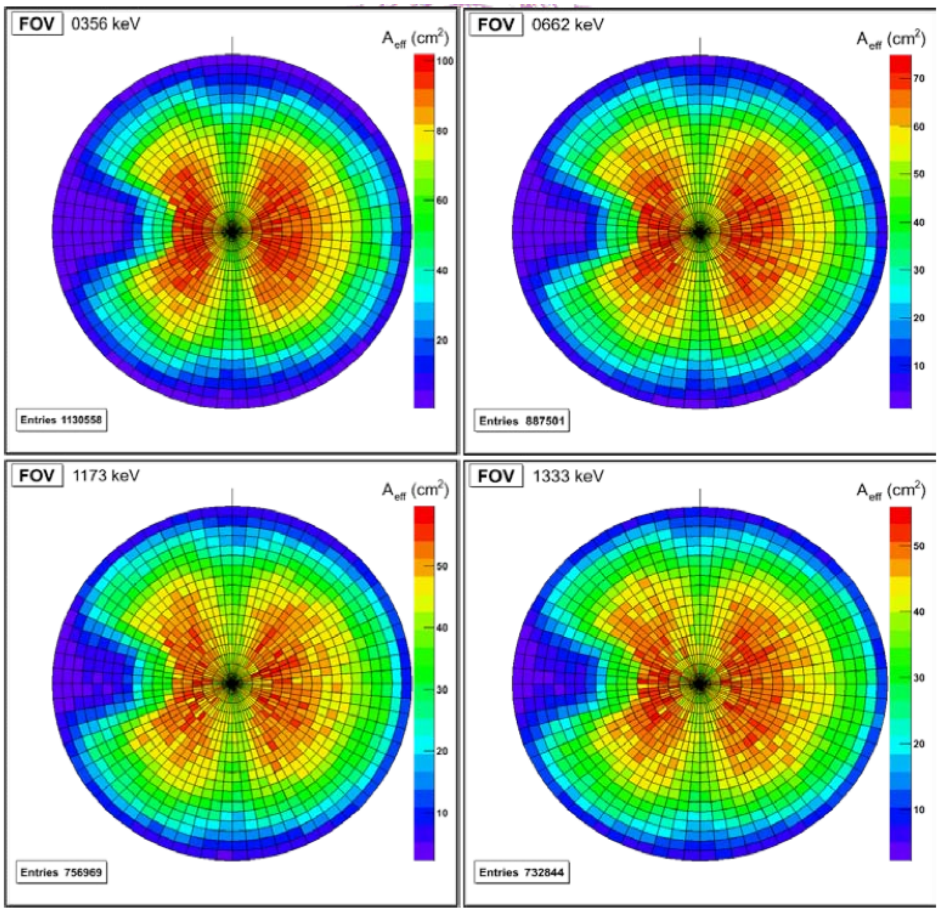

Figure 8.1: The simulated NCT field of view at several energies (Figure 5.19 of Chiu 2010). For each energy, an isotropic source was simulated, and the number of events produced from each sector of the field of view defines an efficiency, shown in the color scale. Deficits due to the liquid nitrogen tank (left notch), the vertical orientation of the detectors (center line), and the BGO shielding (outer edge) are visible.

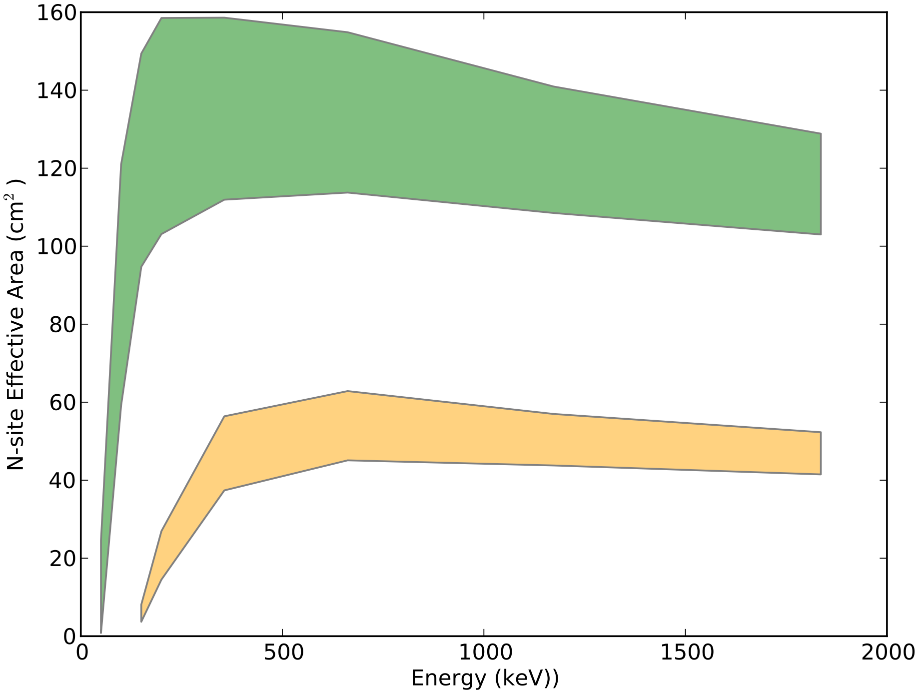

Figure 8.2: NCT effective area for N-site events as a function of incident photon energy. Any event which deposits energy in the 50–2000 keV band contributes to this effective area. The green curves give the range of effective area for all events (1 or more sites). The yellow curves give the range for multiple-site events (2 or more sites) that may be used for Compton imaging and polarimetry. The ranges for the effective area values were determined by simulations on-axis (minimum) and at 20° off-axis (maximum). (Above 200 keV, -20° and 50° points are also included in the range.) Event counts were obtained after the energy and depth calibration and strip pairing by Nuclearizer, but before Compton event reconstruction.

stores photoabsorption events down to the detector threshold at 40 keV. These single-site events may be used (without imaging) for transient searches. Furthermore, incompletely absorbed events will also contribute to the detection of transient events. Figure 8.2 shows the effective area for all events which deposit energy within the 50–2000 keV band as a function of the incident photon energy. NCT has significant single-site effective area over the entire band.

Figure 8.3 shows the 2009 NCT background spectrum at float for all events and for multiple-site events. The background rate for ten detectors is given in Table 8.1.

8.2 NCT's Sensitivity to GRBs

Band (2003) described a method for comparing the sensitivity of different GRB monitors

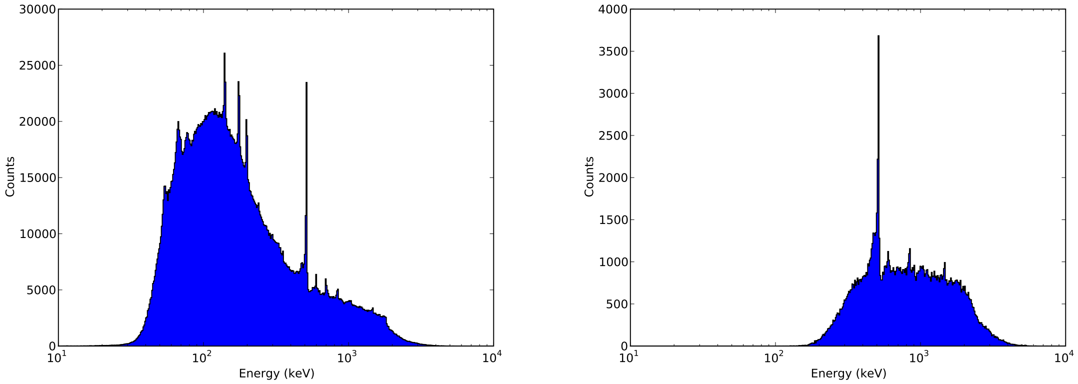

Figure 8.3: NCT 2009 float background spectrum (∼39 km altitude, ∼3.2 g/cm^2). The plotted energies are the total coincident energy for all detectors, using all events (left) and all multiple-site events (right). The data shown were taking from a portion of the first day's observations and include 15.5 ksec of observation time.

Energy Band (keV)	All Events (s^{-1})	Multiple-Site Events (s^{-1})	Compton Reconstructed with 15° ARM cut (s^{-1})
50–200 keV	131.	0.04	—
200–2000 keV	74.	9.4	1.17

Table 8.1: Background rates at float (39 km) for the 2009 NCT New Mexico flight. The 50–200 keV and 200–2000 keV bands contain primarily single-site and Compton events, respectively. Values are scaled to effective rates for ten detectors, as Detector 0 produced few usable counts in flight.

(see also Band 2006; Band et al. 2008). Assuming a 1.0 second trigger interval, the peak flux in a broad band (1 keV–1 MeV) at threshold is plotted as a function of E_{peak} for several spectral parameters α and β.

Figure 8.4 shows these sensitivity curves for NCT assuming a 50 keV–2 MeV trigger band and a 5σ threshold. I estimated the effective area from the values shown in Figure 8.2. I used the lower limits of the simulated all-site effective area curves as a proxy for the true effective area, as in Chapter 6 values derived from calibration data are smaller than those derived from simulations. The background values in each band are from the 2009 New Mexico flight (Table 8.1). These curves do not consider atmospheric absorption, which would further limit sensitivity.

Due to the computational intensity of Compton image reconstruction, a real-time transient trigger would need to operate on raw events. Accordingly, the sensitivity curves are derived from the raw events without any event cuts.

Neglecting atmospheric absorption, NCT's sensitivity curves are similar in shape to those of the BATSE LAD (Band 2003) but a factor of ∼4 larger, suggesting that NCT can

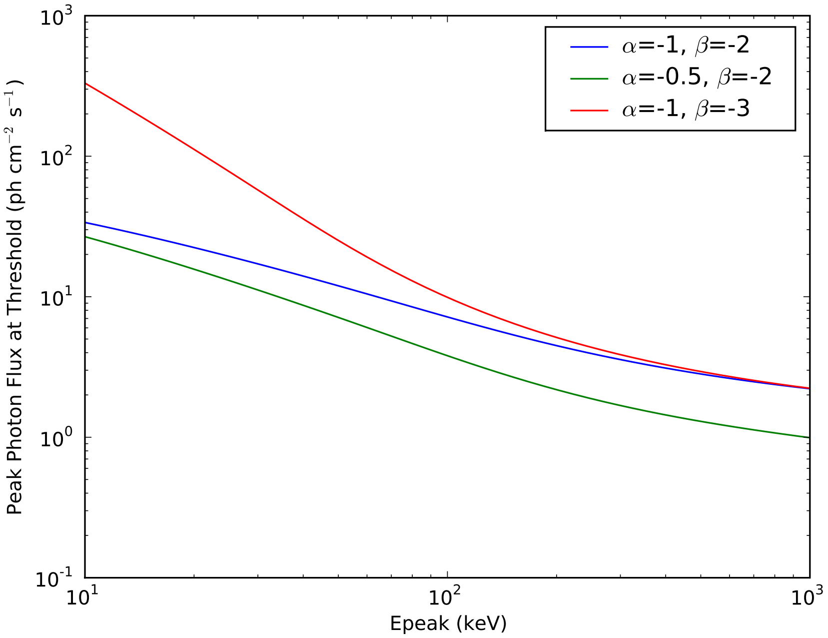

Figure 8.4: NCT's peak flux sensitivity to GRBs for a 50–2000 keV trigger band. A one-second interval and a 5σ trigger threshold are assumed.

perform effectively as a GRB monitor.

8.3 GRB Detection Rates

In order to determine NCT's expected GRB detection rates, I used the Band function spectral parameters determined for the bright BATSE GRB catalog of Kaneko et al. (2006). I assigned each burst a random direction within the NCT field of view (elevation greater than 30°) and calculated the expected counts according to three methods.

In the first, semi-analytic method, I used the effective area curves determined in Section 8.1. I integrated the Band spectrum numerically with the interpolated effective area curves, including atmospheric absorption for the assigned burst elevation assuming 39 km altitude. I then computed the signal-to-noise ratio using the 2009 NCT background rates (Table 8.1). (Because simulations overestimate the true effective area (Chapter 6), I used the minimum effective area values of Figure 8.2).

I also used a Monte Carlo method to determine the expected burst counts directly. I performed Cosima simulations for the bursts of the GRB catalog, again using the random positions within the NCT field of view. I scaled the recorded counts by the atmospheric absorption expected for the input spectrum.

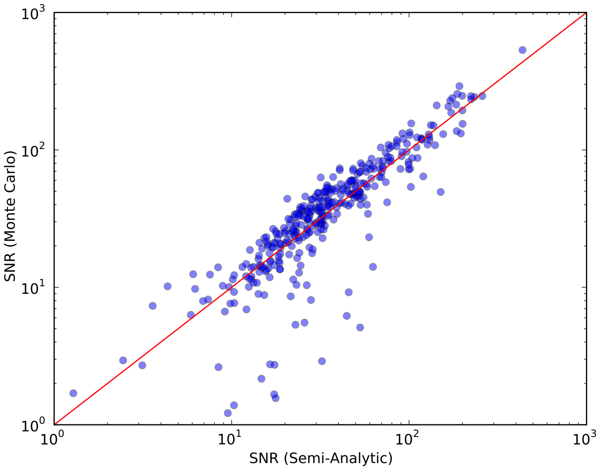

Figure 8.5: Comparison of the SNR of the semi-analytic and Monte Carlo GRB triggers.

Finally, I used the semi-analytic method with values appropriate for offline analysis of a Compton-imaged point source. I used the energy- and ARM- cut effective area data from Chapter 6. To determine the background count rate, I selected events within a 15° radius of a random point at 30° elevation from the 2009 NCT flight. For these Compton-imaged values, I also determined the minimum detectable polarization (MDP; Equation 7.7). For simplicity, I assumed a constant value of $\mu_{100} = 0.45$ (c.f. Figure 7.12).

Using these three methods, I evaluated the SNR for the BATSE bright bursts over the entire burst interval (fluence trigger) as well as scaled to the 1.024 second peak flux given by the BATSE catalog[1].

The detection significance was very similar for the semi-analytic and Monte Carlo methods (Figure 8.5). The Monte Carlo results show slightly higher SNR on average due to the use of the minimum of the effective area curve in the semi-analytic approach; this effect disappears when using the maximum effective area values. Figure 8.6 shows the location of the simulated bursts within the field of view. The only significant trend is the lower SNR of detection at low elevations due to atmospheric absorption.

Even with atmospheric absorption, NCT is capable of detecting virtually all of the bright bursts in the Kaneko et al. (2006) catalog (Table 8.2). The detection rate for Compton-imaged events is lower because of its higher energy band (200–2000 keV) and omission of incompletely-absorbed events.

A moderate fraction, 19.8%, of these bright bursts had MDP values less than 100%, indicating that Compton polarimetry could distinguish a completely polarized burst from a completely unpolarized one (Figure 8.7). The corresponding detection rate for polarized bursts is 0.010 days^{-1}. This makes detection of polarized GRBs by NCT unlikely even for

---

[1] `http://www.batse.msfc.nasa.gov/batse/grb/catalog/`

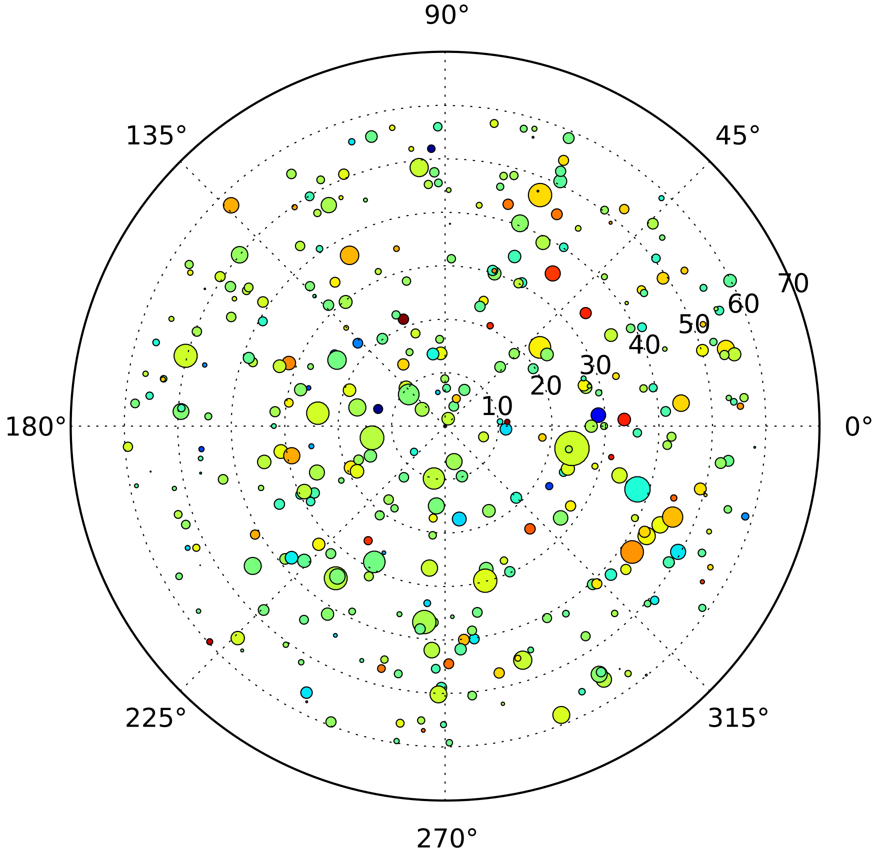

Figure 8.6: Significance of detection of Monte Carlo simulated bright GRBs throughout the NCT field of view. The size of each marker is scaled to the significance of its detection, while the logarithmic color scale indicates E_{peak}.

Data Type	Fluence Trigger	Peak Flux Trigger
Semi-Analytic	0.986	0.901
Monte Carlo	0.966	0.874
Compton-imaged	0.777	0.520

Table 8.2: Fraction of Kaneko et al. (2006) bright bursts detectable (5σ) by NCT.

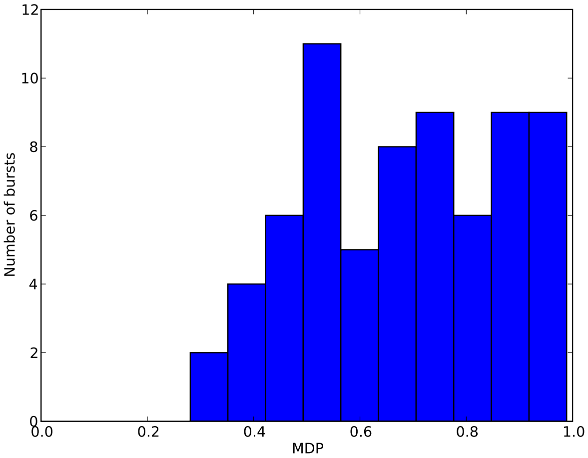

Figure 8.7: Histogram of the minimum detectable polarization values for the 69 bright bursts with MDP < 1.

Data Type	Fluence Trigger (days^{-1})	Peak Flux Trigger (days^{-1})
Semi-Analytic	0.144	0.100
Compton-imaged	0.049	0.030

Table 8.3: Expected detection rate by NCT for GRBs based on the complete BATSE catalog.

long- and ultralong-duration balloon flights. Freed of atmospheric absorption, a space-based mission (e.g., Boggs et al. 2010) with a wider field of view, more detectors, and a longer mission lifetime could perform a useful census of GRB polarization.

In order to determine the true threshold GRB detection rate, I used the complete BATSE catalog[2]. I assigned each burst a random set of spectral parameters from the bright burst sample, scaling the normalization to produce the 50–300 keV fluence given for that burst. I also assigned each burst a random elevation within the field of view for calculating atmospheric absorption.

The results of this procedure suggest that a balloon-borne version of NCT could detect about half of the GRBs in the total BATSE catalog. The corresponding detection rates are shown in Table 8.3. A long-duration balloon flight would be necessary for NCT to expect to detect a GRB.

---

[2] `http://www.batse.msfc.nasa.gov/batse/grb/catalog/`

8.4 Summary

With its wide field of view and moderate effective area, particularly when including single-site and incompletely absorbed events, NCT can effectively detect GRBs. However, atmospheric absorption and short flights limit its utility as a transient monitor on a balloon platform, and GRBs bright enough to allow polarization constraints of the prompt emission are rare. A satellite implementation of an NCT-like Compton telescope should yield valuable contributions to the study of GRBs.

Bibliography

Abbott, B., et al. 2008a, Classical and Quantum Gravity, 25, 114051, 0802.4320

—. 2008b, ApJ, 681, 1419, 0711.1163

Abbott, B. P., et al. 2010, ApJ, 715, 1438, 0908.3824

Abdo, A. A., et al. 2007, ApJ, 666, 361, 0705.1554

—. 2009a, ApJ, 706, L138, 0909.2470

—. 2009b, Science, 323, 1688

Ackermann, M., et al. 2010, ApJ, 716, 1178

—. 2011, ApJ, 729, 114

Aharonian, F., et al. 2009, A&A, 495, 505, 0901.2187

Akerlof, C., et al. 1999, Nature, 398, 400, arXiv:astro-ph/9903271

Allison, J., et al. 2006, Nuclear Science, IEEE Transactions on, 53, 270

Amati, L., et al. 2002, A&A, 390, 81, arXiv:astro-ph/0205230

Amman, M., & Luke, P. N. 2000, Nuclear Instruments and Methods in Physics Research A, 452, 155

Amman, M., Luke, P. N., & Boggs, S. E. 2007, Nuclear Instruments and Methods in Physics Research A, 579, 886

Amrose, S., Boggs, S. E., Coburn, W., Lin, R. P., & Smith, D. M. 2003, Nuclear Instruments and Methods in Physics Research A, 505, 170

Aprile, E., Bolotnikov, A., Chen, D., Mukherjee, R., & Xu, F. 1994, ApJS, 92, 689

Aprile, E., et al. 1996, in Society of Photo-Optical Instrumentation Engineers (SPIE) Conference Series, Vol. 2806, Society of Photo-Optical Instrumentation Engineers (SPIE) Conference Series, ed. B. D. Ramsey & T. A. Parnell, 337–348

Atkins, R., et al. 2000, ApJ, 533, L119

—. 2005, ApJ, 630, 996, arXiv:astro-ph/0503270

Atwood, W. B., et al. 2009, ApJ, 697, 1071, 0902.1089

Band, D., et al. 1993, ApJ, 413, 281

Band, D. L. 2003, ApJ, 588, 945, arXiv:astro-ph/0212452

—. 2006, ApJ, 644, 378, arXiv:astro-ph/0602267

Band, D. L., et al. 2008, ApJ, 673, 1225, 0710.4602

Bandstra, M., Bowen, J., Zoglauer, A., Boggs, S., Coburn, W., Wunderer, C., Amman, M., & Luke, P. 2006, in Nuclear Science Symposium Conference Record, 2006. IEEE, Vol. 2, 770–777

Bandstra, M., et al. 2009, in 2009 IEEE Nuclear Science Symposium Conference Record, 2131–2139

Bandstra, M. S. 2006, private communication

Bandstra, M. S. 2010, PhD thesis, University of California, Berkeley

Barthelmy, S. D., et al. 2005, Space Sci. Rev., 120, 143, arXiv:astro-ph/0507410

Bellm, E., et al. 2009, Nuclear Science, IEEE Transactions on, 56, 1250

Bellm, E. C. 2010, ApJ, 714, 881, 0908.2433

Bellm, E. C., Bandstra, M. E., Boggs, S. E., Hajdas, W., Hurley, K., Smith, D. M., & Wigger, C. 2008a, in American Institute of Physics Conference Series, Vol. 1000, Gamma-Ray Bursts 2007: Proceedings of the Santa Fe Conference, 154–157, arXiv:0801.2417

Bellm, E. C., et al. 2008b, ApJ, 688, 491, 0710.4590

Bellm, E. C., et al. 2010, in Society of Photo-Optical Instrumentation Engineers (SPIE) Conference Series, Vol. 7732, Space Telescopes and Instrumentation 2010: Ultraviolet to Gamma Ray, 773224

Beloborodov, A. M. 2005, ApJ, 618, L13, arXiv:astro-ph/0410050

Berger, E. 2011, New Astronomy Reviews, 55, 1

Berger, E., Kulkarni, S. R., & Frail, D. A. 2004, ApJ, 612, 966, arXiv:astro-ph/0405431

Berger, E., et al. 2005, Nature, 438, 988, arXiv:astro-ph/0508115

Bhattacharya, D., et al. 1999, in Proc. 26th International Cosmic Ray Conference, oG 4.1.19

Black, J. K., Baker, R. G., Deines-Jones, P., Hill, J. E., & Jahoda, K. 2007, Nuclear Instruments and Methods in Physics Research A, 581, 755

Blake, C. H., et al. 2005, Nature, 435, 181, arXiv:astro-ph/0503508

Blandford, R., & Eichler, D. 1987, Phys. Rep., 154, 1

Blandford, R. D., & McKee, C. F. 1976, Physics of Fluids, 19, 1130

Bloom, J. S., Butler, N. R., & Perley, D. A. 2008, in American Institute of Physics Conference Series, Vol. 1000, American Institute of Physics Conference Series, ed. M. Galassi, D. Palmer, & E. Fenimore, 11–15, 0804.0965

Bloom, J. S., Frail, D. A., & Kulkarni, S. R. 2003, ApJ, 594, 674, arXiv:astro-ph/0302210

Bloom, J. S., Frail, D. A., & Sari, R. 2001, AJ, 121, 2879, arXiv:astro-ph/0102371

Bloom, J. S., et al. 1999, Nature, 401, 453, arXiv:astro-ph/9905301

—. 2009, ApJ, 691, 723, 0803.3215

Bloser, P. F., Andritschke, R., Kanbach, G., Schopper, F., Zoglauer, A., & the MEGA Collaboration. 2002, New Astronomy Reviews, 46, 611

Bloser, P. F., Legere, J. S., Macri, J. R., McConnell, M. L., Narita, T., & Ryan, J. M. 2006, Chinese Journal of Astronomy and Astrophysics Supplement, 6, 010000, arXiv:astro-ph/0508314

Bloser, P. F., Legere, J. S., McConnell, M. L., Macri, J. R., Bancroft, C. M., Connor, T. P., & Ryan, J. M. 2009, NIM A, 600, 424, 0812.0782

Boella, G., Butler, R. C., Perola, G. C., Piro, L., Scarsi, L., & Bleeker, J. A. M. 1997, A&AS, 122, 299

Boggs, S., et al. 2006a, Experimental Astronomy, 25

—. 2010, ArXiv e-prints, 1006.2102

Boggs, S. E., Coburn, W., & Kalemci, E. 2006b, ApJ, 638, 1129, arXiv:astro-ph/0510588

Boggs, S. E., Coburn, W., Smith, D. M., Bowen, J. D., Jean, P., Kregenow, J. M., Lin, R. P., & von Ballmoos, P. 2004, New Astron. Rev., 48, 251

Boggs, S. E., & Jean, P. 2000, A&AS, 145, 311, arXiv:astro-ph/0005250

Boggs, S. E., Zoglauer, A., Bellm, E., Hurley, K., Lin, R. P., Smith, D. M., Wigger, C., & Hajdas, W. 2007, ApJ, 661, 458, arXiv:astro-ph/0611318

Boggs, S. E., et al. 1998, Advances in Space Research, 21, 1015

Boggs, S. E., et al. 2003, in Proceedings of the SPIE, Vol. 4851, X-Ray and Gamma-Ray Telescopes and Instruments for Astronomy, ed. J. E. Truemper & H. D. Tananbaum, 1221–1227

Bowen, J., Bandstra, S., Zoglauer, A., Wunderer, C., Amman, M., & Luke, P. 2007, in 2007 IEEE Nuclear Science Symposium Conference Record, Vol. 1, 436–444

Bucciantini, N., Quataert, E., Arons, J., Metzger, B. D., & Thompson, T. A. 2007, MNRAS, 380, 1541, 0705.1742

—. 2008, MNRAS, 383, L25, 0707.2100

Bucciantini, N., Quataert, E., Metzger, B. D., Thompson, T. A., Arons, J., & Del Zanna, L. 2009, MNRAS, 396, 2038, 0901.3801

Burrows, D. N., et al. 2005, Science, 309, 1833, arXiv:astro-ph/0506130

Butler, N. R., & Kocevski, D. 2007, ApJ, 663, 407, arXiv:astro-ph/0612564

Butler, N. R., Kocevski, D., Bloom, J. S., & Curtis, J. L. 2007, ApJ, 671, 656, arXiv:0706.1275

Campana, S., et al. 2006, Nature, 442, 1008, arXiv:astro-ph/0603279

Cash, W. 1979, ApJ, 228, 939

Cenko, S. B., et al. 2010, ApJ, 711, 641, 0905.0690

Chandra, P., et al. 2008, ApJ, 683, 924, 0802.2748

Chiu, J.-L. 2010, PhD thesis, National Tsing Hua University

Chiu, J.-L., et al. 2009, in Nuclear Science Symposium Conference Record (NSS/MIC), 2009 IEEE, 472–476

Coburn, W., & Boggs, S. E. 2003, Nature, 423, 415, arXiv:astro-ph/0305377

Coburn, W., et al. 2003, in Proceedings of the SPIE, Vol. 4784, X-Ray and Gamma-Ray Detectors and Applications IV, ed. R. B. James, L. A. Franks, A. Burger, E. W. Westbrook, & R. D. Durst, 54–63

Coburn, W., et al. 2004, in Proceedings of the SPIE, Vol. 5165, X-Ray and Gamma-Ray Instrumentation for Astronomy XIII., ed. K. A. Flanagan & O. H. W. Siegmund, 131–138

Coburn, W., et al. 2005, in Proceedings of the SPIE, Vol. 5898, UV, X-Ray, and Gamma-Ray Space Instrumentation for Astronomy XIV, ed. O. H. W. Siegmund, 13–21

Cohen, E., Piran, T., & Sari, R. 1998, ApJ, 509, 717, arXiv:astro-ph/9803258

Compton, A. H. 1923, Physical Review, 21, 483

Costa, E., et al. 1997, Nature, 387, 783, astro-ph/9706065

Crider, A., et al. 1997, ApJ, 479, L39, arXiv:astro-ph/9612118

Curioni, A., Aprile, E., Doke, T., Giboni, K. L., Kobayashi, M., & Oberlack, U. G. 2007, Nuclear Instruments and Methods in Physics Research A, 576, 350, arXiv:physics/0702078

Daigne, F., Bošnjak, Ž., & Dubus, G. 2011, A&A, 526, A110, 1009.2636

Dean, A. J., Bird, A. J., Diallo, N., Ferguson, C., Lockley, J. J., Shaw, S. E., Westmore, M. J., & Willis, D. R. 2003, Space Science Reviews, 105, 285

Dean, A. J., et al. 2008, Science, 321, 1183

Della Valle, M., et al. 2006, Nature, 444, 1050, arXiv:astro-ph/0608322

Dessart, L., Burrows, A., Livne, E., & Ott, C. D. 2008, ApJ, 673, L43, 0710.5789

Diehl, R., et al. 1995, A&A, 298, 445

Drenkhahn, G., & Spruit, H. C. 2002, A&A, 391, 1141, arXiv:astro-ph/0202387

Eadie, W. T., Drijard, D., James, F. E., Roos, M., & Sadoulet, B. 1971, Statistical Methods in Experimental Physics (Amsterdam: North-Holland)

Eichler, D., & Granot, J. 2006, ApJ, 641, L5, arXiv:astro-ph/0509857

Eichler, D., Livio, M., Piran, T., & Schramm, D. N. 1989, Nature, 340, 126

Esin, A. A., & Blandford, R. 2000, ApJ, 534, L151, arXiv:astro-ph/0003415

Fabris, L., Madden, N. W., & Yaver, H. 1999, Nuclear Instruments and Methods in Physics Research A, 424, 545

Fan, Y., & Piran, T. 2006, MNRAS, 369, 197, arXiv:astro-ph/0601054

Fenimore, E. E., Madras, C. D., & Nayakshin, S. 1996, ApJ, 473, 998, arXiv:astro-ph/9607163

Fishman, G. J., Meegan, C. A., Wilson, R. B., Paciesas, T. A., & et al. 1989, in Proceedings of the First GRO Science Workshop, ed. W. N. Johnson, NASA Conference Publication,, 2–39

Foley, S., McGlynn, S., Hanlon, L., McBreen, S., & McBreen, B. 2008, A&A, 484, 143, 0803.1821

Ford, L. A., et al. 1995, ApJ, 439, 307, arXiv:astro-ph/9407090

Forot, M., Laurent, P., Grenier, I. A., Gouiffès, C., & Lebrun, F. 2008, ApJ, 688, L29, 0809.1292

Fox, D. B., et al. 2005, Nature, 437, 845, arXiv:astro-ph/0510110

Frail, D. A., Kulkarni, S. R., Nicastro, L., Feroci, M., & Taylor, G. B. 1997, Nature, 389, 261

Frail, D. A., Soderberg, A. M., Kulkarni, S. R., Berger, E., Yost, S., Fox, D. W., & Harrison, F. A. 2005, ApJ, 619, 994, arXiv:astro-ph/0408002

Frail, D. A., Waxman, E., & Kulkarni, S. R. 2000, ApJ, 537, 191, arXiv:astro-ph/9910319

Frail, D. A., et al. 2001, ApJ, 562, L55, arXiv:astro-ph/0102282

Freeman, P. E., Lamb, D. Q., Wang, J. C. L., Wasserman, I., Loredo, T. J., Fenimore, E. E., Murakami, T., & Yoshida, A. 1999, ApJ, 524, 772, arXiv:astro-ph/9906395

Fynbo, J. P. U., et al. 2006, Nature, 444, 1047, arXiv:astro-ph/0608313

Galama, T. J., et al. 1998, Nature, 395, 670, arXiv:astro-ph/9806175

Gehrels, N. 1986, ApJ, 303, 336

Gehrels, N., Ramirez-Ruiz, E., & Fox, D. B. 2009, ARA&A, 47, 567, 0909.1531

Gehrels, N., et al. 2004, ApJ, 611, 1005, astro-ph/0405233

—. 2005, Nature, 437, 851, arXiv:astro-ph/0505630

—. 2006, Nature, 444, 1044, arXiv:astro-ph/0610635

Ghirlanda, G., Bosnjak, Z., Ghisellini, G., Tavecchio, F., & Firmani, C. 2007, MNRAS, 379, 73, 0704.3438

Ghirlanda, G., Celotti, A., & Ghisellini, G. 2002, A&A, 393, 409, arXiv:astro-ph/0206377

—. 2003, A&A, 406, 879, arXiv:astro-ph/0210693

Ghirlanda, G., Ghisellini, G., & Lazzati, D. 2004, ApJ, 616, 331, arXiv:astro-ph/0405602

Ghisellini, G., Celotti, A., & Lazzati, D. 2000, MNRAS, 313, L1, arXiv:astro-ph/9912461

Ghisellini, G., Ghirlanda, G., Nava, L., & Firmani, C. 2007, ApJ, 658, L75, arXiv:astro-ph/0701430

Giannios, D. 2006, A&A, 457, 763, arXiv:astro-ph/0602397

—. 2008, A&A, 480, 305, 0711.2632

Golenetskii, S., Aptekar, R., Mazets, E., Pal'Shin, V., Frederiks, D., & Cline, T. 2006a, GRB Coordinates Network, 5837, 1

—. 2006b, GRB Coordinates Network, 5722, 1

González, M. M., Dingus, B. L., Kaneko, Y., Preece, R. D., Dermer, C. D., & Briggs, M. S. 2003, Nature, 424, 749

Götz, D., Laurent, P., Lebrun, F., Daigne, F., & Bošnjak, Ž. 2009, ApJ, 695, L208, 0903.1712

Granot, J., Königl, A., & Piran, T. 2006, MNRAS, 370, 1946, arXiv:astro-ph/0601056

Granot, J., Piran, T., & Sari, R. 2000, ApJ, 534, L163, arXiv:astro-ph/0001160

Granot, J., & Sari, R. 2002, ApJ, 568, 820, arXiv:astro-ph/0108027

Gruber, D., et al. 2011, ArXiv e-prints, 1101.1099

Halloin, H., et al. 2003, Nuclear Instruments and Methods in Physics Research A, 504, 120

Harrison, F. A., et al. 1999, ApJ, 523, L121, arXiv:astro-ph/9905306

Hjorth, J., et al. 2003, Nature, 423, 847, arXiv:astro-ph/0306347

—. 2005a, ApJ, 630, L117, arXiv:astro-ph/0506123

—. 2005b, Nature, 437, 859, arXiv:astro-ph/0510096

Houck, J. C., & Denicola, L. A. 2000, in Astronomical Society of the Pacific Conference Series, Vol. 216, Astronomical Data Analysis Software and Systems IX, ed. N. Manset, C. Veillet, & D. Crabtree, 591

Humphrey, P. J., Liu, W., & Buote, D. A. 2009, ApJ, 693, 822, 0811.2796

Hung, W.-C., et al. 2009, Nuclear Science, IEEE Transactions on, 56, 2303

Hurford, G. J., et al. 2002, Sol. Phys., 210, 61

Hurley, K., et al. 1994, Nature, 372, 652

—. 2005, Nature, 434, 1098, arXiv:astro-ph/0502329

—. 2010, MNRAS, 403, 342, 0907.2462

IceCube Collaboration et al. 2011, ArXiv e-prints, 1101.1448

Ioka, K., Toma, K., Yamazaki, R., & Nakamura, T. 2006, A&A, 458, 7, arXiv:astro-ph/0511749

Iyudin, A. F., et al. 1994, A&A, 284, L1

—. 1998, Nature, 396, 142

Jarvis, A., et al. 2010, ApJ, 722, 862

Jauncey, G. E., & Harvey, G. G. 1931, Physical Review, 37, 698

Kalemci, E., Boggs, S. E., Kouveliotou, C., Finger, M., & Baring, M. G. 2007, ApJS, 169, 75, arXiv:astro-ph/0610771

Kamae, T., et al. 2008, Astroparticle Physics, 30, 72, 0709.1278

Kanbach, G., et al. 2004, New Astronomy Review, 48, 275

Kaneko, Y., González, M. M., Preece, R. D., Dingus, B. L., & Briggs, M. S. 2008, ApJ, 677, 1168, 0801.1869

Kaneko, Y., Preece, R. D., Briggs, M. S., Paciesas, W. S., Meegan, C. A., & Band, D. L. 2006, ApJS, 166, 298, arXiv:astro-ph/0601188

Katz, J. I. 1994, ApJ, 432, L107, arXiv:astro-ph/9312034

Kishimoto, Y., et al. 2007, IEEE Transactions on Nuclear Science, 54, 561

Klebesadel, R. W., Strong, I. B., & Olson, R. A. 1973, ApJ, 182, L85

Knödlseder, J., von Ballmoos, P., Frontera, F., Bazzano, A., Christensen, F., Hernanz, M., & Wunderer, C. 2009, Experimental Astronomy, 23, 121, 0707.4627

Kobayashi, S., Zhang, B., Mészáros, P., & Burrows, D. 2007, ApJ, 655, 391, arXiv:astro-ph/0506157

Kocevski, D., & Butler, N. 2008, ApJ, 680, 531, 0707.4478

Kokubun, M., et al. 2010, Nuclear Instruments and Methods in Physics Research A, 623, 425

Kouveliotou, C., Meegan, C. A., Fishman, G. J., Bhat, N. P., Briggs, M. S., Koshut, T. M., Paciesas, W. S., & Pendleton, G. N. 1993, ApJ, 413, L101

Krawczynski, H. 2011, ArXiv e-prints, 1102.1228

Krawczynski, H., et al. 2009, IEEE Transactions on Nuclear Science, 56, 3607, 0812.1809

Krimm, H. A., et al. 2006, ApJ, 648, 1117, astro-ph/0605507

—. 2007, ApJ, 665, 554, arXiv:astro-ph/0702603

—. 2009, ApJ, 704, 1405, 0908.1335

Kulkarni, S. R., et al. 1998a, Nature, 393, 35

—. 1998b, Nature, 395, 663

—. 1999, Nature, 398, 389, arXiv:astro-ph/9902272

Kumar, P. 1999, ApJ, 523, L113, arXiv:astro-ph/9907096

Kumar, P., & McMahon, E. 2008, MNRAS, 384, 33, arXiv:0802.2704

Kumar, P., & Panaitescu, A. 2008, MNRAS, 391, L19, 0805.0144

Lazzati, D., Rossi, E., Covino, S., Ghisellini, G., & Malesani, D. 2002, A&A, 396, L5, arXiv:astro-ph/0210333

Lee, W. H., & Ramirez-Ruiz, E. 2007, New Journal of Physics, 9, 17, arXiv:astro-ph/0701874

Lei, F., Dean, A. J., & Hills, G. L. 1997, Space Science Reviews, 82, 309

Lei, F., Hills, G. L., Dean, A. J., & Swinyard, B. M. 1996, A&AS, 120, C695

Liang, E., Racusin, J. L., Zhang, B., Zhang, B., & Burrows, D. N. 2008, ApJ, 675, 528, 0708.2942

Lin, R. P., et al. 2002, Sol. Phys., 210, 3

Lithwick, Y., & Sari, R. 2001, ApJ, 555, 540, arXiv:astro-ph/0011508

Liu, Z.-K., et al. 2009, Nuclear Science, IEEE Transactions on, 56, 1210

Lloyd, N. M., & Petrosian, V. 2000, ApJ, 543, 722, arXiv:astro-ph/0007061

Lloyd-Ronning, N. M., & Petrosian, V. 2002, ApJ, 565, 182, arXiv:astro-ph/0109340

Luke, P. N., Cork, C. P., Madden, N. W. Rossington, C. S., & Wesela, M. F. 1992, IEEE Trans. Nucl. Sci., 39, 590

Lyubarsky, Y. E. 2005, MNRAS, 358, 113, arXiv:astro-ph/0501392

Lyutikov, M. 2006, New Journal of Physics, 8, 119, arXiv:astro-ph/0512342

Lyutikov, M., & Blandford, R. 2003, ArXiv Astrophysics e-prints, arXiv:astro-ph/0312347

Lyutikov, M., & Uzdensky, D. 2003, ApJ, 589, 893, arXiv:astro-ph/0210206

MacFadyen, A. I., Ramirez-Ruiz, E., & Zhang, W. 2005, ArXiv Astrophysics e-prints, arXiv:astro-ph/0510192

MacFadyen, A. I., & Woosley, S. E. 1999, ApJ, 524, 262, arXiv:astro-ph/9810274

MacFadyen, A. I., Woosley, S. E., & Heger, A. 2001, ApJ, 550, 410, arXiv:astro-ph/9910034

Mahoney, W. A., Ling, J. C., Jacobson, A. S., & Tapphorn, R. M. 1980, Nuclear Instruments and Methods, 178, 363

Malesani, D., et al. 2004, ApJ, 609, L5, arXiv:astro-ph/0405449

Matteson, J. L. 1978, in AIAA, Aerospace Sciences Meeting, ed. A. Ungut, A. J. Yule, D. S. Taylor, & N. A. Chigier

Mazets, E. P., et al. 2008, ApJ, 680, 545, 0712.1502

McBreen, S., Hanlon, L., McGlynn, S., McBreen, B., Foley, S., Preece, R., von Kienlin, A., & Williams, O. R. 2006, A&A, 455, 433, arXiv:astro-ph/0604455

McGlynn, S., et al. 2007, A&A, 466, 895, arXiv:astro-ph/0702738

McKinney, J. C., & Uzdensky, D. A. 2010, ArXiv e-prints, 1011.1904

Medvedev, M. V. 2000, ApJ, 540, 704, arXiv:astro-ph/0001314

Meegan, C. A., Fishman, G. J., Wilson, R. B., Horack, J. M., Brock, M. N., Paciesas, W. S., Pendleton, G. N., & Kouveliotou, C. 1992, Nature, 355, 143

Meszaros, P., & Rees, M. J. 1997, ApJ, 476, 232, arXiv:astro-ph/9606043

Mészáros, P., & Rees, M. J. 2000, ApJ, 530, 292, arXiv:astro-ph/9908126

Meszaros, P., Rees, M. J., & Papathanassiou, H. 1994, ApJ, 432, 181, arXiv:astro-ph/9311071

Meszaros, P., Rees, M. J., & Wijers, R. A. M. J. 1998, ApJ, 499, 301, arXiv:astro-ph/9709273

Metzger, B. D., Giannios, D., Thompson, T. A., Bucciantini, N., & Quataert, E. 2010, ArXiv e-prints, 1012.0001

Metzger, B. D., Quataert, E., & Thompson, T. A. 2008, MNRAS, 385, 1455, 0712.1233

Metzger, M. R., Djorgovski, S. G., Kulkarni, S. R., Steidel, C. C., Adelberger, K. L., Frail, D. A., Costa, E., & Frontera, F. 1997, Nature, 387, 878

Nakar, E. 2007, Phys. Rep., 442, 166, arXiv:astro-ph/0701748

Nakar, E., Piran, T., & Granot, J. 2003, New Astronomy Reviews, 8, 495, arXiv:astro-ph/0210631

Narayan, R., Paczynski, B., & Piran, T. 1992, ApJ, 395, L83, arXiv:astro-ph/9204001

NASA. 2010, Nuclear Compton Telescope Balloon Launch in Alice Springs, Northern Territory, Australia, IRIS Case Number S-2010-119-00007

Nomoto, K., & Kondo, Y. 1991, ApJ, 367, L19

Norris, J. P., & Bonnell, J. T. 2006, ApJ, 643, 266, arXiv:astro-ph/0601190

Nousek, J. A., et al. 2006, ApJ, 642, 389, arXiv:astro-ph/0508332

Oates, S. R., et al. 2009, MNRAS, 395, 490, 0901.3597

Ofek, E. O. 2007, ApJ, 659, 339, arXiv:astro-ph/0611860

Ofek, E. O., et al. 2008, ApJ, 681, 1464, 0712.3585

Paczynski, B. 1986, ApJ, 308, L43

Page, K. L., et al. 2007, ApJ, 663, 1125, arXiv:0704.1609

Palmer, D. M., et al. 2005, Nature, 434, 1107, arXiv:astro-ph/0503030

Panaitescu, A., & Mészáros, P. 2000, ApJ, 544, L17, arXiv:astro-ph/0009309

Panaitescu, A., Mészáros, P., Gehrels, N., Burrows, D., & Nousek, J. 2006, MNRAS, 366, 1357, arXiv:astro-ph/0508340

Pe'er, A., Ryde, F., Wijers, R. A. M. J., Mészáros, P., & Rees, M. J. 2007, ApJ, 664, L1, arXiv:astro-ph/0703734

Pe'er, A., & Zhang, B. 2006, ApJ, 653, 454, arXiv:astro-ph/0605641

Pe'er, A., Zhang, B., Ryde, F., McGlynn, S., Zhang, B., Preece, R. D., & Kouveliotou, C. 2010, ArXiv e-prints, 1007.2228

Pélangeon, A., et al. 2008, A&A, 491, 157, 0811.3304

Pelling, M., et al. 1992, in Society of Photo-Optical Instrumentation Engineers (SPIE) Conference Series, Vol. 1743, Society of Photo-Optical Instrumentation Engineers (SPIE) Conference Series, ed. O. H. W. Siegmund, 408–421

Perley, D. A., et al. 2009, AJ, 138, 1690, 0905.0001

Piran, T. 2004, Reviews of Modern Physics, 76, 1143, arXiv:astro-ph/0405503

Plüschke, S., et al. 2001, in ESA Special Publication, Vol. 459, Exploring the Gamma-Ray Universe, ed. A. Gimenez, V. Reglero, & C. Winkler, 55–58, arXiv:astro-ph/0104047

Preece, R. D. 2000, in Bulletin of the American Astronomical Society, Vol. 32, Bulletin of the American Astronomical Society, 1231

Preece, R. D., Briggs, M. S., Giblin, T. W., Mallozzi, R. S., Pendleton, G. N., Paciesas, W. S., & Band, D. L. 2002, ApJ, 581, 1248

Preece, R. D., Briggs, M. S., Mallozzi, R. S., Pendleton, G. N., Paciesas, W. S., & Band, D. L. 1998a, ApJ, 506, L23, arXiv:astro-ph/9808184

Preece, R. D., Pendleton, G. N., Briggs, M. S., Mallozzi, R. S., Paciesas, W. S., Band, D. L., Matteson, J. L., & Meegan, C. A. 1998b, ApJ, 496, 849, arXiv:astro-ph/9711153

Racusin, J. L., et al. 2008, Nature, 455, 183, 0805.1557

Rees, M. J., & Meszaros, P. 1994, ApJ, 430, L93, arXiv:astro-ph/9404038

—. 1998, ApJ, 496, L1, arXiv:astro-ph/9712252

Rhoads, J. E. 1997, ApJ, 487, L1, arXiv:astro-ph/9705163

Romano, P., et al. 2006, A&A, 456, 917, arXiv:astro-ph/0602497

Roming, P. W. A., et al. 2009, ApJ, 690, 163, 0809.4193

Ryde, F. 2004, ApJ, 614, 827, arXiv:astro-ph/0406674

—. 2005, ApJ, 625, L95, astro-ph/0504450

Ryde, F., Björnsson, C.-I., Kaneko, Y., Mészáros, P., Preece, R., & Battelino, M. 2006, ApJ, 652, 1400, arXiv:astro-ph/0608363

Ryde, F., & Pe'er, A. 2009, ApJ, 702, 1211, 0811.4135

Ryde, F., et al. 2010, ApJ, 709, L172, 0911.2025

Sakamoto, T., et al. 2005, ApJ, 629, 311
—. 2008, ApJS, 175, 179, 0707.4626
—. 2009, ApJ, 693, 922, 0811.3401
—. 2010, ArXiv e-prints, 1011.1301
Sari, R., & Piran, T. 1997, ApJ, 485, 270, arXiv:astro-ph/9701002
—. 1999, ApJ, 520, 641, arXiv:astro-ph/9901338
Sari, R., Piran, T., & Halpern, J. P. 1999, ApJ, 519, L17, arXiv:astro-ph/9903339
Sari, R., Piran, T., & Narayan, R. 1998, ApJ, 497, L17, arXiv:astro-ph/9712005
Scargle, J. D. 1998, ApJ, 504, 405
Schönfelder, V., et al. 1993, ApJS, 86, 657
Schönfelder, V., et al. 2000, A&AS, 143, 145, arXiv:astro-ph/0002366
Shivvers, I., & Berger, E. 2011, ArXiv e-prints, 1101.0603
Sironi, L., & Spitkovsky, A. 2009, ApJ, 707, L92, 0908.3193
Skinner, G. K. 2001, A&A, 375, 691
—. 2002, A&A, 383, 352
—. 2010, ArXiv e-prints, 1009.2101
Smith, D. M. 2003, ApJ, 589, L55, arXiv:astro-ph/0304508
Smith, D. M. 2005, private communication
Smith, D. M., Lopez, L. I., Lin, R. P., & Barrington-Leigh, C. P. 2005, Science, 307, 1085
Smith, D. M., et al. 2002, Sol. Phys., 210, 33
Soderberg, A. M., et al. 2004, Nature, 430, 648, arXiv:astro-ph/0408096
—. 2006a, Nature, 442, 1014, arXiv:astro-ph/0604389
—. 2006b, ApJ, 650, 261, arXiv:astro-ph/0601455
Spitkovsky, A. 2008a, ApJ, 673, L39, 0706.3126
—. 2008b, ApJ, 682, L5, 0802.3216
Spruit, H. C., Daigne, F., & Drenkhahn, G. 2001, A&A, 369, 694, arXiv:astro-ph/0004274
Stanek, K. Z., et al. 2003, ApJ, 591, L17, arXiv:astro-ph/0304173
Starling, R. L. C., et al. 2011, MNRAS, 411, 2792, 1004.2919
Sturner, S. J., Seifert, H., Shrader, C., & Teegarden, B. J. 2000, in American Institute of Physics Conference Series, Vol. 510, American Institute of Physics Conference Series, ed. M. L. McConnell & J. M. Ryan, 814
Taylor, G. B., Frail, D. A., Berger, E., & Kulkarni, S. R. 2004, ApJ, 609, L1, arXiv:astro-ph/0405300
Taylor, P. A., Miller, J. C., & Podsiadlowski, P. 2011, MNRAS, 410, 2385
Thompson, T. A., Chang, P., & Quataert, E. 2004, ApJ, 611, 380, arXiv:astro-ph/0401555
Thompson, T. A., Metzger, B. D., & Bucciantini, N. 2010, in American Institute of Physics Conference Series, Vol. 1279, American Institute of Physics Conference Series, ed. N. Kawai & S. Nagataki, 81–88, 1008.5138
Toma, K., Ioka, K., Yamazaki, R., & Nakamura, T. 2006, ApJ, 640, L139, arXiv:astro-ph/0511718
Toma, K., et al. 2009, ApJ, 698, 1042, 0812.2483
Ueno, K., et al. 2008, in Society of Photo-Optical Instrumentation Engineers (SPIE) Confer-

ence Series, Vol. 7011, Society of Photo-Optical Instrumentation Engineers (SPIE) Conference Series

Usov, V. V. 1992, Nature, 357, 472

Uzdensky, D. A. 2011, Space Sci. Rev., 19, 1101.2472

Uzdensky, D. A., & McKinney, J. C. 2010, ArXiv e-prints, 1007.0774

van der Horst, A. J., et al. 2008, A&A, 480, 35, 0706.1321

van Eerten, H., Zhang, W., & MacFadyen, A. 2010, ApJ, 722, 235, 1006.5125

van Eerten, H. J., Meliani, Z., Wijers, R. A. M. J., & Keppens, R. 2011, MNRAS, 410, 2016, 1005.3966

van Paradijs, J., et al. 1997, Nature, 386, 686

Vanderspek, R., et al. 2004, ApJ, 617, 1251, arXiv:astro-ph/0401311

Vestrand, W. T., et al. 2005, Nature, 435, 178, arXiv:astro-ph/0503521

von Ballmoos, P., et al. 2005, Experimental Astronomy, 20, 253

Wang, X., & Loeb, A. 2000, ApJ, 535, 788, arXiv:astro-ph/9910477

Waxman, E., & Bahcall, J. 1997, Physical Review Letters, 78, 2292, arXiv:astro-ph/9701231

Waxman, E., & Draine, B. T. 2000, ApJ, 537, 796, arXiv:astro-ph/9909020

Weisskopf, M. C., Elsner, R. F., & O'Dell, S. L. 2010, in Society of Photo-Optical Instrumentation Engineers (SPIE) Conference Series, Vol. 7732, Space Telescopes and Instrumentation 2010: Ultraviolet to Gamma Ray, 1006.3711

Wigger, C., Hajdas, W., Arzner, K., Güdel, M., & Zehnder, A. 2004, ApJ, 613, 1088, arXiv:astro-ph/0405525

Wigger, C., Wigger, O., Bellm, E., & Hajdas, W. 2008, ApJ, 675, 553, 0710.2858

Wilderman, S., Rogers, W., Knoll, G., & Engdahl, J. 1998, Nuclear Science, IEEE Transactions on, 45, 957

Willis, D. R., et al. 2005, A&A, 439, 245, arXiv:astro-ph/0505097

Woosley, S. E. 1993, ApJ, 405, 273

Woosley, S. E., & Bloom, J. S. 2006, ARA&A, 44, 507, arXiv:astro-ph/0609142

Woosley, S. E., & Heger, A. 2006, ApJ, 637, 914, arXiv:astro-ph/0508175

Yamada, M., Kulsrud, R., & Ji, H. 2010, Reviews of Modern Physics, 82, 603

Zhang, B. 2007, Advances in Space Research, 40, 1186, arXiv:astro-ph/0611774

Zhang, B., Fan, Y. Z., Dyks, J., Kobayashi, S., Mészáros, P., Burrows, D. N., Nousek, J. A., & Gehrels, N. 2006, ApJ, 642, 354, arXiv:astro-ph/0508321

Zhang, B., & Mészáros, P. 2002, ApJ, 571, 876, arXiv:astro-ph/0112118

Zhang, B., & Yan, H. 2011, ApJ, 726, 90, 1011.1197

Zhang, B., Zhang, B.-B., Liang, E.-W., Gehrels, N., Burrows, D. N., & Mészáros, P. 2007a, ApJ, 655, L25, arXiv:astro-ph/0612238

Zhang, B., et al. 2007b, ApJ, 655, 989, arXiv:astro-ph/0610177

—. 2010, ArXiv e-prints, 1009.3338

Zoglauer, A. 2005, PhD thesis, Technical University Munich

Zoglauer, A., Andritschke, R., & Kanbach, G. 2004a, New Astronomy Review, 48, 231

Zoglauer, A., Andritschke, R., Kanbach, G., Bloser, P. F., & Litvinenko, V. N. 2004b, in ESA Special Publication, Vol. 552, 5th INTEGRAL Workshop on the INTEGRAL Universe, ed. V. Schoenfelder, G. Lichti, & C. Winkler, 921

Zoglauer, A., Andritschke, R., & Schopper, F. 2006, New Astron. Rev., 50, 629

Zoglauer, A., Boggs, S. E., Andritschke, R., & Kanbach, G. 2007, in Proceedings of the SPIE, Vol. 6700, Mathematics of Data/Image Pattern Recognition, Compression, Coding, and Encryption X, with Applications.

Zoglauer, A., & Kanbach, G. 2003, in Proceedings of the SPIE, Vol. 4851, X-Ray and Gamma-Ray Telescopes and Instruments for Astronomy, ed. J. E. Truemper & H. D. Tananbaum, 1302–1309

Zweibel, E. G., & Yamada, M. 2009, ARA&A, 47, 291